Chapter 8
Instability and Chaos in Various Laser Structures

Narrow-stripe edge-emitting structure is not the only one for semiconductor lasers. Other than these, various kinds of laser structures of semiconductor lasers have been proposed and some of them are now in practical use. For example, self-pulsating semiconductor lasers are used for light sources of optical mass data storage systems, vertical cavity surface-emitting semiconductor lasers (VCSELs) are expected as the next generation laser light sources for optical communications and optical memory systems, and broad-area semiconductor lasers are promising light sources for high power laser applications. Quantum-dot semiconductor laser is a new laser structure expected as a light source for highly coherent beam emission. The region of light emission from the laser is well confined in a certain spatial point in the active area, namely a quantum dot, and the energy levels related to light emission are perfectly quantized by a quantum-dot structure. Another example of recent semiconductor laser is quantum-cascade laser, which is a THz light source. Though a quantum-cascade laser is one of the semiconductor lasers, the laser structure and light emission process are completely different from other semiconductor lasers based on interband optical transitions. Such a laser also shows different dynamics from conventional semiconductor lasers. They have their own unique characteristic properties. Here, we do not discuss the details of each device structure and its characteristics, but we introduce the rate equations for such lasers and present their dynamic properties. These new laser structures have extra degrees of freedom and show instabilities and chaotic dynamics without any introduction of external perturbations. In this chapter, we discuss the dynamics of these new lasers both for solitary oscillations and external perturbations.

J. Ohtsubo, *Semiconductor Lasers*, Springer Series in Optical Sciences 111,
DOI: 10.1007/978-3-642-30147-6_8, © Springer-Verlag Berlin Heidelberg 2013

8.1 Multimode Lasers

8.1.1 Multimode Operation of Semiconductor Lasers

Before discussing the dynamics of semiconductor lasers with various structures different from narrow-stripe edge-emitting lasers, we show the rate equations for multimode operating narrow-stripe edge-emitting lasers. In the preceding chapters, semiconductor lasers were assumed to be operating at a single longitudinal mode, however, the laser sometimes oscillates at multimode due to noises when it is biased at a low injection current close to the threshold, otherwise it oscillates at multimode originating from their device structures even for a higher bias injection current. It intrinsically oscillates at multimode by the introduction of external perturbations such as optical external feedback. Figure 8.1 shows a multimode spectrum of a Fabry-Perot semiconductor laser operating close to the threshold. Even for a laser operating at a single mode with suppressed side mode, the side mode does not damp out by optical feedback or optical injection, and the laser dynamics are much affected by the mode behaviors as shown in Chap. 6. Semiconductor lasers at solitary condition may be operated with multimode as a nature of the device structure, since the laser has a broad gain bandwidth. The separation of the longitudinal modes of an ordinary semiconductor laser is more than 100 GHz (the corresponding wavelength separation is $\sim$1 nm) due to a short internal cavity length. However, the gain profile is as large as 20 nm or more and it has the possibility of multimodal oscillations with several oscillation lines. In semiconductor lasers of various device structures different from narrow-stripe edge-emitting lasers, they usually operate at multimode without any external perturbations, since they originally include extra variables (extra degrees of freedom) besides those for narrow-stripe edge-emitting lasers. We will discuss these dynamics later. Here, we first discuss the dynamics of narrow-stripe edge-emitting semiconductor lasers operating at multimode.

Semiconductor lasers have broad gain bandwidth, which is a unique feature different from other lasers. Therefore, there exist many possible oscillation lines within the bandwidth. The gain curve is sometimes assumed as a parabolic function, although, in actual fact, the gain profile has asymmetry. The gain for shorter wavelength (higher energy of carrier or higher frequency oscillation) tends to be large by the band-filling effects under the condition of constant temperature and carrier injection. Also, semiconductor lasers with multimode operation are much affected by this effect (Petermann 1988). The optical powers are equally distributed to respective modes below the laser threshold. However, the transfer of the power to the side modes is much restrained well above the threshold and the power of the main mode increases resulting in a single mode oscillation. This phenomenon is well reproduced from the calculations of the rate equations for taking into consideration the multimode effects and the theory and experiments show good coincidence. The effect of side mode suppression is strongly dependent on spontaneous emission of light and the large spontaneous emission coefficient β_{sp} forces the excitation of side modes.

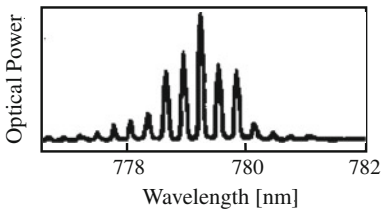

Fig. 8.1 Optical spectrum of a multimode Fabry-Perot semiconductor laser

8.1.2 Theoretical Model of Multimode Lasers

The rate equations for the photon number and the carrier density for multimode semiconductor lasers are given by the following equations (Petermann 1988):

$$\frac{\mathrm{d}S_j(t)}{\mathrm{d}t} = [G_{n,j}\{n(t) - n_{\mathrm{th},j}\}]S_j(t) + R_{\mathrm{sp}}(\omega_j) \tag{8.1}$$

$$\frac{\mathrm{d}n(t)}{\mathrm{d}t} = \frac{J(t)}{ed} - \frac{n(t)}{\tau_s} - \sum_{j=-M}^{M} G_{n,j}\{n(t) - n_0\}S_j(t) \tag{8.2}$$

where subscript j is for the jth mode and $2M+1$ is the total mode number. $j = 0$ is the main mode. The final term in (8.1) is the effect of spontaneous emission of light. It is noted that it is not only a function of time but also a function of optical frequency. For incoherent rate equations, we do not need to consider the phase equation, since it does not couple with the other equations. The above two equations are enough to describe the primary characteristics induced by multimode oscillations in a solitary laser. On the other hand, in an actual situation, we must consider the nonlinear saturation effect for the gain and the cross-saturation effect in the photon number rate equation. Further, we must use the complex field equation instead of the photon number rate equation, when we consider coherent effects such as optical feedback. For coherent phenomena, the phase equation plays a crucial role for the dynamics as has already been discussed. Such an instance will be treated later in this subsection.

At first, we study the side mode suppression ratio (MSR) in a multimode semiconductor laser. Assuming $2M+1$ oscillation lines within the gain profile and approximating the gain as a parabolic curve, the gain is written as

$$G_{n,j} = G_n \left\{1 - \left(\frac{j}{M}\right)^2\right\} \tag{8.3}$$

where $M = \Delta\nu_g/\Delta\nu_l$, $\Delta\nu_g$ is the frequency width of the gain profile and $\Delta\nu_l$ the frequency of the longitudinal mode spacing. The laser output power of the jth mode for the steady-state solution is calculated from the rate Eqs. (8.1) and (8.2) as (Petermann 1988; Agrawal and Dutta 1993)

$$S_j \approx \frac{R_{\rm sp}(\omega_j)}{\frac{1}{\tau_{\rm ph}} - G_{n,j}(n_s - n_0)} \approx \frac{\tau_{\rm ph} R_{\rm sp}(\omega_j)}{\delta + \left(\frac{j}{M}\right)^2} \tag{8.4}$$

where n_s and n_0 is the steady-state value of carrier density and carrier number at transparency, and $\delta = 1 - G_n \tau_{\rm ph}(n_s - n_0) = \tau_{\rm ph} R_{\rm sp}/S_0$. Note that the relation $G_n \tau_{\rm ph}(n_s - n_0) \approx 1$ is used for the final form of (8.4). From this relation, we obtain the side mode suppression ratio as

$$\text{MSR} = \frac{S_0}{S_1} = 1 + \frac{1}{\delta M^2} = 1 + \frac{S_0}{\tau_{\rm ph} R_{\rm sp}} (\frac{\Delta \nu_l}{\Delta \nu_g})^2 \tag{8.5}$$

For a semiconductor laser which is assumed to be a single mode operation, the value of MSR is larger than 20.

A single mode operation at a high bias injection current is expected for index-guided semiconductor lasers, since the spontaneous emission coefficient is as small as less than $\beta_{\rm sp} \sim 10^{-4}$. However, the side mode suppression is weak for gain-guided semiconductor lasers with a larger spontaneous emission coefficient of $\beta_{\rm sp} \sim 10^{-3}$ and the laser tends to be oscillated with multimode. As a primary effect, a side mode is suppressed for the increase in the injection current above the threshold and the optical power is concentrated to the main mode. In actual laser oscillation, there are effects of spatial hole-burning due to standing-wave nature along the laser propagation and spectral hole-burning due to the broadening of the gain profile for the increase in the optical power. As results, the side mode is suppressed and the optical power is transferred to the main mode (Agrawal and Dutta 1993). These effects cause instabilities for the main mode and play an important role for chaotic dynamics in semiconductor lasers. Similar effects are observed for optical injection to semiconductor lasers as shown in Fig. 6.5. Other effects to destabilize the main mode and enhance the side modes are the beating between the main and side modes and the four-wave mixing in the oscillation modes. The effects are strongly dependent on laser types, materials, and confinement of light in the active layer.

We have derived the multimode rate equations for semiconductor lasers in the incoherent case. However, we must take into account the effects of the nonlinear gain saturation and cross-gain saturation. Also, we must use the coherent rate equations for a semiconductor laser when the laser is subjected to external optical feedback or optical injection. When a semiconductor laser oscillates at a multimode with $2M+1$ oscillation lines, the rate equations for the complex field and the carrier density are written as (Ryan et al. 1994)

$$\begin{aligned}\frac{{\rm d}E_j(t)}{{\rm d}t} &= \frac{1}{2}(1 - i\alpha) G_{n,j}\{n(t) - n_{{\rm th},j}\} E_j(t) \\ &\quad - \frac{1}{2}\left(\varepsilon_{sj}|E_j(t)|^2 + \sum_{m=-M}^{M} \theta_{mj}|E_m(t)|^2\right) E_j(t)\end{aligned} \tag{8.6}$$

Table 8.1 Characteristic device parameters for a multimode semiconductor laser at an oscillation wavelength of 780 nm (GaAs-GaAlAs laser)

Symbol	Parameter	Value
G_n	gain coefficient	$2.05\times10^{-13}\,\mathrm{m^3\,s^{-1}}$
α	linewidth enhancement factor	4.00
r_0	facet reflectivity	0.556
n_{th}	carrier density at threshold	$4.00\times10^{24}\,\mathrm{m^{-3}}$
n_0	carrier density at transparency	$1.40\times10^{24}\,\mathrm{m^{-3}}$
τ_s	lifetime of carrier	2.00 ns
τ_{ph}	lifetime of photon	1.88 ps
τ_{in}	round trip time in laser cavity	6.00 ps
V	volume of active region	$1.25\times10^{-16}\,\mathrm{m^3}$
ε_{sj}	nonlinear self-saturation coefficient	$1.70\times10^{4}\mathrm{s^{-1}}$
θ_{mj}	nonlinear cross-saturation coefficient	$1.60\times10^{3}\mathrm{s^{-1}}$

$$\frac{\mathrm{d}n(t)}{\mathrm{d}t}=\frac{J}{ed}-\frac{n(t)}{\tau_s}-\sum_{m=-M}^{M}[K_m G_{n,m}\{n(t)-n_0\}]|E_m(t)|^2 \tag{8.7}$$

where $E_j(t)$ is the field of the jth mode, ε_{sj} and θ_{mj} $(m=j)$ are the nonlinear self- and cross-saturation coefficients, respectively, and K_m is the mode gain coefficient. We omitted the Langevin noise terms in (8.6), however, it may be added where necessary.

The nonlinear saturation coefficient $\alpha'=-(\partial\mathrm{Re}[\chi]/\partial S)/(\partial\mathrm{Im}[\chi]/\partial S)$ for the photon number discussed in Sect. 6.2 is ignored in the above equation. The saturation coefficients ε_{sj} and θ_{mj} do not have large values and they are in the order of $10^4\ \mathrm{s^{-1}}$. In the carrier density equation, we also ignore the mode interferences for the carrier recombination because it has small effects. A semiconductor laser operating at multimode is an unstable laser and it is easily affected by external perturbations. A multimode semiconductor laser shows mode competitions and mode switching induced by the nonlinear interactions among the modes. Mode partition noise is one of the dominant effects in multimode oscillating lasers and it is a non-negligible effect (Ahamed and Yamada 2002). Each oscillation mode includes a very large relative intensity noise (RIN) and it sometimes causes problems in actual use. However, as a total intensity, a multimode semiconductor laser with partition noise has the same order of RIN as a single mode laser, since the partition noises are averaged out (Petermann 1988). Using (8.6), the rate equation for the complex field in a multimode semiconductor laser with optical feedback is given by

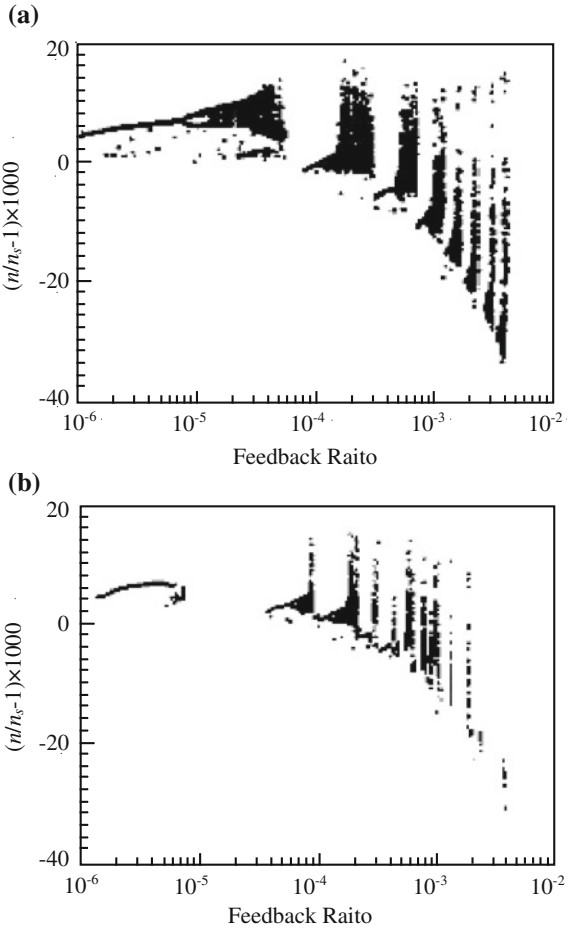

Fig. 8.2 Bifurcation diagrams of carrier density for optical feedback rate. **a** Single mode laser. **b** Multimode laser with five oscillation lines. The external cavity length is $L = 10\,\text{cm}$, which corresponds to a frequency of 1.5 GHz. The relaxation oscillation frequency of the laser is assumed as 0.7 GHz. The same device parameters are assumed for both cases [after Ryan et al. (1994); © 1994 IEEE]

$$\frac{\mathrm{d}E_j(t)}{\mathrm{d}t} = \frac{1}{2}(1-i\alpha)G_{n,j}\{n(t)-n_{\mathrm{th},j}\}E_j(t) - \frac{1}{2}\left(\varepsilon_j|E_j(t)|^2 + \sum_{m=-M}^{M}\theta_{mj}|E_m(t)|^2\right)E_j(t) + \frac{\kappa_j}{\tau_{in}}E_j(t-\tau)\exp(i\omega_j\tau) \tag{8.8}$$

In the following, the dynamics of multimode semiconductor lasers subjected to external optical feedback are numerically investigated. Table 8.1 shows typical values of device parameters for a multimode semiconductor laser frequently used in numerical simulations (Ryan et al. 1994).

8.1.3 Dynamics of Multimode Semiconductor Lasers with Optical Feedback

When the frequency corresponding to the round-trip time of light in the external cavity is small enough compared with the relaxation oscillation frequency, the difference in the dynamics between single mode and multimode semiconductor lasers is not distinct. However, if the external cavity length becomes short and the corresponding frequency exceeds the relaxation oscillation frequency, they show different dynamics. Figure 8.2 shows an example of the difference. Bifurcation diagrams in the phase space of the carrier density and the external feedback rate are calculated both for single mode and multimode semiconductor lasers (Ryan et al. 1994). For the multimode laser, five modes are assumed. In Figs. 8.2a, b, the multimode laser is stable compared with the single mode laser and a feedback level of ten times larger than the solitary case is required to destabilize the laser. Namely, the multimode semiconductor laser is less sensitive to optical feedback than the single mode semiconductor laser as far as the conditions of the device parameters are the same. This result can be understood qualitatively by noting that all modes contribute to the damping of relaxation oscillations. Even though an individual mode may be unstable in solitary oscillation, simultaneous lasing of all modes preserves the steady state over a large range of the external feedback. The situation is quite similar to the effect of averaged RIN in multimode semiconductor lasers (Petermann 1988). Also, chaotic regions are much thinner compared to the single mode case.

At chaotic oscillations of a multimode semiconductor laser, the bifurcation diagrams cannot tell us whether all of the modes simultaneously oscillate, or whether one of the modes, or a small number of them are the dominant oscillation modes. Figure 8.3 shows the simulation result for waveforms of each oscillation mode in a multimode semiconductor laser (Ryan et al. 1994). Figure 8.3 is the calculations of waveforms without and with optical feedback. Each waveform is averaged for a 10 ns time window to clearly show the difference. Switching among the modes is not distinct for the solitary oscillation, although the change of the main mode for the time evolution is visible as shown in Fig. 8.3a. The solitary laser exhibits mode partition fluctuations, but it remains multi-moded most of the time. The total optical power at the solitary oscillation is almost constant for time. However, in Fig. 8.3b, only one of the modes is dominant for a certain time duration and the other mode is suppressed, when the laser shows chaotic dynamics induced by the optical feedback. The main mode changes to the other mode after a certain time duration in a random manner. At the moment of mode hopping, the total output power sustains irregular spikes. Switching among modes is a typical feature of multimode semiconductor lasers subjected to optical feedback. From the detailed study of the dynamics, it is understood that only one or few of the possible oscillation modes become the dominant mode for a certain time duration and the modes alternately switch in a random manner. When the mode number is small, only one mode tends to oscillate in chaotic manner and oscillations of the other modes are suppressed. Especially, a mode of shorter wavelength tends to show chaotic oscillations for small optical feedback due to the

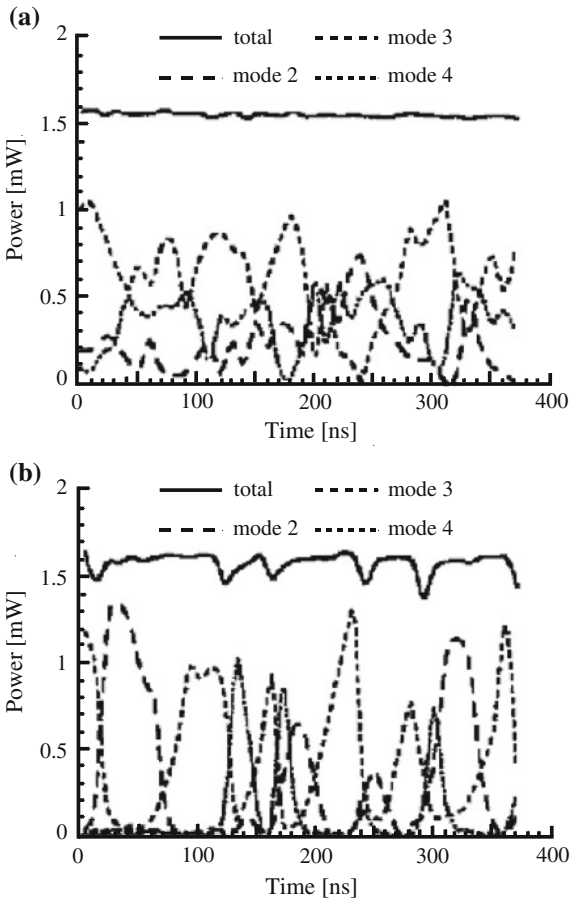

Fig. 8.3 Waveform of each mode in a multimode semiconductor laser corresponding to Fig. 8.2. Three modes are displayed. **a** Almost steady-state oscillation without optical feedback and **b** chaotic oscillation with optical feedback. The intensity feedback ratio is 5×10^{-4} [after Ryan et al. (1994); © 1994 IEEE]

asymmetry of the gain profile. Indeed, this mode switching has been experimentally observed (Ikuma and Ohtsubo 1998).

8.2 Self-Pulsating Lasers

8.2.1 Theory of Self-Pulsating Lasers

Self-pulsating semiconductor lasers are used as light sources for digital versatile disks (DVD) in optical data storage systems, since noises (actually chaotic irregular oscillations) induced by optical feedback from a disk surface are greatly suppressed by self-pulsations. Also, a technique of high frequency injection current modulation

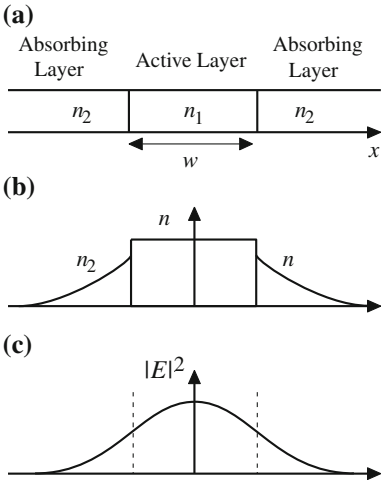

Fig. 8.4 Model of self-pulsating semiconductor lasers. **a** Cross-section of the front facet of the laser, **b** carrier distribution, and **c** optical profile. The center is the active region and both sides of the active layer are the carrier absorbing regions

in CW operating semiconductor lasers is used to reduce optical feedback noises in optical disk systems. Self-pulsating semiconductor lasers are fabricated to reduce feedback noises using pulsation oscillations originating from their device structures without external control circuits. The pulsation frequency depends on each device and the bias injection current, and ranges typically from several hundreds of MHz to the order of GHz. The self-pulsation semiconductor laser itself is unstable and sometimes shows instability for a certain region of the bias injection current even without external perturbations. The structure of self-pulsation lasers is almost the same as edge-emitting lasers except for saturable absorbing regions adjacent to the active layer as shown in Fig. 8.4. The width of the active region is usually the same size as that of edge-emitting semiconductor lasers. However, this is not the only structure of self-pulsating semiconductor lasers. The other example is a type of weak index guide (WIG) and the saturable absorbing layer is installed above the active region. The type of adjacent saturable absorbing layers (SALs) shown in Fig. 8.4 is assumed in the following discussion. However, the results are straightforwardly applicable to the WIG model.

In Fig. 8.4a the cross-section of the front facet of a self-pulsating semiconductor lasers is represented. The saturable absorbing regions are installed at both sides of the active layer. Figure 8.4b is the carrier distribution along the active layer. The size of the active region has almost the same dimension as that of common narrow-stripe edge-emitting semiconductor lasers. Carriers injected into the active region rapidly decay out to the regions of the saturable absorbers. Figure 8.4c is the profile of the output power at lasing oscillation. The whole distributions of the carriers and the optical power from the active layer to the saturable absorbing regions are determined by the boundary conditions in the same manner as the treatment of the light transmission in an optical wave guide (Yamada 1993). The time constant τ_{12} of the carrier diffusion from the active layer to the absorbers is given as

$$\tau_{12} = \frac{w^2}{2D} \tag{8.9}$$

where w is the width of the active layer and D is the diffusion constant. At the same time, the carrier diffusion also occurs from the saturable absorbing regions to the active layer. Since the total number of the electrons $V_1 n_1 + V_2 n_2$ should be unchanged, the time constant τ_{21} of the carrier diffusion from the absorbers to the active layer is given as

$$\tau_{21} = \frac{V_2}{V_1}\tau_{12} \tag{8.10}$$

where V_1 and V_2 are the volumes of the active and absorbing regions, and n_1 and n_2 are the carrier densities at the active and absorbing regions, respectively. The linearized gains for the active and absorbing regions have different values, therefore we must use appropriate gains for them in the numerical simulations. Also, the carrier densities above which the lasing gain becomes positive, i.e., transparent, differ from each other.

Before introducing the rate equations for self-pulsating semiconductor lasers, the mechanism of self-sustained pulsating oscillations in a SAL type laser is briefly explained. At the carrier number less than the laser threshold, carriers are accumulated in the active region by the carrier injection. When the carrier number exceeds the laser threshold, the laser oscillation starts. The carriers are rapidly absorbed by the diffusion to the saturable absorbing regions. The carrier diffusion is reduced due to the increase of the carrier number in the saturable absorbing regions, and this results in the increase of the photon number. However, the increase of the photon number causes the depletion of carriers in the active region and the decrease of the carrier number is accelerated by the diffusion of the carriers to the saturable absorbing regions. Then, the carrier number falls below the laser threshold and, finally, the laser oscillation stops. After the halt of the laser oscillation, the carrier number again increases and the next pulsating oscillation starts. This process repeats again and again and the laser shows self-sustained pulsation oscillations. The accumulation time of carriers to show lasing oscillation is typically about 1 ns (corresponding to a pulsating oscillation frequency of 1 GHz) and the width of the pulses is $\sim$100 ps.

In the following, we assume a single mode oscillation for a self-pulsating semiconductor laser, however, actual lasers are more or less multimode oscillations. Therefore, the dynamics derived from the theory do not always coincide well with the experimental results unlike in the cases of narrow-stripe edge-emitting lasers. However, we can discuss approximate characteristics of self-pulsating semiconductor lasers, such as pulsating oscillations, pulsing frequency, and L-I characteristics. Several theoretical models have been proposed and some of them are listed in the reference (Carr and Erneux 2001), although the fundamental idea of the models is the same. Here, we assume a single mode model for a self-pulsating semiconductor laser and we introduce an additional carrier density equation for the saturable absorbing regions of the rate equations in a narrow-stripe edge-emitting semiconductor laser (Yamada 1993, 1996). Due to the presence of the saturable absorbing regions,

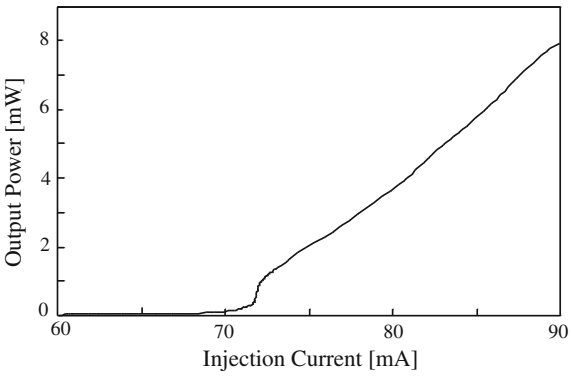

Fig. 8.5 L-I characteristic of a self-pulsating semiconductor laser. The laser is an AlGaInP multi-quantum well laser operating at a wavelength of 650 nm and a maximum output power of 5 mW

carriers in the active region rapidly decay toward the absorbing regions and pulsations occur in the laser output. In such a structure, we must take into account the carrier density equations in the absorbing regions.

The rate equations for the complex amplitude E and the carrier densities n_1 and n_2 for the active and absorbing regions describing self-pulsation semiconductor lasers are written as

$$\frac{\mathrm{d}E(t)}{\mathrm{d}t} = \frac{1}{2}(1 - i\alpha)[G_{n1}\{n_1(t) - n_{\mathrm{th1}}\} + G_{n2}\{n_2(t) - n_{\mathrm{th2}}\}]E(t) \tag{8.11}$$

$$\frac{\mathrm{d}n_1(t)}{\mathrm{d}t} = \frac{J}{ed} - \frac{n_1(t)}{\tau_{s1}} - \frac{n_1(t) - n_2(t)}{\tau_{12}} - G_{n1}\{n_1(t) - n_{01}\}|E(t)|^2 \tag{8.12}$$

$$\frac{\mathrm{d}n_2(t)}{\mathrm{d}t} = -\frac{n_2(t)}{\tau_{s2}} - \frac{n_2(t) - n_1(t)}{\tau_{21}} - G_{n2}\{n_2(t) - n_{02}\}|E(t)|^2 \tag{8.13}$$

Here, subscripts 1 and 2 denote the quantities for the active and absorbing regions, respectively, and τ_{12} and τ_{21} are the carrier diffusions from regions 1–2 and vice versa, respectively, as has already been defined. In the field equation, we ignored the nonlinear gain saturation effect. However, it may play an important role in self-pulsating semiconductor lasers, since the photon density becomes large due to pulsating oscillations even for a short time duration. We take into account the nonlinear gain in such a case as discussed in Sect. 3.3.4. However, we can simulate approximate characteristics of self-pulsating semiconductor lasers without considering the gain saturation effect and the term is sometimes omitted. Self-pulsation semiconductor lasers were originally aimed to reduce the effect of optical feedback noises, however, the RIN is sometimes enhanced under certain conditions of the feedback. Furthermore, they are essentially unstable lasers and they sometimes show unstable or chaotic oscillations under certain ranges of the bias injection current even at solitary oscillations.

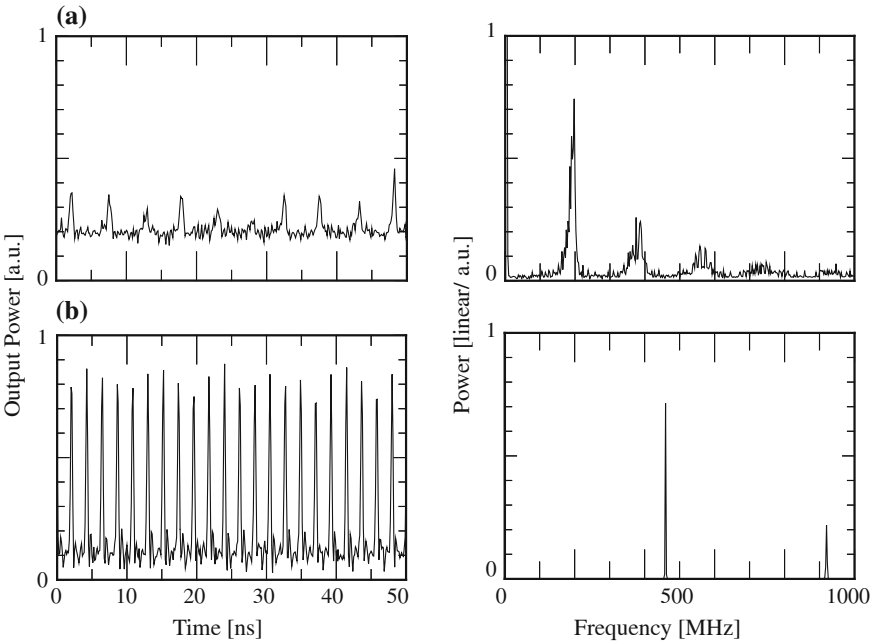

Fig. 8.6 Waveforms and rf spectra in Fig. 8.5. **a** Unstable region at a bias injection current of 74 mA and **b** stable regular pulsating oscillation at 80 mA

8.2.2 Instabilities at Solitary Oscillations

The self-pulsating semiconductor laser itself is an unstable laser and regular pulsating oscillation is considered as a kind of period-1 state on the way to chaotic evolution. Typical features of chaotic states in a self-pulsating semiconductor laser are pulsing oscillations with irregular pulse amplitude and jitters. The characteristics of self-pulsating semiconductor lasers are strongly dependent on the device structure and parameters. Figure 8.5 shows an example of an experimental L-I characteristic of a self-pulsating semiconductor laser at solitary oscillation. The laser is a SAL type and has a maximum output power of 5 mW with an oscillation wavelength of 650 nm. The oscillation above the threshold is divided into unstable and stable regions for the bias injection current. The threshold current is about 70 mA, which is much higher than that of ordinary narrow-stripe edge-emitting semiconductor lasers, because the strong carrier dissipation exists due to the presence of the saturable absorbing regions. Another difference is the vague threshold. The laser power does not linearly increase for the bias injection current close to the threshold, but it has a hysteresis. As demonstrated later, bistability is reproduced by the numerical simulations from the rate equations.

In the L-I characteristic, the laser output shows the bistable state above the threshold. In this region, the laser exhibits pulsating oscillation, but it is unstable. A

Table 8.2 Characteristic device parameters for a self-pulsating semiconductor laser at an oscillation wavelength of 650 nm (AlGaInP laser)

Symbol	Parameter	Value
G_{n1}	gain coefficient in active region	$3.08 \times 10^{-12}\ \mathrm{m^3 s^{-1}}$
G_{n2}	gain coefficient in satruable absorbing region	$1.24 \times 10^{-13}\ \mathrm{m^3 s^{-1}}$
α	linewidth enhancement factor	4.00
n_{01}	carrier density at transparency in active region	$1.40 \times 10^{24}\ \mathrm{m^{-3}}$
n_{02}	carrier density at transparency in satuarble absorbing region	$1.60 \times 10^{24}\ \mathrm{m^{-3}}$
τ_{s1}	lifetime of carrier in active region	2.49 ns
τ_{s2}	lifetime of carrier in saturable absorbing region	1.25 ns
τ_{12}	diffusion time	2.65 ns
τ_{ph}	lifetime of photon	2.72 ps
V_1	volume of active region	$0.72 \times 10^{-16}\ \mathrm{m^3}$
V_2	volume of saturable absorbing region	$0.46 \times 10^{-16}\ \mathrm{m^3}$

waveform and its rf spectrum in this region are plotted in Fig. 8.6a. The pulse peak changes irregularly and the waveform shows a broad chaotic spectrum. Well above the laser threshold, the laser shows regular pulsing states with constant peak and separation as shown in Fig. 8.6b. However, even for such stabilized operations at solitary mode, the laser may be destabilized by optical feedback. Stability or instability of the laser operations for optical feedback is discussed in the next subsection. It is noted that every self-pulsating semiconductor laser does not always show the same L-I characteristics as in Fig. 8.5. A laser with regular pulsing states is suitable for a read-light source in DVD systems to avoid optical feedback from a disk surface.

The L-I characteristic is numerically calculated from the rate Eqs. (8.11)–(8.13). Typical parameter values of red light self-pulsating semiconductor lasers are listed in Table 8.2. Because of the pulsation characteristics of laser oscillations, the values of the gain coefficients are larger than those of narrow-stripe edge-emitting semiconductor lasers. Figure 8.7 is an example of the calculated L-I characteristic (van Tartwijk and San Miguel 1996). After the lasing oscillations, the laser shows bistability for the bias injection current between 48 and 58 mA and chaotic pulsating oscillations are observable in this region. For the bias injection current from 58 to 125 mA, the laser oscillates at stable regular pulsing states. Over the bias injection current of 125 mA, the laser shows stable CW oscillations. In the numerical simulations, noises induced by spontaneous emission strongly affect the pulsing frequency. At regular pulsing states without considering noises, the pulsing frequency smoothly increases with the increase of the bias injection current. In the presence of noises, a kink is observed in the characteristic curve of the pulsing frequency and the bias injection current (van Tartwijk and San Miguel 1996; Mirasso et al. 1999).

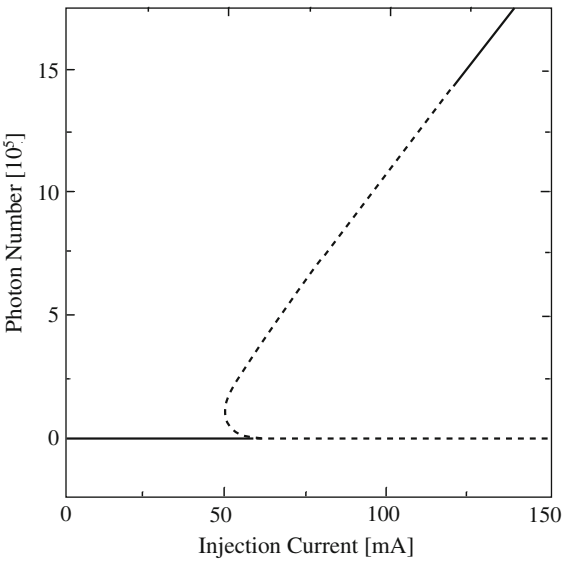

Fig. 8.7 Theoretically calculated L-I characteristic of a self-pulsating semiconductor laser [after van Tartwijk and San Miguel (1996); © 1996 IEEE]

The theoretical calculation in Fig. 8.7 well reproduces the behaviors of unstable and stable pulsating oscillations. However, the CW operation of self-pulsating lasers is not observable in experiments. The CW operation in Fig. 8.7 is achieved at a high bias injection current and such a high bias injection current may damage the laser. Another example of discrepancy between the theory and the experiment is the pulse width of the waveform. The theoretically calculated pulse width is much smaller than the actual width. For example, the calculated pulse width is typically 10 ps, but the observed pulse usually has a width of around 100 ps. As has already been mentioned, the improvement of the theoretical model of the rate equations is still required to explain well the experimental data (Yamada 1998b). The other reason for the discrepancy is the assumption of a single mode operation for self-pulsating lasers. It is well known that self-pulsating semiconductor lasers oscillate at multimode with many oscillation lines.

Characteristics of InGaN self-pulsating semiconductor lasers with an operating wavelength of 395 nm have been investigated (Tronciu et al. 2003). Since the difference between the carrier lifetimes of the active and saturable absorbing layers is much greater than that of red light self-pulsating semiconductor lasers, the lasers show quite different dynamics from red self-pulsating lasers. For example, the carrier lifetime of the active layer is 2.0 ns, while that of the saturable absorbing layer is only 0.1 ns. The rate equations are fundamentally the same as those in (8.11)–(8.13), but Tronciu et al. took into account the effects of the outer regions besides the active and absorbing layers in the numerical simulations. Figure 8.8 shows some numerical and experimental results. They used the model of a WIG-type laser. Close to the threshold, the laser oscillates at the CW operation without hysteresis like in Fig. 8.8a, which is quite different from the operation of red self-pulsating lasers. At a certain

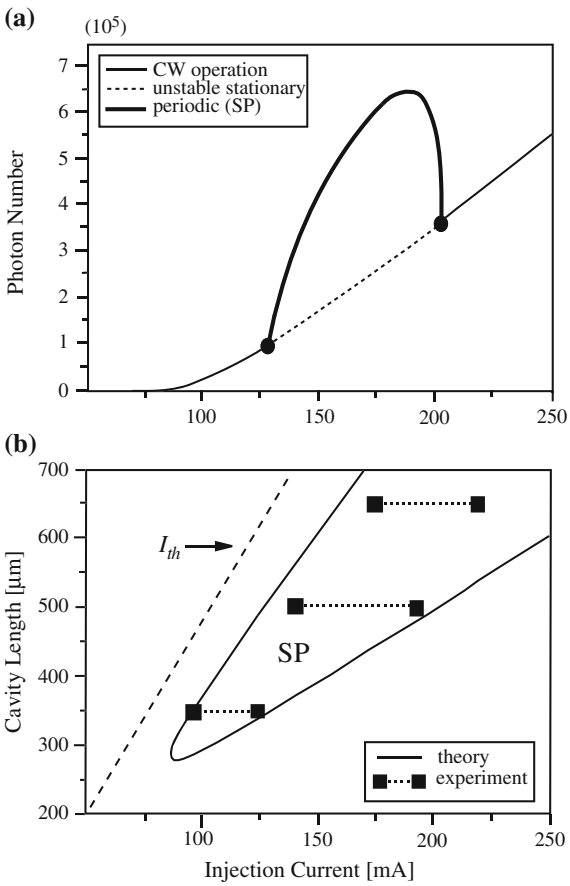

Fig. 8.8 Characteristics of an InGaN self-pulsating semiconductor laser with an oscillation wavelength of 395 nm. **a** Calculated bifurcation diagram for a laser cavity length of 500 μm. The self-pulsation region is observable from 125 to 200 mA. The other range of the injection current is a stable CW operation. **b** Self-pulsation range in the plane of laser cavity length versus injection current. Experimentally obtained ranges of the self-pulsation are indicated with *dotted lines* [after Tronciu et al. (2003); © 2003 IEEE]

bias injection current, the laser at first shows self-pulsating oscillation. However, the laser recovers stable states for a bias injection current above 200 mA. The dynamics is strongly dependent on the laser cavity length. The self-pulsation range (SP) for the laser cavity length is investigated in Fig. 8.8b. We can see the agreement between the theoretical and experimental results.

8.2.3 Instability and Chaos by Optical Feedback

The self-pulsating semiconductor laser is fabricated as a low noise light source in optical data storage systems. However, the reduction of feedback noise is not always achieved for every feedback condition. The self-pulsating semiconductor laser has a periodic pulsation with a frequency ranging from several hundreds MHz to GHz depending on the bias injection current. There is a congenial range of optical feedback

lengths to suppress feedback noise. The self-pulsating semiconductor laser sustains a forced oscillation due to the device structure and the feedback noise is reduced for a wide range of the feedback conditions. On the other hand, outside this region, the laser undergoes more noises than that of edge-emitting semiconductor lasers. Also, the laser shows chaotic behaviors for the modulation under certain bias injection current ranges. At first, we consider feedback induced noises in a self-pulsating semiconductor laser. There are two schemes of optical feedback in self-pulsating semiconductor lasers; coherent and incoherent feedback depending on the relation between the pulse separation and the feedback length. When the feedback length is small enough compared with the pulsing separation and close or less than the pulse width, the effect is coherent. For the condition $T_p > \tau$ (T_p being the pulse separation), the rate equation for the complex field is given by

$$\frac{\mathrm{d}E(t)}{\mathrm{d}t} = \frac{1}{2}(1 - i\alpha)[G_{n1}\{n_1(t) - n_{\mathrm{th1}}\} + G_{n2}\{n_2(t) - n_{\mathrm{th2}}\}]E(t) + \frac{\kappa}{\tau_{in}}E(t - \tau)\exp(i\omega_0\tau) \tag{8.14}$$

The equation is the same as that for the coherent case of narrow-stripe edge-emitting semiconductor lasers except for the effects of the gain term in the saturable absorbing regions. The rate equations for the carrier densities under coherent feedback remain unchanged as in (8.12) and (8.13).

On the other hand, the rate equation of the complex field is written the same as (8.11) for incoherent optical feedback, however, the carrier density equation for the active layer in (8.12) must be changed and the incoherent feedback term is added to this equation, when $T_p < \tau$. The rate equation for the carrier density is given as

$$\frac{\mathrm{d}n_1(t)}{\mathrm{d}t} = \frac{J}{ed} - \frac{n_1(t)}{\tau_{s1}} - \frac{n_1(t) - n_2(t)}{\tau_{12}} - G_{n1}\{n_1(t) - n_{01}\} \times \{|E(t)|^2 + \kappa_i(1 - R_0^2)R|E(t - \tau)|^2\} \tag{8.15}$$

where R_0 and R are the intensity reflectivities of the front facet of the laser and the external reflector, respectively, and κ_i is the intensity coupling coefficient to the active layer.

We show some numerical results for the dynamics of self-pulsating semiconductor lasers subjected to coherent optical feedback. Figure 8.9 is an example (Yamada 1998a,b). Figure 8.9a shows the time series of the laser oscillation without optical feedback. In the figure, n_1 and n_2 are the carrier densities of the active and saturable absorbing regions, respectively, and S is the photon number. n_4 is the carrier density at the current blocking region installed above the saturable absorbing layer. The laser oscillates at the regular pulsing state and the pulsing frequency is 1.29 GHz. The calculated RIN at the solitary oscillation is less than −130 dB/Hz for the lower frequency component. Figure 8.9b shows the waveforms for the same variables under optical feedback. The feedback ratio is set to be 3.3 % in the average field amplitude. In the presence of optical feedback, the laser still shows a pulsating oscillation.

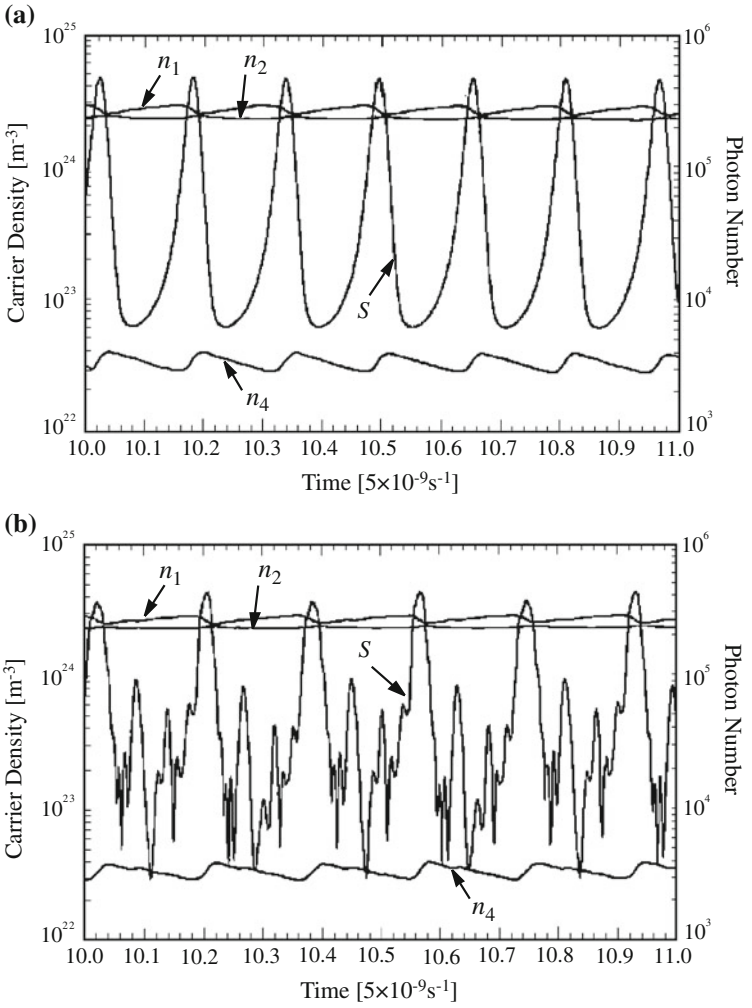

Fig. 8.9 Times series of the variables in a self-pulsating semiconductor laser at $J = 1.69 J_{\text{th}}$. **a** Without optical feedback and **b** with optical feedback of 3.3 % of the average field amplitude. The external cavity length is $L = 4$ cm. n_1: carrier density in active region, n_2: carrier density in saturable absorbing region, n_4: carrier density in current blocking region, and S: photon number [after Yamada (1998a); © 1998 IEICE]

However, the laser output power is disturbed by the feedback and the laser shows a chaotic oscillation. The pulse period is larger than that of the solitary oscillation and its average frequency is 1.07 GHz. It is noted that the pulse height also fluctuates and the RIN is greatly enhanced up to −90 dB/Hz for the lower frequency component.

van Tartwijk and San Miguel (1996) numerically studied the effects of optical feedback in self-pulsating semiconductor lasers and calculated pulse periods and

jitters (the standard deviation from the average period) without and with optical feedback. As results, the pulse period decreases with the increase of the bias injection current and, at the same time, the jitter becomes small. Increasing the feedback time, the pulse period increases and, then, a sudden jump-down is observed at a certain feedback distance. The jump in the pulse period must be attributed to a switch of the locked-pulse frequency to a neighboring compound cavity mode, i.e., the resulting resonance frequency of the laser mode with relaxation oscillations and one of the external cavity resonance frequencies. A similar trend can be observed for the pulse jitter. There is also phase sensitivity of coherent optical feedback in a self-pulsating semiconductor laser as expected from (8.14). When the feedback is small, the pulse period keeps almost the same value as that of the solitary oscillation. However, the jitter has the minimum value at a certain small feedback ratio. The increase in jitter after the optimum value manifests itself by a multi-peaked, very broad pulse period distribution. The effects agree well with the period-doubling route to chaos (Kuznetsov et al. 1986). The dynamics of coherent optical feedback is extensively studied in self-pulsating semiconductor lasers, because the lasers are used as light sources for DVD systems in which the optical feedback length is typically within several centimeters. On the other hand, the typical feedback length is several tens of centimeters to meters when the lasers are used as light sources for optical measurements. The effects for this range are incoherent.

8.2.4 Instability and Chaos by Injection Current Modulation

A few studies have been reported for the modulation properties of self-pulsating semiconductor lasers. The lasers show unstable oscillations by the modulation to the bias injection current, and also exhibit chaotic behaviors at large modulation index. For the variations of irregular pulse peaks, we can see similar chaotic bifurcations to those in ordinary narrow-stripe edge-emitting semiconductor lasers such as discussed in Chap. 7 (Winful et al. 1986; Juang et al. 1999, 2000; Jones et al. 2001). It is shown that the occurrence of chaotic oscillations is critically dependent on the modulation frequency. Periodic bands of chaotic dynamics are found to exist at multiples of the relaxation oscillation frequency. Not only stable pulsations resonance to the modulation frequency (locking oscillation), but also unstable pulsations and unique frequency-locked pulsations in which multiple spikes appear within some modulation period are found.

Fukushima et al. (2002) investigated experimentally and theoretically the dynamics of self-pulsating semiconductor lasers with injection current modulated and observed chaotic bifurcations for the pulsation frequency and the pulse height. Figure 8.10 shows some typical output waveforms observed by the experiments. The scales in the figure denote the period of modulation. The modulation index for the bias injection current is set to be $m = 1.06$. Each periodic state is defined as P_k^l, where k stands for the ratio of the fundamental period of the pulse train to the modulation period and l stands for the number of spikes in the fundamental period

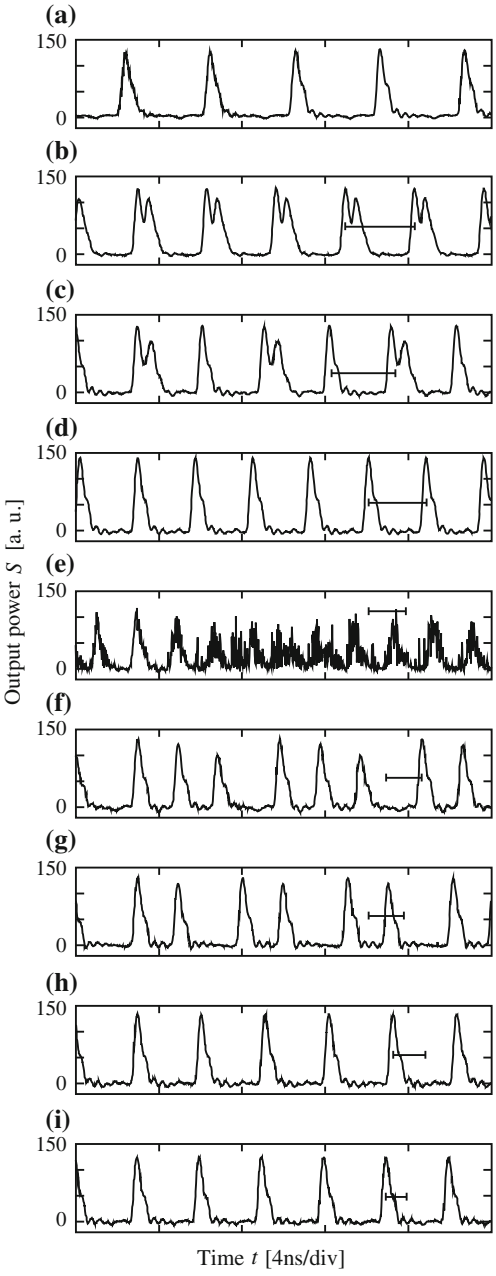

Fig. 8.10 Experimentally observed temporal waveforms of the output optical pulses at a bias injection current of 59.5 mA and a modulation index of $m = 1.06$. **a** Without rf modulation, **b** P_1^2 pulsation at $f_m = 300.0$ MHz, **c** P_2^3 pulsation at $f_m = 327.0$ MHz, **d** P_1^1 pulsation at $f_m = 360.0$ MHz, **e** unstable pulsation at $f_m = 562.0$ MHz, **f** P_4^3 pulsation at $f_m = 584.0$ MHz, **g** P_3^2 pulsation at $f_m = 592.0$ MHz, **h** P_2^1 pulsation at $f_m = 650.0$ MHz, and **i** P_3^1 pulsation at $f_m = 1000.0$ MHz. The *bar* in each plot is the fundamental period of the modulation [after Fukushima et al. (2002); © 2002 JSAP]

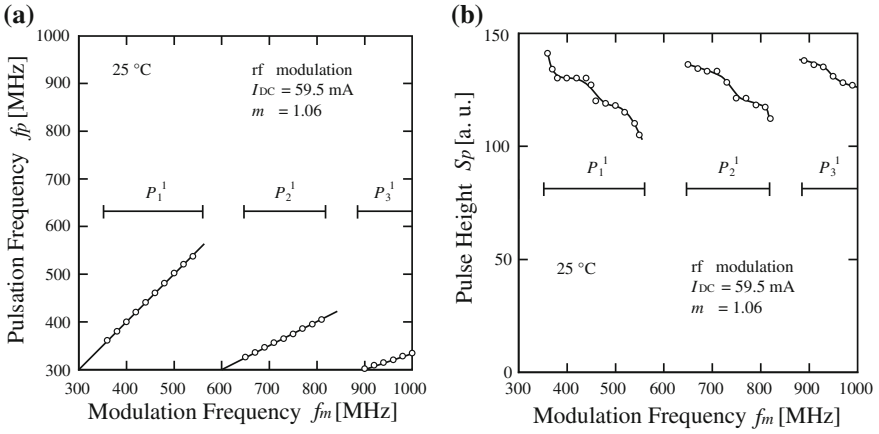

Fig. 8.11 **a** Characteristics of pulsation frequency versus modulation frequency under rf modulation. **b** Dependence of the pulse height on the modulation frequency under the frequency-locked pulsations of P_1^1, P_2^1, and P_3^1 [after Fukushima et al. (2002); © 2002 JSAP]

of the pulse train. Without rf modulation, the laser shows stable pulsation at a self-pulsation frequency of 245.7 MHz, as shown in Fig. 8.10a. Under rf modulation, as the modulation frequency f_m increases, the output optical pulse train is locked to the modulation frequency (P_1^1 pulsation) or its subharmonics (P_2^1 and P_3^1 pulsations) as shown in Fig. 8.10d, h, and i. In the boundary regions of these frequency-locked pulsations, unstable pulsation occurs as shown in Fig. 8.10e. It is speculated that the unstable region contains both quasi-periodic pulsation and chaotic pulsation. In the boundary regions, unique frequency-locked pulsations are also observed. One is P_1^2 pulsation in which two spikes appear within one modulation period, as shown in Fig. 8.10b. Another is P_2^3 pulsation in which two spikes and a single spike appear alternately. The others are P_4^3 and P_3^2 pulsations in which three or two spikes appear within four or three modulation periods as shown in Fig. 8.10f, g, respectively.

The experimental results are summarized in Fig. 8.11. Figure 8.11a shows the characteristics of pulsation frequency versus modulation frequency. The figure shows the regions of frequency-locked states for the modulation frequency. In between the frequency-locked states for the modulation frequency, we can observe unstable and chaotic oscillations as shown in Fig. 8.11e. Figure 8.11b shows the dependence of the pulse height on the modulation frequency under P_1^1, P_2^1, and P_3^1 pulsations. Under P_1^1 pulsation, the pulse height decreases gradually as the modulation frequency increases and eventually the pulsation becomes unstable at the modulation frequency of 560 MHz. Then P_2^1 pulsation occurs at 647 MHz. Here, the pulse height again returns to a high level. The same phenomenon is observed under P_2^1 and P_3^1 pulsations. The modulation index used in this experiment is rather high. However, similar trends in those results were obtained for lower modulation index, although each region of frequency-locked state shifts for lower modulation frequency. Fukushima et al. (2002) also compared the theoretical results with those experiments and demonstrated

that the theory based on the rate equations of (8.11)–(8.13) with injection current modulation well explains their experiments.

8.3 Vertical-Cavity Surface-Emitting Lasers

8.3.1 Vertical-Cavity Surface-Emitting Lasers

Vertical-cavity surface-emitting lasers (VCSELs) are promising devices of light sources for optical information processing and communications. Currently, VCSELs from visible wavelengths to near infrared (1.5 μm) are fabricated and their output powers reach as high as several tens of milliwatts. Also, a device that has a high modulation bandwidth of over 10 GHz with a low RIN of less than −140 dB is fabricated. A VCSEL has a disk structure with light coming out from the top or bottom of the substrate surface. Various types of device structures have been proposed. Index- and gain-guiding structures are used for the confinements of carrier and light in VCSELs such as those for edge-emitting semiconductor lasers. Each guiding structure has merits and demerits in the laser oscillations, but the differences of the stable and unstable effects between those device structures are usually small compared with those in edge-emitting semiconductor lasers, since the length of the laser cavity is much smaller than that of edge-emitting semiconductor lasers. The details of VCSEL structures can be found in the book by Li and Iga (2002). Here, we do not discuss the details of device structures and device characteristics, but discuss the dynamics. As an example, the distributed Bragg reflector (DBR) VCSEL is shown in Fig. 8.12. The thickness of the active layer is approximately equal to the wavelength of light λ. The top view of the laser looks like a disk and its diameter is several to tens of μm. For special use, a disk diameter over 100 μm has been fabricated. In these devices, the reflectivity of the bottom surface is almost 100 % and the top reflectivity of the DBR structure is more than 99 %. The laser light comes out from the top. Though the internal reflectivity is very high compared with edge-emitting semiconductor lasers, VCSELs are also sensitive to optical feedback and optical injection. The photon number in the active volume is much less than that of edge-emitting lasers, and a few external photons would cause instabilities in the laser oscillations. VCSELs even for different device structures are described by the same or similar rate equations for the field and the carrier density.

There are many advantages of VCSELs for practical purposes. Since the VCSEL has a symmetric space structure, we can expect a circular beam as its output, while the beam profile of the edge-emitting laser has astigmatism. Due to a short cavity length compatible with the wavelength of light and very high reflectivity of light in the internal cavity, the laser is a very low threshold device, as low as $\sim\mu$A. From this same reason, we can produce a stabilized oscillation with a single mode that has a large mode separation (∼40 THz). Another merit of VCSELs is the easiness of devising laser arrays because of the surface-emitting structure. However, VCSELs

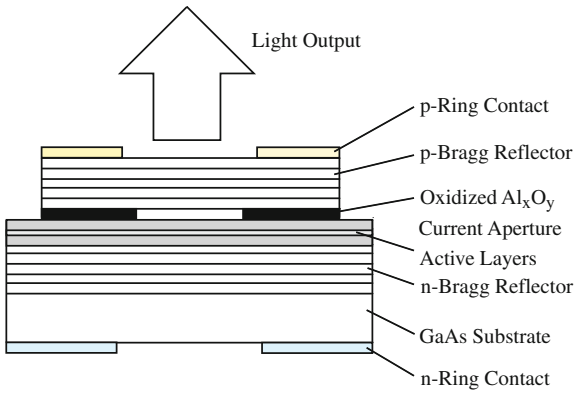

Fig. 8.12 Distributed Bragg reflector VCSEL structure

have unstable features for their operations even without any external perturbations. In addition to the time-dependent phenomena, the space structures and the polarization modes give rise to instability and chaotic dynamics in VCSELs. Spatial hole-burning and multi-transverse mode oscillations are often observed in the laser output to cause instabilities such as spatial-mode and polarization switching. Therefore, the VCSEL itself is an unstable laser. To describe the dynamics of VCSELs, several models have been proposed. Each model has the advantages for explaining respective particular dynamics of real VCSELs. In the following, some of them are introduced.

8.3.2 Spatial-Mode Expansion Model

The rate equations for VCSELs are similar to those for the narrow-stripe edge-emitting laser except for the spatial terms. For a certain polarization mode, the field equation is given as (Valle et al. 1995a,b; Law and Agrawal 1997a,b)

$$\frac{\mathrm{d}E_j(t)}{\mathrm{d}t} = \frac{1}{2}(1 - i\alpha)G_{nj}\{n(r,\ \phi,\ t) - n_{\mathrm{th},j}\}E_j(t) \tag{8.16}$$

where $n(r,\ \phi,\ t)$ is the space-dependent carrier density for the radial coordinates $(r,\ \phi,\ z)$ and $n_{\mathrm{th},j}$ is the threshold carrier density for the jth spatial mode. E_j is the field amplitude for the laser oscillation of the jth spatial component, and the total complex amplitude from a VCSEL is written as

$$\mathbf{E}_{\mathrm{total}}(r,\ \phi,\ z,\ t) = \frac{1}{2}\sum_{j=1}^{M}\hat{\mathbf{e}}_j E_j(t)\psi_j(r,\phi)A_0\sin(\beta_z z)\exp(-i\omega_{\mathrm{th},j}t) + c.c. \tag{8.17}$$

where $M$is the total number of the spatial modes, $\hat{\mathbf{e}}_j$ is the polarization vector for the jth mode, ψ_j is the eigen-function for the jth mode, β_z is the propagation constant

for the z direction, and A_0 is the normalization coefficient. Since the carrier diffusion in the radial direction must be taken into account for the VCSEL oscillation, the rate equation for the carrier density is written as

$$\frac{\mathrm{d}}{\mathrm{d}t}n(r,\ \phi,\ t) = D\nabla_T^2 n(r,\ \phi,\ t) + \frac{J(r,\ \phi)}{ed} - \frac{n(r,\ \phi,\ t)}{\tau_s} - \frac{\Gamma_d}{d}\sum_{j=1}^{M} G_{nj}\{n(r,\ \phi,\ t) - n_0\}|E_j(t)\psi_j(r,\phi)|^2 \tag{8.18}$$

where D is the coefficient for the carrier diffusion, the subscript T denotes the operation for the transverse coordinates, and Γ_d is the confinement factor for the longitudinal direction in the active layer given as

$$\Gamma_d = \int_0^d |A_0 \sin(\beta z)|^2 \mathrm{d}z \tag{8.19}$$

Here, the thickness of the active layer d is smaller than the total length of the laser cavity L, thus $\Gamma_d < 1$. In the derivation of the carrier density Eq. (8.18), we must consider the depletion of carriers for laser emission and take into account the interference terms for the external product of the vector polarizations. However, the frequency difference of the modes is usually of the order of several tens of GHz to one hundred GHz. As a result, the beating of these i and j terms, $\exp\{-i(\omega_l - \omega_j)t\}$, has a high frequency and the carrier cannot follow the oscillation. Therefore, we can neglect this effect and Eq. (8.18) becomes a good approximation for the dynamics of the carrier density.

The eigenfunction for the jth mode ψ_j is a function of the polar coordinate calculated for a particular structure of the VCSEL. For example, for a weak index-guide cylindrical structure with two polarization states corresponding to the spatial LP_{01} mode, it is written by the Bessel function of the first kind $\mathrm{J}_0(z)$ and the modified Bessel function of the second kind $\mathrm{K}_0(z)$ and has the following form:

$$\psi_j(r,\phi) = \begin{cases} \frac{\mathrm{J}_0(u_{1j}r/R_a)}{\mathrm{J}_0(u_{1j})} & \text{for} \quad r \le R_a \\ \frac{\mathrm{K}_0(w_{1j}r/R_a)}{\mathrm{K}_0(w_{1j})} & \text{for} \quad r > R_a \end{cases} \tag{8.20}$$

where R_a is the radius of the active area and u_{1j} and w_{1j} are the first roots of the eigenvalue equation for the jth polarization mode

$$\frac{u_j \mathrm{J}_1(u_j)}{\mathrm{J}_0(u_j)} = \frac{w_j K_1(w_j)}{\mathrm{K}_0(w_j)} \tag{8.21}$$

They have a relation of $u_{1j}^2 + w_{1j}^2 = V_j^2$. V_j is the normalized frequency defined as

$$V_j = \frac{2\pi R_a \sqrt{\eta_{1j}^2 - \eta_j^2}}{\lambda} \tag{8.22}$$

where λ is the wavelength of light in vacuum and η_{1j} and η_j are the refractive indices for the jth mode in the active area and the clad region.

8.3.3 Spin-Flip Model

The spatial mode model well represents the spatial behaviors of VCSELs, however, it takes a long time to perform numerical calculations. Alternative models to show the dynamics of VCSELs have been proposed. The spin-flip model is an excellent one for analyzing the behaviors of polarization switching and polarization-mode oscillation in the lowest spatial mode. In the derivation of the rate equations in the previous subsection, we consider the polarization effects in VCSELs in (8.17). However, in the physical terms, we must take into account the effects of electron spin states associated with light emission in the polarization dynamics of VCSELs. Specifically, left and right circularly polarizations of laser light emission are related to spin states of electrons in the conduction and valence bands. This is the origin of the polarization oscillations in VCSELs, and results in a rich variety of polarization dynamics including polarization switching frequently observed in VCSELs. San Miguel et al. proposed a spin-flip model for the rate equations of VCSELs by taking into account spin dynamics (San Miguel et al. 1995; Martín-Regalado et al. 1997; Sciamanna et al. 2002a,b). The model couples the polarization state of the electric field to the semiconductor medium by including the magnetic sublevels of the conduction and valence bands (the angular momentum numbers of electron) in quantum well devices. It is shown that laser dynamics depend significantly on the value of the relaxation rate. The polarization switching is included by the assumption of the population difference between the carrier densities with positive- and negative-spin values. From these equations, the dynamics of the laser oscillations for the lower order spatial mode can be easily explained, and the results are entirely coincident with the model discussed in the previous subsection. Although the dynamics of polarization dynamics in VCSELs can be well-defined by the model, these rate equations are usually applicable to the lowest spatial mode oscillation. In the following, we derive the expressions for the rate equations based on the spin dynamics.

In VCSELs, the thickness of the laser cavity is thin and less than the optical wavelength and light comes out vertically from the substrate surface (along the z-direction), so that the degeneration of spin states of electrons in heavy-hole and light-hole bands is resolved along the z-direction and we must take into account the difference between down- and up-spin states. In the case of edge-emitting semiconductor laser, the thickness of the active layer is also very thin, however, light comes out perpendicular to the z-direction and we need not consider the spin states. Only the total carrier number is important for the dynamics in edge-emitting semiconductor

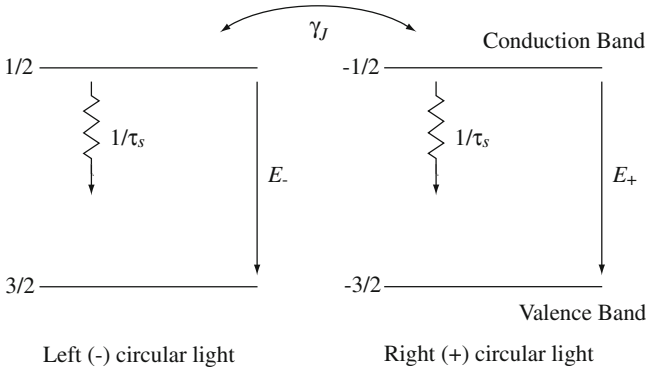

Fig. 8.13 Four-level spin-flip model for polarization dynamics in quantum-well VCSEL

laser, while the sum and difference of carrier number play the important role in the VCSEL dynamics. Figure 8.13 shows the four-level model for polarization dynamics in quantum-well VCSELs (San Miguel et al. 1995; Martín-Regalado et al. 1997). In Fig. 8.13, γ_J^{-1} is the spin relaxation time. In the spin dynamics model of laser transitions, the magnetic quantum numbers in the lower edge of the conduction band have $J_z = \pm 1/2$ in accordance with down- and up-spin states. On the other hand, the magnetic quantum numbers for heavy holes in the upper valence band have values of $J_z = \pm 3/2$, since we can neglect the effect of light holes in quantum-well VCSELs. In the quantum state numbers, the same sign corresponds to the same spin state. Photon emitted from $+$ spin state corresponds to left circular polarization, while photon from $-$ spin state to right circular polarization. In the model, the decay rate γ_J accounts for the mixing of the populations with opposite value of J_z. This parameter is introduced to model spin-flip relaxation processes.

We next consider the effects of cavity anisotropies, which can be modeled in the two equations for the time evolution of the field amplitudes with two circular polarizations by replacing the linear loss rate with a matrix whose Hermitian part is associated with amplitude losses and whose anti-Hermitian part gives linear and circular phase anisotropies (also known as birefringence and circular dichroism, respectively). For VCSELs, it is known that there are two preferred modes of linear polarization that coincide with the crystal axes. These two modes have a frequency splitting associated with the birefringence of the medium. This can be modeled by a linear phase anisotropy given by a parameter γ_p, which represents the effect of different indexes of refraction for the orthogonal linearly polarized modes. In addition, the two modes may have a slightly different gain-to-loss ratio that can be related to the anisotropic gain properties of the crystal; the slightly different position of the frequencies of the modes with respect to the gain versus frequency curve, and different cavity geometries for the differently polarized modes. These effects can be modeled by an amplitude anisotropy with parameter γ_a. We assume here for

simplicity that the directions of linear phase and amplitude anisotropy coincide, so that both are diagonalized by the same basis states.

We now derive the rate equations for double crossed linearly polarized light. Electron spin is associated with photon spin. We start the description of circularly polarized light for the fields of photons in such a case. The laser light field is coupled to two population inversion variables; n is the sum of the upper state and lower state populations and n_J is the number of the difference between the population inversions (upper and lower state population difference) on the two distinct channels with positive or negative value of J_z (quantum spin number). Namely, in semiconductor lasers, n represents the total carrier number in excess of its value at transparency. Then the rate equations for the fields with right (+) and left (−) circularly polarized states are given as (San Miguel et al. 1995)

$$\frac{\mathrm{d}E_{\pm}(t)}{\mathrm{d}t} = \frac{1}{2}(1 - i\alpha)G_n \left\{ n_{\pm}(t) - \frac{1}{G_n \tau_{ph}} \right\} E_{\pm}(t) - (\gamma_a - i\gamma_p)E_{\mp}(t) \quad (8.23)$$

where $n_{\pm}(t) = n(t) \pm n_J(t) - n_0$($n_0$ is the total carrier density at transparency), and γ_a and γ_p are the linear anisotropies representing dichroism and birefringence discussed above. Note that signs between the spin states and the subscripts of the fields are opposite. The rate equations for the carrier density with spin-down and spin-up, $n_{\pm}$, are written as

$$\frac{\mathrm{d}n_{\pm}(t)}{\mathrm{d}t} = \frac{J}{ed} - \frac{1}{2\tau_s}\{n_+(t) + n_-(t)\} \mp \frac{1}{2\tau_J}\{n_+(t) - n_-(t)\} - 2G_n n_{\pm}(t)|E_{\pm}(t)|^2 \quad (8.24)$$

where $1/\tau_J$ is the spin-flip rate.

Using the conversion relations between linearly polarized lights and circularly polarized lights, $E_x = (E_+ + E_-)/\sqrt{2}$ and $E_y = i(E_+ - E_-)/\sqrt{2}$, and also the relations of the sum of the carrier number of down- and up-spin states n and the spin-state difference n_J, $n_+ = n + n_J - n_0$ and $n_- = n - n_J - n_0$, the equations for the linearly polarized fields are given as

$$\frac{\mathrm{d}E_x(t)}{\mathrm{d}t} = \frac{1}{2}(1-i\alpha)G_n[\{n(t)-n_{\mathrm{th}}\}E_x(t)-in_J(t)E_y(t)]-(\gamma_a-i\gamma_p)E_x(t) \quad (8.25)$$

$$\frac{\mathrm{d}E_y(t)}{\mathrm{d}t} = \frac{1}{2}(1-i\alpha)G_n[\{n(t)-n_{\mathrm{th}}\}E_y(t)+in_J(t)E_x(t)]+(\gamma_a-i\gamma_p)E_y(t) \quad (8.26)$$

The rate γ_p reads to a frequency difference of $2\gamma_p$ between the x- and y-polarized solutions (the x-polarized solution having the lower frequency when γ_p is positive). The decay rate γ_a reads to threshold difference for these two linearly polarized solutions, with the y-polarized solution having the lower threshold when γ_a is positive. In actual fact, the frequency difference between the two linear modes depends on both the parameters γ_p and γ_a. Similarly, the equations for the total carrier density and the difference of the spin states are calculated as

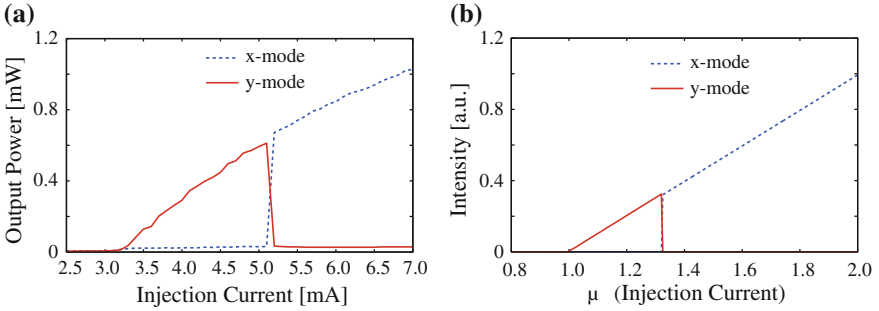

Fig. 8.14 L-I characteristics of VCSELs. **a** Experimental L-I characteristic and **b** L-I characteristic calculated by the spin-flip model

$$\frac{dn(t)}{dt} = \frac{J}{ed} - \frac{n(t) - n_0}{\tau_s} - G_n\{n(t) - n_0\}\{|E_x(t)|^2 + |E_y(t)|^2\} + iG_n n_J(t)\{(E_y(t)E_x^*(t) - E_x(t)E_y^*(t)\} \tag{8.27}$$

$$\frac{dn_J(t)}{dt} = -\frac{n(t)}{\tau_J} - G_n n_J(t)\{|E_x(t)|^2 + |E_y(t)|^2\} + iG_n\{n(t) - n_0\}\{(E_y(t)E_x^*(t) - E_x(t)E_y^*(t)\} \tag{8.28}$$

The total carrier number n has a decay rate $1/\tau_s$ associated with spontaneous decay, while the carrier differnce n_J has a decay rate $1/\tau_J = 1/\tau_s + 2\gamma_J$. The rate γ_J accounts for the mixing of the populations with opposite value of J_z, which was introduced to model spin-flip relaxation processed and assumed to have the same value for the conduction and valence bands.

One of the typical features of VCSELs is a sharp polarization switching for the increase or decrease of the bias injection current. Figure 8.14 shows an example of polarization switching in VCSELs. Figure 8.14a, b are an experimentally observed LI characteristic and a simulation result calculated from (8.25)–(8.28) using the parameter values of $\gamma_p = 1.0\,\text{ns}^{-1}$ and $\gamma_a = 45\,\text{ns}^{-1}$. In this case, the y-polarization mode is the starting main mode above the threshold and it switches to the x-polarization mode for the increase of the bias injection current. Though the switching point does not correspond with each other, a sharp polarization switching is well reproduced by the numerical simulation. It is noted that the frequency difference of the laser oscillations between y- and x-polarization modes is about $+6\,\text{GHz}$ at a bias injection current of 4 mA, although the lasing power of the x-polarization mode is very small at this bias injection current.

Normalized versions of the above rate equations are widely used for numerical investigations of VCSEL dynamics (Martín-Regalado et al. 1997). Using the normalizations of the variables as $E_\pm{}' = \sqrt{\tau_s G_n} E_\pm$ and $n_\pm{}' = n' \pm n_J{}' = G_n \tau_{\text{ph}} n_\pm$ ($n' = G_n \tau_{\text{ph}}(n - n_0)$ and $n_J{}' = G_n \tau_{\text{ph}} n_J$), the field and carrier density equations

for circularly polarized states read as

$$\frac{\mathrm{d}E_{\pm}'(t)}{\mathrm{d}t} = \frac{1}{2\tau_{\mathrm{ph}}}(1 - i\alpha)\{n_{\pm}(t) - 1\}E_{\pm}'(t) - (\gamma_a - i\gamma_p)E_{\mp}'(t) \tag{8.29}$$

$$\frac{\mathrm{d}n_{\pm}'(t)}{\mathrm{d}t} = \frac{1}{\tau_s}\mu - \frac{1}{2\tau_s}\{n_{+}'(t) + n_{-}'(t)\} \mp \frac{1}{2\tau_J}\{n_{+}'(t) - n_{-}'(t)\} - \frac{2}{\tau_s}n_{\pm}'(t)|E_{\pm}'(t)|^2 \tag{8.30}$$

where μ is the current density normalized to the threshold, $\mu = J/J_{\mathrm{th}}$. On the other hand, for linearly polarized case, the field equations of the two components are written as

$$\frac{\mathrm{d}E_x'(t)}{\mathrm{d}t} = \frac{1}{2\tau_{\mathrm{ph}}}(1 - i\alpha)[\{n'(t) - 1\}E_x'(t) - in_J'(t)E_y'(t)] - (\gamma_a - i\gamma_p)E_x'(t) \tag{8.31}$$

$$\frac{\mathrm{d}E_y'(t)}{\mathrm{d}t} = \frac{1}{2\tau_{\mathrm{ph}}}(1 - i\alpha)[\{n'(t) - 1\}E_y'(t) + in_J'(t)E_x'(t)] + (\gamma_a - i\gamma_p)E_y'(t) \tag{8.32}$$

The equations for the total carrier density and the carrier difference are given as

$$\begin{aligned}\frac{\mathrm{d}n'(t)}{\mathrm{d}t} = &-\frac{1}{\tau_s}[n'(t)\{1 + (|E_x'(t)|^2 + |E_y'(t)|^2)\} - \mu \\ &- in_J'(t)\{E_y'(t)E_x'^{*}(t) - E_x'(t)E_y'^{*}(t)\}]\end{aligned} \tag{8.33}$$

$$\begin{aligned}\frac{\mathrm{d}n_J'(t)}{\mathrm{d}t} = &-\frac{1}{\tau_J}n_J'(t) - \frac{1}{\tau_s}[n_J'(t)\{|E_x'(t)|^2 + |E_y'(t)|^2\} \\ &- in'(t)\{E_y'(t)E_x'^{*}(t) - E_x'(t)E_y'^{*}(t)\}]\end{aligned} \tag{8.34}$$

Several spin relaxation processes for electrons and holes have been identified in semiconductors, such as scattering by defects, exchange interactions between electrons and holes, and exciton–exciton exchange interactions (Martín-Regalado et al. 1997). From experimental measurements of spin relaxation times in quantum wells, the relaxation time is of the order of tens of picoseconds. Since typically $\tau_s \sim 1\,\mathrm{ns}$, and $\tau_{\mathrm{ph}} \sim 1\,\mathrm{ps}$, the spin mixing τ_J occurs on an intermediate timescale between that of the field decay and that of the total carrier population difference decay. Hence, the dynamics of the difference in spin states n_J cannot be adiabatically eliminated for the timescales of interest. The rate equations including the magnetic sublevels of the conduction and valence bands are applied to analyses for the dynamics of VCSEL polarizations such as polarization switching and polarization instabilities (Sciamanna et al. 2003b,c; Sciamanna and Panajotov 2005, 2006; Masoller et al. 2006). In particular, fruitful results are obtained for explanations of the dynamics for orthogonal optical injection and stabilization in VCSELs. For the treatments of dynamics related to higher spatial modes, we need the rate equations discussed in

the previous subsection. The spin-flip model is essentially developed for explaining the polarization dynamics in VCSELs in the fundamental spatial mode. However, it can be extended to the model including higher spatial modes (Valle et al. 2007). In this book, we use mainly the theoretical treatments in the previous subsection, which includes the spatial effects. However, the model of the magnetic sublevels is also used for VCSEL dynamics when necessary.

8.3.4 Two-Gain Model

The rate equations for narrow-stripe edge-emitting semiconductor lasers have been modified and used to study the dynamics of VCSELs, since they are very simple and easier to perform steady-state analyses and numerical simulations (Danckaerta et al. 2002; Hong et al. 2005). In the rate equations, the complex fields E_x and E_y for the two polarization directions in the orthogonal x and y coordinates at a single spatial mode oscillation are given as

$$\frac{\mathrm{d}E_x(t)}{\mathrm{d}t} = \frac{1}{2}(1 - i\alpha)G_{n,x}\{n(t) - n_{\mathrm{th},x}\}E_x(t) \tag{8.35}$$

$$\frac{\mathrm{d}E_y(t)}{\mathrm{d}t} = \frac{1}{2}(1 - i\alpha)G_{n,y}\{n(t) - n_{\mathrm{th},y}\}E_y(t) \tag{8.36}$$

where $G_{n,x}$ and $G_{n,y}$ are the gain coefficients for the polarization modes, and $n_{\mathrm{th},x}$ and $n_{\mathrm{th},y}$ are the carrier densities at threshold. We here introduced the different gain coefficients for the orthogonal polarization modes. The carrier density equation is given as

$$\frac{\mathrm{d}n(t)}{\mathrm{d}t} = \frac{J}{ed} - \frac{n(t)}{\tau_s} - G_{n,x}\{n(t) - n_{0,x}\}|E_x(t)|^2 - G_{n,y}\{n(t) - n_{0,y}\}|E_y(t)|^2 \tag{8.37}$$

where $n_{0,x}$ and $n_{0,y}$ are the carrier densities at transparency for the respective modes.

For the main lasing mode above the threshold, the gain is saturated, however, the gain of the counterpart polarization mode is a function of the bias injection current. At a certain bias injection current, the oscillation mode is switched from the main polarization mode to the sub-polarization mode. Then, the gain of the sub-mode saturates and the gain of the original main mode decreases for the further increase of the bias injection current. Figure 8.15 is an example of two orthogonal gain coefficients calculated from the spatial model, which is discussed in Sect. 8.3.2. In this case, the y-polarization mode is the main oscillation mode above the threshold. At a bias injection current $\mu = 2.04$, the laser oscillation is switched to the x-polarization mode. During the oscillation mode, the corresponding gain is clamped to a constant value, while the counterpart mode linearly increases or decreases for the change of the bias injection current. Therefore, from the gain coefficients in Fig. 8.15,

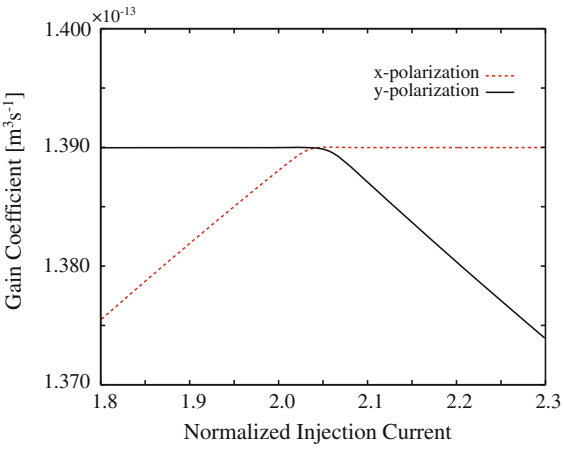

Fig. 8.15 Example of gain coefficients for two orthogonal polarization modes for increase of bias injection current calculated from the spatial mode model discussed in Sect. 8.3.2. μ is the normalized bias injection current to the threshold as $\mu = J/J_{\text{th}}$. The polarization switching point is set to $\mu = 2.04$

we introduce the difference of the gain coefficients $G_{n,x}$ and $G_{n,y}$ as

$$G_{n,y} - G_{n,x} = G_0 \left(1 - \frac{J}{J_{\text{sw}}}\right) \tag{8.38}$$

where G_0 is a certain constant and J_{sw} is the switching current at which the polarization alteration occurs. We here assume that the y-polarization mode is the original laser oscillation mode above the threshold and x-polarization mode is the sub-mode. Also, the gains below or above the polarization switching current are defined as

$$G_{n,y} = G_{0y} = \text{constant for } J \leq J_{\text{sw}} \tag{8.39a}$$

$$G_{n,x} = G_{0x} = \text{constant for } J > J_{\text{sw}} \tag{8.39b}$$

For the example of the spatial mode model in Fig. 8.15, we obtain the gain constants as $G_0 = 2.00 \times 10^{-15}\ \text{m}^3\ s^{-1}$ and $G_{0y} = G_{0x} = 1.39 \times 10^{-13}\ \text{m}^3\ s^{-1}$. Using the two-gain model, we can describe a sharp polarization switching such as observed in Fig. 8.14. In the spatial mode model in Sect. 8.3.2, the difference between the gain coefficients of the two polarization modes is implicitly included through the refractive indices in the orthogonal gains defined in (8.18), so that we do not explicitly introduce the terms for the gain difference in the rate equations. While the difference is explicitly included as the parameters of birefringence and dichroism, γ_p and γ_a, in the spin-flip model in Sect. 8.3.3.

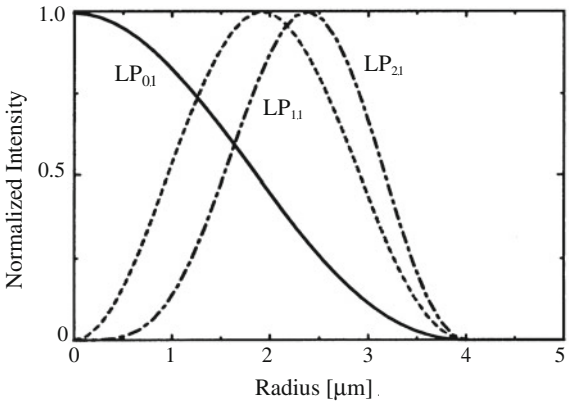

Fig. 8.16 Spatial mode distributions for LP_{01}, LP_{11}, and LP_{21} modes in VCSELs. The radius of the disk is assumed as 4 μm

8.3.5 Characteristics of VCSELs in Solitary Oscillations

Even in the absence of external perturbations, VCSELs sometimes show unstable behaviors depending on the bias injection current. Spatial and polarization modes play important roles in the dynamic behavior of VCSELs. Higher spatial modes are easily excited for a higher bias injection current. Figure 8.16 shows the beam profiles for the lowest three spatial modes along the radial direction of a VCSEL (Linearly Polarized modes; LP_{01}, LP_{11}, and LP_{21} modes). These modes are calculated from (8.20)–(8.22). Due to the spatial hole-burning effects, the carrier distribution has a dip at the center of the disk in a VCSEL and the higher spatial modes tend to oscillate for a large bias injection current (Law and Agrawal 1997b). Figure 8.17 shows the experimentally obtained near-field images of the oscillation modes (Degen et al. 1999). The disk diameter of the VCSEL is 6 μm. The patterns are obtained by changing the bias injection current. Higher spatial modes are excited for the increase of the bias injection current. The excitation of higher modes strongly depends on the disk diameter. For ordinary applications of VCSELs, a circular Gaussian beam of the lowest mode is desirable. To obtain such a clean beam, the diameter of a VCSEL must be small, but it is difficult to attain a high power operation at the same time.

In semiconductor materials, there exists the difference of the refractive indices between the components for the principal axis and the orthogonal axis to it because of the distortion and birefringence of the materials. The difference between the indices is very small and it is 10^{-3}–10^{-4}. For ordinary edge-emitting semiconductor lasers, the difference can be ignored due to a large asymmetric configuration for the TE and TM modes in the active layer and the laser usually operates at only TE mode. However, the difference plays a crucial role for the operations of VCSEL, since it has a circular disk structure of the light-emitting facet. Then, there is an ambiguity for the polarization direction of the laser oscillation. A VCSEL usually oscillates at a polarization mode along the optic axis of the material (y-polarization mode) when

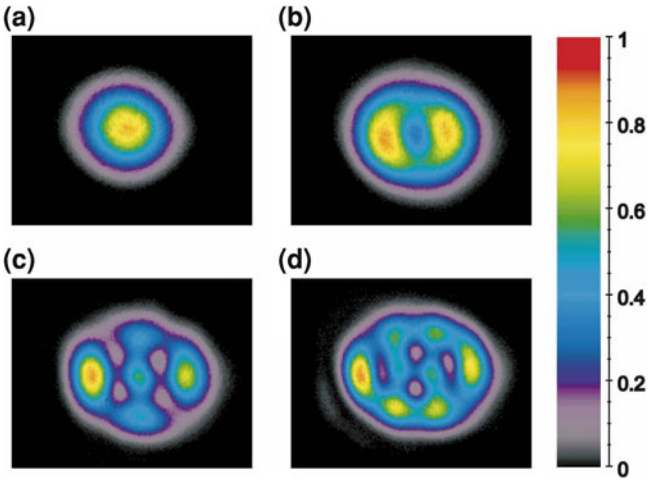

Fig. 8.17 Experimentally obtained near-field images of VCSEL with 6 μm diameter at an injection current of **a** 3.0, **b** 6.2, **c** 14.7, and **d** 18 mA [after Degen et al. (1999); © 1999 OSA]

the laser is biased at a low injection current. However, the polarization mode may switch from this mode to the orthogonal one (x-polarization mode) for the increase of the bias injection current. This switching is mainly induced by the distortion or the birefringence of the laser material as discussed above. Taking into consideration the birefringence of laser materials, the polarization switching is well reproduced by the numerical simulations from (8.16)–(8.18) (Giudici et al. 1999; Danckaerta et al. 2002). At a low bias injection current, the carrier density has a maximum value at the center of the disk in the active area and the carrier density smoothly decreases toward the edge of the disk. However, for a large bias injection current, hole-burning of carriers occurs at the center of the disk. Then, the carrier density takes the maximum value a little away from the center of the disk. This induces the excitation of the orthogonal mode and the suppression of the original mode, since, for example, the hole-burning due to the birefringence causes the transfer of the optical energy from the y-mode to the x-mode. Then, the laser oscillation is switched from the y-mode to the x-mode. The effects are distinct for VCSELs with large birefringence and small disk size.

The L-I characteristic of a VCSEL experimentally obtained for a disk diameter of 3 μm is already shown in Fig. 8.14. The laser is a typical single spatial mode VCSEL of a wavelength of 780 nm and a maximum power of 2.0 mW, since the diameter is rather small compared with spatially multimode VCSELs such as shown in Fig. 8.17. In Fig. 8.14a, the laser at first oscillated at the main polarization mode (y-polarization mode) above the threshold current of 3.1 mA, but it switched to the orthogonal polarization mode (x-polarization mode) at the bias injection current of 5.2 mA. After the switching, the laser stably oscillated at the orthogonal polarization mode. Usually, the polarization switching has a hysteresis for the increase or the decrease in the bias

injection current. Whether we can observe clear switching of the polarization modes or not, strongly depends on the characteristics of the laser materials and the device structures. Some VSCELs do not show clear polarization switching for the change of the bias injection current. Different from edge-emitting semiconductor lasers, two orthogonal polarization modes are easily excited simultaneously owing to a small gain difference between the two modes. The laser is longitudinally a single mode, since the total cavity length in VCSELs is as small as around 1 μm and the free spectral range of the cavity is very large. For the same reason, the conversion efficiency from the current to the frequency is very large compared with that of edge-emitting semiconductor lasers (see Sect. 5.1.6). Indeed, the laser in Fig. 8.14a has a conversion efficiency of 128 GHz/mA. Due to a short cavity length compared with edge-emitting semiconductor lasers (usually, the cavity length is several hundred times less than that of an edge-emitting semiconductor laser), the change of the refractive index for the increase or decrease of the bias injection current causes a very large frequency change in the laser oscillation through the relation of $\Delta\nu \approx c(1 - \Delta\eta/\eta)/2\eta l$, where $\Delta\nu$ and $\Delta\eta$ are the frequency change and the change of the refractive index, respectively.

Even in solitary oscillations, VCSELs show dynamic characteristics. One such type of dynamics is the anti-phase irregular oscillation of the optical power between the two polarization modes (Fujiwara and Ohtsubo 2004). Figure 8.18 shows an experimental example of anti-phase oscillations of the y- and x-polarization modes in a VCSEL. Unstable pulsations and bistability are sometimes observed at the switching point of the two polarization modes (Tang et al. 1997). However, not only at the switching point of the two polarization modes but also at certain bias injection currents different from the switching point, does the laser show fast unstable oscillations and the two polarization modes oscillate at anti-phase manner in time. When the output power of the y-polarization mode goes down, the output power of the x-polarization mode grows up, and vice versa. This anti-phase oscillation is frequently observed in chaotic VCSELs subjected to optical feedback and injection current modulation (Besnard et al. 1997, 1999).

8.3.6 Spatio-Temporal Dynamics in VCSELs

Lasers with spatial structures such as VCSELs and broad-area lasers have spatio-temporal dynamics induced by diffraction of light and hole-burning of carriers in the laser cavity. In the case of VCSELs, the cavity length is short, so that the effect of the diffraction of light inside the cavity can be neglected. However, the effect of carrier hole-burning plays a crucial role for transverse-mode oscillations. The polarization dynamics of VCSEL are strongly related to carrier hole-burning, and the laser shows picosecond instabilities even at solitary oscillations. Time averaged polarization dynamics in VCSELs, such as dynamics of near-field patterns for the bias injection current, were extensively studied, while a few studies of spatio-temporal dynamics were reported (Mulet and Balle 2002; Barchanski et al. 2003;

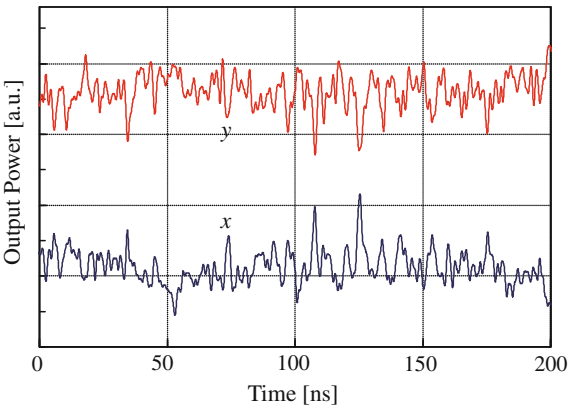

Fig. 8.18 Example of anti-phase oscillations of y- and x-polarization modes in VCSEL at solitary oscillation

Valle et al. 2007). In this subsection, we present some experimental results for the spatio-temporally resolved polarization dynamics and discuss the underlining mechanism. Figure 8.19 shows the experimental results of spatiotemporal dynamics of a VCSEL obtained by a temporally resolved imaging by differential analysis, which allows us to extract the full two-dimensional evolution of the near-field intensity on timescales of 10 ps (Barchanski et al. 2003). The laser used is an oxidized VCSEL with an oscillation wavelength of 852 nm and a maximum output power of 3.8 mW. The VCSEL has a disc diameter of 14 μm.

Figure 8.19a shows the laser outputs of the two polarization modes for the time evolution after a step impulse, in which each polarization mode shows relaxation oscillation after the switch-on. A period of 10 μs of the pulse prevents the occurrence of thermal effects in the experiments. The laser is biased at $2.3J_{\mathrm{th}}$. At this bias injection current, the frequency of the relaxation oscillation is about 3 GHz. In this figure, the 90° polarization mode is the main oscillation mode. After about 3 ns from switch-on, the laser settles down to steady-state oscillation. Figure 8.19b shows snapshots for the evolution of the near-field intensity in the VCSEL after the second relaxation oscillation peak. In order to allow measurements, a displacement prism was used in the detection path to separate the laser beam into two orthogonal polarization patterns. The near-field polarized patterns of the laser was detected as an integrated image of 36,000 events by a CCD camera with a fast shutter time ∼200 ps using gating triggers synchronized with the driving pulses for the bias injection current. The images in Fig. 8.19b give evidence for a rich dynamical behavior in the emission profile in both polarization directions. In the 0° polarization mode, the intensity change of the center of the disc aperture is clearly seen, namely, the center is filled with a bright spot at 1,720 ps, however, the center of the aperture remains mostly dark at 10 ps later. The intensity at 1,740 ps is nearly uniform over the whole aperture, and then the center is again dark at 1,750 ps. In the near-field patterns of the 90° polarization mode, we can see clear rotational flicker of the bright spots of the laser oscillations. For example, bright spots of the intensity rotate by 5° counterclockwise from 1,720 to 1,730 ps, while they rotate by 5° clockwise from 1,740 to 1,750 ps. This

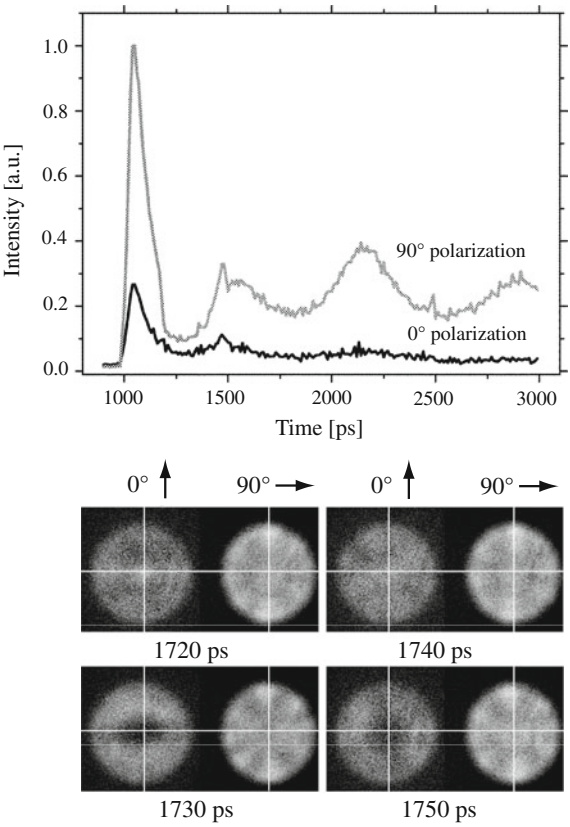

Fig. 8.19 **a** Evolution of the relaxation oscillations extracted from the differential images of the near-field polarization-resolved patterns. *Gray curve* 90 ° polarization mode (dominant oscillation mode), and *black curve* 0 ° polarization mode. **b** Snapshots for the evolution of near-field intensity of the VCSEL after the second relaxation oscillation peak. In each snapshot, the left shows the 0 ° polarization mode and the right 90 ° polarization mode. The crossing point of the overlaid crosshair is the center of the laser [after Barchanski et al. (2003) © 2003 IEEE]

kind of rotational flicker is attributed to the spatial hole burning of the carrier density in the laser cavity. Spatial hole-burning has been identified as a very important effect contributing to the observed dynamics on the examined timescales, especially for lasers having a spatial structure. Similar nonlinear dynamical behaviors have already been found and well investigated in the field of broad-area semiconductor lasers as known filamentation effects, which will be discussed in the following section.

Every transverse mode in a VCSEL corresponds to a different wavelength. Therefore, by spectrally resolving the near-field emission intensity, it is possible to investigate the dynamics of each mode separately. Figure 8.20 shows spectrally resolved near-field patterns of the VCSELs. In the observations, a spectrometer was used in the detection path to obtain spectrally resolved near-field patterns of the laser oscillations. The horizontal axis represents the spatial coordinate, the vertical axis is a combination of both spatial and spectral coordinates, with the wavelength increasing from the bottom to top of each snapshot. The large birefringence splitting, which is the spectral spacing among the fundamental Gaussian modes in orthogonal polarization directions, is quite noticeable. The estimation of the birefringence splitting,

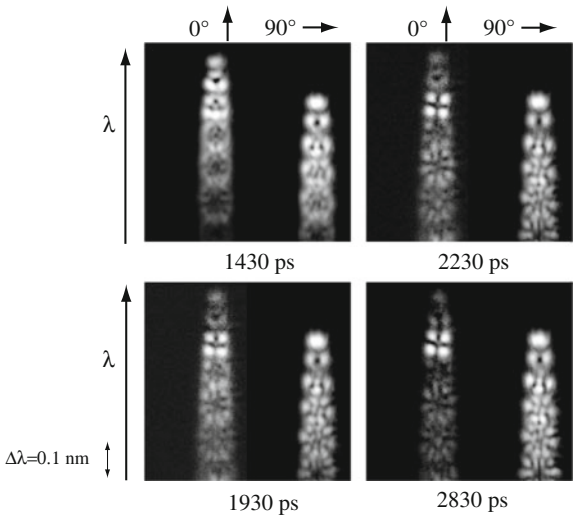

Fig. 8.20 Spectrally resolved near-field patterns for time evolution. In each snapshot, the *left* shows the 0 ° polarization mode and the *right* 90 ° polarization mode. The wavelength increases from *bottom* to *top* of each snapshot. The snapshots show the intensity change during 100 ps [after Barchanski et al. (2003); © 2003 IEEE]

performed with an optical spectrum analyzer having a maximal resolution of 0.05 nm, provides a value of approximately 0.11 nm, or 50 GHz, respectively. The first image at 1,430 ps, within the second relaxation oscillation peak, shows two more mode orders than during the first relaxation oscillation peak, though the near-field pattern at the first relaxation oscillation peak is not shown here. At 1,930 ps, about ten modes occur in the near-field intensity within the observed area. While the relative intensity among the 90° polarization modes mostly remains uniform, there is a drastic change in the modal behavior in the 0° polarization mode. Throughout the evolution, the four-lobed mode, which is the second oscillation mode, remains as an oscillation mode and all other modes of the 0° polarization direction show a relative smaller intensity. The fundamental Gaussian mode in the 90° polarization mode is spectrally aligned at the same position as the bright four-lobed mode in the 0° polarization mode. This spectral alignment implies the importance of spectral interactions related to the spatial carrier hole-burning effects. Namely, the fundamental mode, observed in the 90° polarization direction, has its intensity concentrated in the center of the aperture. In contrast, the intensity of the four-lobed mode is concentrated in the periphery of the aperture, resulting in a minimal spatial overlap of both modes. The complementary oscillation between the two polarization modes originates from a competition of both polarization directions for the available gain in the active medium. The dynamics of VCSELs even at solitary oscillation still remains an interesting research field, providing further insight into the fundamental physics of semiconductor lasers and promising device optimization.

Table 8.3 Characteristic device parameters for a VCSEL at an oscillation wavelength of 850 nm

Symbol	Parameter	Value
G_n	gain coefficient	$2.90 \times 10^{-12}\ \mathrm{m^3 s^{-1}}$
Γ_d	confinement factor	0.1
α	linewidth enhancement factor	3.80
r_1	output facet reflectivity	0.9975
r_2	bottom reflectivity	0.9995
n_{th}	carrier density at threshold	$3.80 \times 10^{24}\ \mathrm{m^{-3}}$
n_0	carrier density at transparency	$1.75 \times 10^{24}\ \mathrm{m^{-3}}$
τ_s	lifetime of carrier	1.00 ns
τ_{ph}	lifetime of photon	3.30 ps
γ_J^{-1}	lifetime of spin	30 ps
τ_{in}	round trip time in laser cavity	22.6 fs
D	diffusion constant	$30\ \mathrm{cm^2\ s^{-1}}$
l	cavity length	1.00 μm
d	active layer thickness	0.20 μm
R_a	radius of active layer	4.00 μm

8.3.7 Optical Feedback Effects in VCSELs

VCSELs have a high reflective mirror of the Bragg reflector within the cavity as much as the internal reflectivity of higher than 99 % to realize a low laser threshold. However, the total photon number within the cavity is much smaller than that of the edge-emitting semiconductor laser and the laser is also affected by a small number of photons from an external reflector. For a small optical feedback, (8.16) is modified and the rate equations for the complex field are written as

$$\frac{\mathrm{d}E_j(t)}{\mathrm{d}t} = \frac{1}{2}(1-i\alpha)G_{nj}\{n(r,\ \phi,\ t)-n_{\mathrm{th},j}\}E_j(t)+\frac{\kappa}{\tau_{in}}E_j(t-\tau)\exp(i\omega_0\tau) \quad (8.40)$$

The other equations for the total complex field amplitude and the carrier density remain unchanged. Equation (8.40) looks like the same form as that for narrow-stripe edge-emitting semiconductor lasers. However, the rate equations of the total field and the carrier density are the functions not only of time but also space and, as a result, the laser shows complicated behaviors compared with narrow-stripe edge-emitting semiconductor lasers. Mutual interactions between the two polarization modes also affect the dynamics. Spatial mode competitions may also play an important role for the dynamics under a large bias injection current. Therefore, we must take into account the essential terms of the spatial polarization modes for numerical calculations of the dynamics.

Since the laser cavity length of a VCSEL is less than the optical wavelength and much smaller than those of other semiconductor lasers, the separations both for the longitudinal and transverse modes are much larger than for other lasers. Therefore,

we can well apply the approximation for a single longitudinal mode operation as far as the laser has a small disk size or is biased at a modest injection current. However, the competition among spatial and polarization modes arises at a higher bias injection current. In the following, we show some characteristics of optical feedback effects in VCSELs. Unstable oscillations of VCSELs induced by optical feedback have been numerically calculated (Law and Agrawal 1998). Table 8.3 is a typical set of parameters used in the numerical simulations. Figure 8.21 shows a numerically calculated time series of the laser output for the change of the external feedback ratio. The diameter of the laser disk is 4 μm and the laser is oscillated with the lowest single mode or the lowest two spatial modes (LP_{01} and LP_{11} modes). However, a single polarization mode is assumed at solitary oscillation. From Fig. 8.21a–d, the two modes show period-doubling like evolutions to chaotic states. However, once they become a fixed oscillation in Fig. 8.21e and again evolve into fully chaotic oscillations in Fig. 8.21f. Spontaneous emission of light is ignored in these calculations, however, it strongly affects the dynamics when the laser oscillates at chaotic states. Some such effects are the increase of noise floor and the broadening of the chaotic carrier frequency.

As dynamics of narrow-stripe edge-emitting semiconductor lasers, low-frequency fluctuations (LFFs) have been observed. LFFs are not only the typical features of narrow-stripe edge-emitting semiconductor lasers, but also they are observed in various types of semiconductor lasers. Fujiwara et al. (2003) have experimentally observed LFFs in VCSELs with optical feedback from a distant reflector. Similar LFF characteristics to those of narrow-stripe edge-emitting semiconductor lasers, sudden power dropout and gradual power recovery, are observed for the y-polarization mode with the lowest spatial mode of LP_{01} at a low bias injection current. Under an LFF oscillation for the y-polarization mode, the output power of the orthogonal x-polarization mode also shows synchronous waveforms of LFFs with the y-polarization mode, but it is an anti-phase oscillation. Similar to the dynamics of narrow-stripe edge-emitting semiconductor lasers, coexistent states of LFFs and stable oscillations are sometimes observed close to the threshold current. The polarization switching is suppressed or even eliminated by parallel optical injection at higher optical feedback ratio, while the laser shows chaotic oscillations at a single polarization mode when the feedback is not so strong (Hong et al. 2004; Aoyama 2011). Also, the coherence of the laser is fairly collapsed at LFF states. However, the laser still holds a single longitudinal-mode operation, because of the large separation of the cavity modes (Von Lehmen et al. 1991). The dynamic properties of LFFs in VCSELs have been demonstrated by numerical simulations using the model of the population difference between the carrier densities with positive and negative spin values, i.e., spin-flip model (Masoller and Abraham 1999a; Sciamanna et al. 2003a,b,c).

Figure 8.22 shows time-averaged effects of polarization-selected optical feedback in a VCSEL. A VCSEL used in the experiments has the disc diameter of 16 μm and the oscillation wavelength of 780 nm with a maximum optical power of 10 mW. The external mirror is located at 90 cm away from the front facet of the laser. For a reference, the L-I characteristics of solitary mode together with near-field oscillation

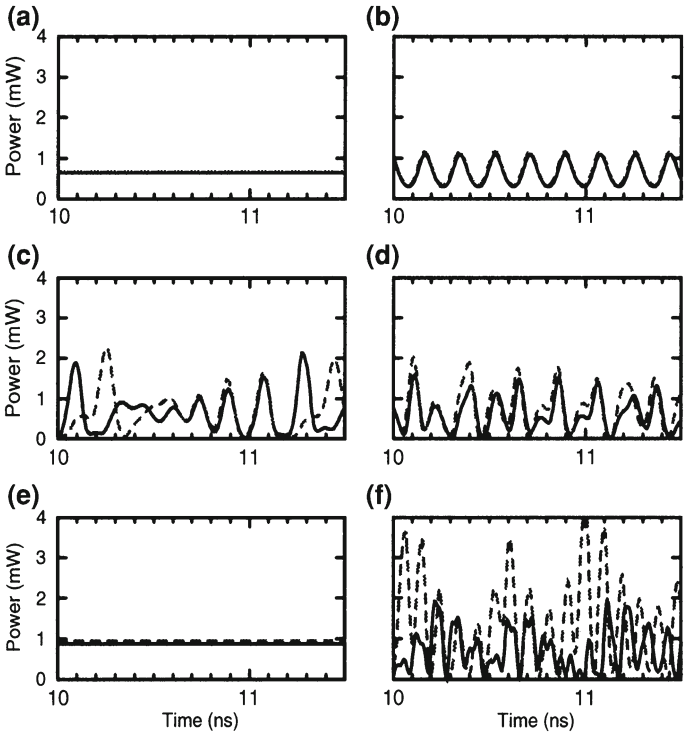

Fig. 8.21 Temporal evolutions of output power under two-mode operation with 4 μm disc contact (weak coupling) VCSEL for several feedback levels. *Solid* and *dashed* curves represent the LP_{01} and LP_{11} modes, respectively. External feedback rate κ of **a** 0, **b** 1.6×10^{-4}, **c** 5×10^{-4}, **d** 8.9×10^{-4}, **e** 1.6×10^{-3}, and **f** 2.8×10^{-3} [after Law and Agrawal (1998); © 1998 OSA]

patterns at 7.0, 12.0, 18.0, and 24.0 mA are displayed in Fig. 8.22a. For steady-state oscillations, the complementary features of the oscillation patterns between the two polarization modes are clear, especially at higher bias injection current, which is the typical nature of VCSELs either for fast or slow dynamics. This laser has no clear polarization switching between the crossed polarization modes. As noted, L-I characteristics of VCSELs strongly depend on device structures and used materials. Though the total L-I characteristic shows an almost linear relation for the increase of the bias injection current, each polarization component has quite different features depending on the respective VCSEL structures. For example, the L-I characteristics of y- and x-polarization modes are quite different from those for one in Fig. 8.14 that shows a clear polarization switching. As a result, the near-field pattern for each VCSEL is also dependent on the device structures. For the case of total optical feedback in Fig. 8.22b, the threshold of the y-polarization mode slightly reduces from 6.4 to 6.2 mA, while the threshold of the x-polarization mode increases from 6.4 to 6.8 mA. The slope efficiency increases due to the optical feedback, but only slight changes of the L-I curves are visible. However, the spatial modes are

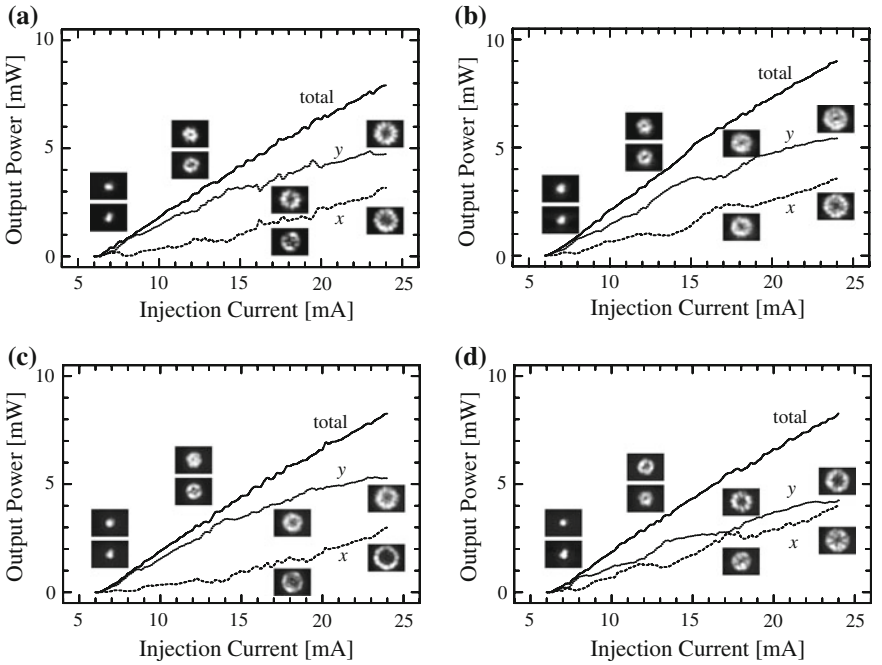

Fig. 8.22 Effects of optical feedback in VCSELs. Experimentally obtained L-I characteristics and near-field patterns for **a** solitary oscillations, **b** total optical feedback (intensity feedback of 9.8 %), **c** y-polarization feedback (feedback of 6.1 %), and **d** x-polarization feedback (feedback of 6.0 %). The *upper* mode patterns in the insets are for y-polarization mode, while the *lower* ones for x-polarization mode

affected by the optical feedback, especially in higher bias injection current. In the case of y-polarization optical feedback, the trends of the threshold reduction are almost the same as for the case of the total optical feedback. However, the crossed polarization component (x-polarization mode) is greatly suppressed. On the other hand, two modes compete with each other in the case of y-polarization feedback. As a result, the laser becomes less stable at this amount of the optical feedback and it is oscillated with lower spatial orders. Polarization selective optical feedback provides quite interesting dynamics of VCSELs, and it is very important from the viewpoint of laser control.

VCSELs have been newly developed and they themselves show various dynamics under solitary oscillations and external perturbations. Therefore, the dynamics have not been well understood yet and studies are still undergoing. As another example of dynamics in VCSELs, we here show self-oscillation properties when a portion of the laser output power is injected back into the laser after having rotated its polarization by 90° with respect to the initial laser polarization state (Jiang et al. 1993). When the two polarization components of the lights are orthogonally returned to the laser from a reflector with short distance, the y-polarization component coherently couples

with the x-polarization component and the x-polarization component also coherently couples with the y-polarization component in as far as the corresponding oscillation wavelengths are assumed to be almost the same. Figure 8.23 shows the experimental waveforms of self-modulations in VCSELs. In this experiment, a laser that shows a clear polarization switching is used. Self-modulations are observed both for the bias injection currents above and below the polarization switching point. As square wave is observed for a long external feedback, while sinusoidal waveforms are observed for a short external feedback. As can easily be recognized, the waveforms of the y-and x-polarization components show anti-phase oscillations. The frequency of the oscillation is half of the frequency for the external cavity length. The polarization rotation feedback induces polarization injection locking in the VCSEL and leads to a switching of the polarization state, then self-modulation occurs in its output. The phenomenon is quite similar to injection locking in a regenerative amplifier, where very weakly injected light is sufficient to lock the laser to the incident frequency. Under the same configuration, a self-modulation with a frequency of 6 GHz is obtained for a short cavity length of 1 cm. These self-modulation oscillations can be used as light sources for high-speed pulse sequences. Masoller and Abraham (1999a,b) presented the numerical simulations for the model considering the population difference between the carrier densities with positive- and negative-spin values in VCSELs and obtained the generations of self-modulation square waves. It is noted that similar square-wave generation is also observed in narrow-stripe edge-emitting semiconductor lasers with polarization-rotated optical feedback as discussed in Sect. 5.8.2. In that case, the frequency of pulses is also twice of the round-trip time of light in the external feedback loop. Therefore, square wave generation is a universal feature in any semiconductor lasers with polarization-rotated optical feedback.

8.3.8 Short Optical Feedback in VCSELs

In Sect. 5.4.2, we discussed typical regular pulse package dynamics with LFFs induced in short cavity optical feedback in narrow-stripe edge-emitting semiconductor lasers. Regular pulse package dynamics are also observed in VCSELs with short cavity optical feedback. However, VCSEL has complex dynamics of orthogonal polarization modes and the characteristics of the pulse package are substantially affected by the polarization dynamics. Thus, we cannot observe exact regular pulse oscillations as in the case of narrow-stripe edge-emitting semiconductor lasers, due to the competitions of the crossed-polarization modes. Though the device structure of VCSELs is fairly different from that of common semiconductor lasers, the relaxation oscillation frequency is mainly determined by the gain coefficient and the photon lifetime (see (3.71)). Thus, the relaxation oscillation frequency is almost the same order as that of narrow-stripe edge-emitting semiconductor lasers as far as the emitting light powers are the same. The definition of short cavity is that the cavity length is within the length corresponding to the relaxation oscillation frequency, which is usually less than centimeters. For example, in a VCSEL with a very short external

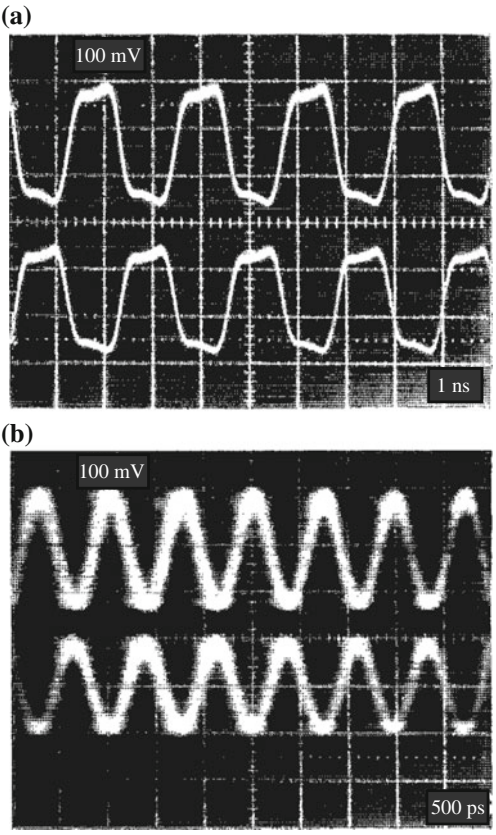

Fig. 8.23 Waveforms of polarization self-modulation signals corresponding to extended cavity lengths of **a** 16.5 cm and **b** 5.3 cm at a bias injection current of $J = 1.51 J_{\text{th}}$. The bias injection current is above the point of the polarization switching. *Upper trace* y-polarization, *lower trace* x-polarization [after Jiang et al. (1993); © 1993 AIP]

cavity condition ($\sim 10\,\mu$m), the laser and the external cavity conform a composite cavity and one polarization mode shows a periodic undulation of the output power for a period of $\lambda/2$ with the change of the external cavity length. In this state, the other mode is also excited alternately to the orthogonal mode, thus showing anti-phase oscillation for the external cavity length (Arteaga et al. 2006).

Tabaka et al. (2006) investigated the pulse package dynamics with LFFs including polarization modes in a short external cavity VCSEL. As a result, for the increase of the injection current, switching from one polarization mode to the other with orthogonal polarization direction is observed. The existence of the two polarization modes in VCSELs can give rise to an additional polarization mode competition dynamics in the presence of feedback. Figure 8.24 shows the experimental results of the polarization resolved dynamics. The VCSEL with an oscillation wavelength of 986 nm has the solitary threshold of $I_{\text{th}} = 3.7$ mA and shows polarization switching at the bias injection current of $I = 4.2$ mA. The external cavity length is 6.5 cm and the mirror reflectivity is 0.3, which results in a threshold reduction of 22 % from the solitary laser oscillation. The relaxation oscillation frequency at $I = 5.2$ mA

corresponds to the external cavity length of 6.5 cm. Therefore, the observed dynamics in Fig. 8.24 satisfy the short cavity condition. In Fig. 8.24a the amplitude of the peaks is still small and the shape of the single pulse package envelope is not very regular. However, the envelope of the packages can be clearly identified, which indicates that the pulse packages in the two polarization modes are almost periodic with a characteristic frequency. The pulse package dynamics in the two polarization modes can be much better recognized at $I = 3.4\,\mathrm{mA}$, in Fig. 8.24c. In actual fact, the total intensity shows a quite regular pulse package oscillation, but the polarization resolved pulse package dynamics is not as regular as for the total intensity. The reason for this is that we observe polarization mode competition, underlying the pulse package dynamics, reducing the regularity of the pulse package dynamics in each polarization mode. This mechanism becomes more relevant at a higher injection current, approaching the polarization switching point. A gradual loss of the regularity in the pulse package dynamics as the bias injection current is increased from 3.2 to 3.8 mA. In the time series in Fig. 8.24, the pulse package dynamics temporarily take place in one of the polarization modes only in some cases and the second mode is almost turned off. In other cases the pulse package dynamics take place in the two polarization modes simultaneously. The first case of dynamics, in which the pulses are emitted in one polarization mode only, is referred to as type I pulse packages. The second case of dynamics, in which the pulse package dynamics take place in the two polarization modes simultaneously, is called type II pulse packages. Similar interplay of the feedback induced complex dynamics and polarization mode competition has been found numerically in the long external cavity regime (Sciamanna et al. 2003a) and experimentally confirmed (Naumenko et al. 2003; Sondermann et al. 2003).

The cross-correlation functions corresponding to the left column are shown in the right column of the figure. By increasing the injection current, we observe a continuous decrease of the modulation amplitude at the timescale of the multiples of the pulse package envelope until the peaks completely vanish, which we demonstrate in Fig. 8.24h. At higher levels of the bias injection current, the laser first emits pulses with high amplitudes while the amplitude of the following pulses progressively decreases. Moreover, in the regime of high injection currents, well above the polarization switching point, the cross-correlation function becomes negative for all time lags. This substantial change in the shape of the cross-correlation function can be associated with a remarkable change of the pulse package dynamics, reflecting a gradual transition from type II pulse package to type I one.

8.3.9 Optical Injection Dynamics in VCSEL

We have discussed optical injection phenomena in narrow-stripe edge-emitting semiconductor lasers in Chap. 6. The technique is developed for frequency-locking and stabilizing injected lasers, but the lasers are sometimes destabilized by optical injection and show a rich variety of chaotic dynamics for certain ranges of the injection parameters as has already been discussed. In the case of narrow-stripe edge-emitting

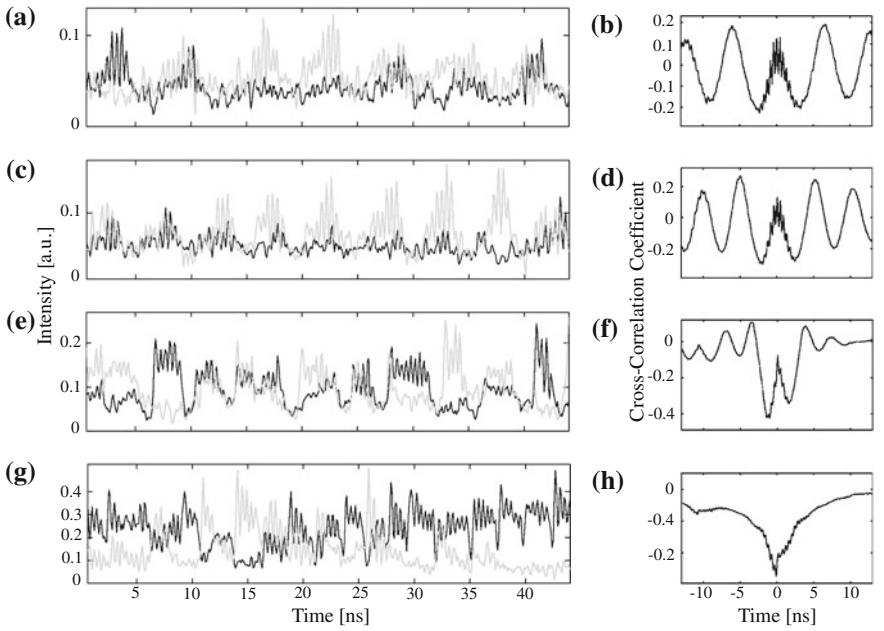

Fig. 8.24 Polarization resolved dynamics of a VCSEL in the pulse package regime for the injection current. *Left* column is time series and *right* column the corresponding cross-collation function. **a** $I = 3.2\,\mathrm{mA}$, **c** $I = 3.4\,\mathrm{mA}$, **e** $I = 3.8\,\mathrm{mA}$, and **g** $I = 5.0\,\mathrm{mA}$. *Gray plot* corresponds y-polarization and *black plot* x-polarization [after Tabaka et al. (2006); © 2006 AIP]

semiconductor laser, the laser usually emits a light with a linear polarization (TE mode) and the same polarization is used as an injection light. Once in a while, polarization-rotated optical injection (TM mode injection) is applied to obtain a chaotic light source in narrow-stripe edge-emitting semiconductor lasers. Normally, the excitation of the orthogonal mode is very small in ordinary edge-emitting semiconductor lasers. However, the situation completely changes in VCSELs, since the lasers have the ambiguity of oscillations for polarization directions. In VCSELs, optical injection including the polarization direction plays a crucial role in the dynamics of the laser oscillations even if the laser is oscillated at a certain fixed polarization with a solitary mode. Depending on the injection conditions, the laser shows a rich variety of dynamics; stable and unstable injection locking, and even chaotic oscillations by the optical injection. The typical feature of the dynamics is the polarization switching between the two orthogonal polarization modes. Further, the polarization is greatly affected by small changes of the bias injection current or the device temperature may result in a polarization switching between the two linearly polarized modes. Control of the VCSEL polarization is a major issue in telecommunication applications. For well polarization controlled VCSELs, polarization switching may be interesting for the development of all optical switches.

The typical feature of VCSEL oscillations is the polarization switching for the increase or decrease of the bias injection current. By optical injection, the laser shows different dynamics depending on the injection direction for the polarization mode and also the frequency detuning. As a general trend, the polarization switching current is almost fixed to that of the solitary oscillation for a small optical injection. For the increase of optical injection level, the switching current increases. Finally, the polarization switching is eliminated for a strong optical injection like the effect of optical feedback and the laser oscillates at only a single polarization mode (injected polarization direction), although the particular mode may show chaotic oscillations. In optical injection to a VCSEL, we can obtain a similar injection map of Fig. 6.6 in Sect. 6.2.3 as far as the injection polarization direction is the same as the oscillation mode of the VCSEL (Li et al. 1996; Ryvkinn et al. 2004; Hurtado et al. 2010). However, polarization switching dynamics encounter for an orthogonal polarization injection and the laser shows a rich variety of dynamics in its output power and polarizations. Figure 8.25 shows examples of dynamic-state maps in the phase space of the optical injection and the frequency detuning calculated from the spin-flip model discussed in Sect. 8.3.3. Here, we show different conditions of the polarization directions of optical injection and the bias injection points. The important parameters related to the polarization switching current and the laser oscillation frequency are set to $\gamma_p = 30$ rad·ns^{-1} and $\gamma_a = 1$ ns^{-1}. Under this condition, the normalized polarization switching current is $\mu_{sw} = 1.3$ and the frequency difference between the y- and x-polarization oscillations is about 9 GHz. Figure 8.25a, b are the results for parallel optical injections, while Fig. 8.25c, d are those for orthogonal optical injection. Figure 8.25a is the map for the optical injection to y-polarization when the laser oscillates at y-polarization mode ($\mu = 1.2$). On the other hand, Fig. 8.25b is that for the optical injection to x-polarization under the laser oscillation at x-polarization mode ($\mu = 1.4$). The general trends of the dynamics are quite similar to the case of narrow-stripe edge-emitting semiconductor lasers. As is expected, for higher bias injection, the stable oscillation region shrinks and chaotic oscillation areas are expanded. Figure 8.25c is the map for the optical injection to x-polarization when the laser oscillates at the y-polarization mode ($\mu = 1.2$). While, Fig. 8.25d is that for the optical injection to y-polarization under the laser oscillation at x-polarization mode ($\mu = 1.4$). In the maps of the orthogonal optical injections, the offset frequency detunings of ± 9 GHz correspond to the frequency differences between the two polarization components of the laser oscillations. Except for the offset of the frequency detuning, one obtains similar dynamics for parallel optical injection to VCSELs. However, it is noted that unlocking regions are widely observed at lower injection ratio in these cases.

In order to represent the richness of the polarization dynamics in VCSELs with orthogonal optical injection including wide range of frequency detuning and also large dynamic range of optical injection power, the map of the boundaries of different dynamics is experimentally drawn as usual in the phase space of the frequency detuning and the injection power in Fig. 8.26 (Altés et al. 2006; Gatare et al. 2006). The laser is under the x-polarization oscillation with a single spatial mode (the fundamental transverse mode) above the polarization switching point, hence the

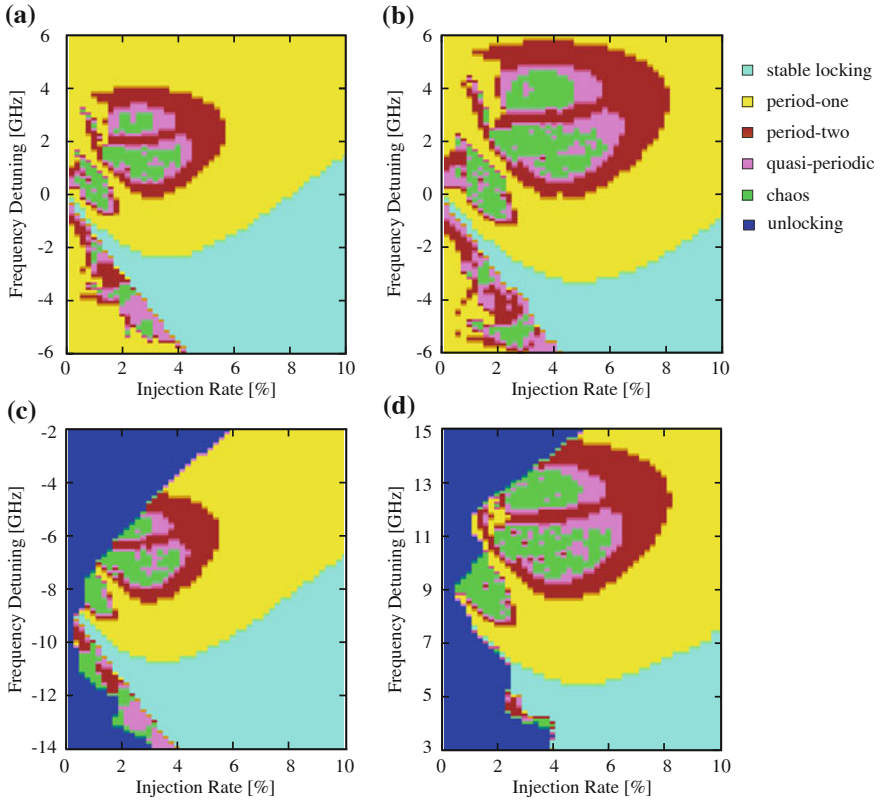

Fig. 8.25 Maps of dynamic states of an optically injected VCSEL in the phase space of optical injection rate and the frequency detuning between the injection laser and the VCSEL. The maps are calculated from the spin-flip model. The polarization switching current is $\mu = 1.3$. Parallel optical injection maps for the oscillation modes at **a** $\mu = 1.2$ (y-polarization mode is injected) and **b** $\mu = 1.4$ (x-polarization mode is injected). Orthogonal optical injection maps for the non-oscillation modes at **c** $\mu = 1.2$ (x-polarization mode is injected) and **d** $\mu = 1.4$ (y-polarization mode is injected)

main y-polarization mode is suppressed. The injection power in the horizontal axis in Fig. 8.26 is normalized to the solitary oscillation power at this bias point. The VCSEL is externally injected by the linear polarization light with y-polarization mode and the x-polarization mode dynamics of the laser is investigated. The thin solid and gray lines are the polarization switching boundaries (switch-on points) for the increase of the bias injection current. While the dashed and the thick solid lines are polarization switching boundaries (switch-off points) for the decrease of the bias injection current. In the regions S1 and S2, the frequency of VCSEL emission is locked to the master laser. However, in the case of S2, it is the first order transverse mode and not the fundamental transverse mode that locks to the master laser, the fundamental transverse mode then being suppressed. The unlocking of the first order

transverse mode happens at smaller values of the injection power, describing bistable region B2 between the fundamental and the first order transverse mode both with the same polarization.

In Fig. 8.26, two polarization bistable regions are observed in a regime of fundamental mode emission, which correspond to two different ways of polarization switching. The first one is with frequency locking in region B1 and is confined between the gray and the thick solid lines. The second polarization bistable region of B3 is confined between the dash and the thin solid lines where the polarization switching happens without frequency locking. The two bistable regions are connected at a detuning of 2 GHz, which coincides with the birefringence frequency splitting between the two linear polarization modes. This means that when the master laser is biased at the frequency of the y mode (the suppressed mode under the bias injection current) a dramatic change of dynamics occurs from polarization switching with injection locking to polarization switching without locking. For larger positive or negative detunings, the switching power is larger, and moreover the switching power is larger for a negative than for a positive detuning value. This experimental feature agrees with theoretical results on a VCSEL rate equation model (Sciamanna and Panajotov 2005). It is noted that the widths of the injection-locking regions S1 and S2 and of the bistability region B1 increase with the detuning. On the other hand, the width of the bistability region B3 remains approximately constant when changing the frequency detuning. This bistable region B3 is also strongly influenced by the locking of the first order linear polarization mode (S2). For small positive detunings ranging from about 0–10 GHz, complicated dynamics like wave mixing, subharmonic resonance, sustained limit cycle oscillation, period doubling, and chaotic regimes (C) are observed as shown in the inset in Fig. 8.26. The example shown here is the polarization dynamics of orthogonally injected VCSELs at the bias injection current above the polarization switching point. Similar but somewhat different dynamics can be found for the bias injection current below the polarization switching point (y-polarization mode oscillations) and x-polarized optical injection (Sciamanna and Panajotov 2005, 2006).

8.4 Broad-Area Semiconductor Lasers

8.4.1 Theoretical Model of Broad-Area Semiconductor Lasers

The high power semiconductor laser is a promising laser device for various industrial applications of high-energy optical sources, since the power conversion efficiency from electricity to light in those semiconductor lasers is much higher than in other lasers (the efficiency is more than 50 %). Such high power and high efficiency lasers can be used for light sources of laser welding, pumps for solid-state lasers, and laser fusion. Also high power semiconductor lasers are used as light sources for laser printing and laser display. Currently, a high power semiconductor laser over

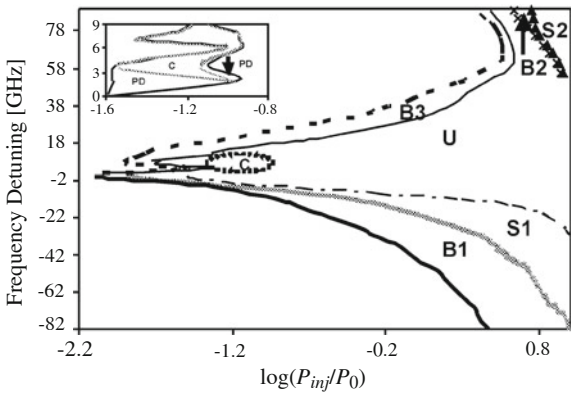

Fig. 8.26 Mapping of the dynamics of a VCSEL subject to optical injection in the phase space of the frequency detuning and the optical injection power. The laser is oscillated at the *y*-polarization mode above the polarization switching point. The injected linear polarization light is set to be *x* mode. *Thin solid line* and *gray line* are polarization-switching boundaries for the increase of the bias injection current. *Dashed line* and *thick solid line* are polarization-switching boundaries for the decrease of the bias injection current. B1, B2, B3: bistable regions, S1, S2: stable injection-locking regions, U: unlocking region, C: chaotic region. The inset shows period-doubling (PD) dynamics around the region of instabilities C [after Altés et al. (2006); © 2006 IEEE]

1 kW of output is deviced by stacking lasers as arrays. One of the technologies for high power semiconductor lasers is a broad-area laser that has a broad stripe width (∼100 μm which is about twenty times or more larger than that for ordinary narrow-stripe edge-emitting semiconductor lasers). The broad-area semiconductor laser has a broad stripe width of the active region as its name suggests. Therefore, the effects of the carrier diffusion and the diffraction of light in the active region are essential for such a structure (Diehl 2000; Gehrig and Hess 2003). Other than that, the broad-area semiconductor laser has the same structure as ordinary narrow-stripe edge-emitting semiconductor lasers. Figure 8.27 is an example of the device structures. The thickness of the active layer is larger than that of ordinary narrow-stripe edge-emitting semiconductor lasers, but the oscillation of the TE mode is usually expected. However, under special installation of the device structures such as stress-induced anisotropy for the device, a broad-area semiconductor laser may oscillate at the TM mode. The internal cavity length is of the same order as for narrow-stripe edge-emitting semiconductor laser or several times larger than that. The longitudinal dimension is typically 1 mm. Except for wide stripe, the laser usually has a high reflectivity of light at the back facet and a low reflectivity at the front facet to avoid catastrophic optical damage (COD), which is discussed in Sect. 8.4. The output power of a broad-area laser is more than 100 mW and even 10 W oscillation is realized as a single emission light source.

Except for the advantage of high power operation, the qualities of the laser beam show rather poor performances. For example, broad-area semiconductor lasers usually operate at multimode both for the longitudinal and transverse modes. Depending

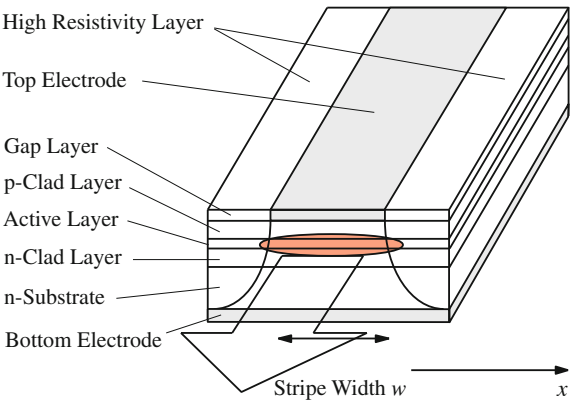

Fig. 8.27 Device structure of a broad-area semiconductor laser. The stripe width w of the active layer is as broad as $\sim 100\,\mu\text{m}$

on the bias injection current, spatial mode excitation or suppression occurs in the laser beam. As an ordinary tendency, the laser transversely oscillates with a few lower spatial modes at low bias injection current, while higher spatial modes are further excited with the increase of the bias injection current. This effect originates from the increased importance of carrier dynamics; with increasing current the nonlinear spatial and spectral dynamics lead to an increased rise in the gain for the higher spatial modes. Moreover, the carrier-induced refractive index induces dynamic filamentations in the gain medium, which is a principal cause of multimode dynamics. The far-field pattern of a broad-area laser typically has a twin-peak at low bias injection current. There exists a carrier hole-burning effect in the active region along the stripe width at high bias injection current. The positions of the hole-burning change and fluctuate with time and this gives rise to pulsating oscillations with picosecond and fast spatio-temporal filamentations (Hess et al. 1995; Marciante and Agrawal 1998; Scholz et al. 2008). Filamentation of broad-area semiconductor lasers, which shows zigzag motions of high intensity peaks along the internal cavity (typically the time size is several tens of picoseconds and the spatial size of several micron-meters), is one of the typical features of broad-area semiconductor lasers and it much deteriorates the laser performance. The broad-area semiconductor laser is also sensitive to external perturbations. In the following, we discuss the dynamics both without and with external perturbations.

The broad-area semiconductor laser itself is also an unstable device due to the spatial dependence in the laser oscillations (i.e., the spatial variation is an additional degree of freedom). Broad-area semiconductor lasers usually oscillate with multimode, however, we assume a single longitudinal mode operation for simplicity. Even for the assumption, it is proved that we can well reproduce fundamental dynamics of broad-area semiconductor lasers. Starting from the Helmholtz equation for the complex laser field $E(x,\ t)$($x$is the coordinate perpendicular to the laser thickness in the active layer, i.e., the direction along the laser stripe width), the rate equation is given as (Rahman and Winful 1994; Merbach et al. 1995; Levy and Hardy 1997)

Table 8.4 Characteristic device parameters for broad-area semiconductor lasers at an oscillation wavelength of 780 nm

Symbol	Parameter	Value
G_n	gain coefficient	$2.00 \times 10^{-13}\,\mathrm{m^3\,s^{-1}}$
α	linewidth enhancement factor	3.00
r_1	front facet reflectivity	0.05
r_2	back facet reflectivity	0.95
n_{th}	carrier density at threshold	$5.11 \times 10^{24}\,\mathrm{m^{-3}}$
n_0	carrier density at transparency	$1.30 \times 10^{24}\,\mathrm{m^{-3}}$
τ_s	lifetime of carrier	3.00 ns
τ_{ph}	lifetime of photon	1.88 ps
τ_{in}	round trip time in laser cavity	6.00 ps
D_e	diffraction coefficient	$1.44\,\mathrm{m^2\,s^{-1}}$
D_n	carrier diffusion coefficient	$30\,\mathrm{cm^2\,s^{-1}}$
l	cavity length	500 μm
w	stripe width	50 μm
d	thickness of active layer	0.05 μm

$$\frac{\partial E(x,\,t)}{\partial t} = iD_e\frac{\partial^2 E(x,\,t)}{\partial x^2} + \frac{1}{2}(1 - i\alpha)G_n\{n(x,t) - n_{\mathrm{th}}\}E(x,t) \tag{8.41}$$

where $D_e = c/2k_0\eta^2$ is the diffraction coefficient of light (k_0 being the wavenumber in vacuum). The first term on the right-hand side of the equation is the diffraction effect due to the broad active area. The diffusion effect must also be included in the rate equation for the carrier density $n(x,\,t)$ and it is written as

$$\frac{\partial n(x,\,t)}{\partial t} = D_n\frac{\partial^2 n(x,\,t)}{\partial x^2} + \frac{J}{ed} - \frac{n(x,\,t)}{\tau_s} - G_n\{n(x,t) - n_0\}|E(x,\,t)|^2 \tag{8.42}$$

where D_n is the diffusion coefficient of the carrier and it is defined as $D_n = l_d^2/\tau_s$ (l_d is the diffusion length). In reality, the injection current is a function not only of time but also of the x coordinate. The dynamics of broad-area semiconductor lasers at solitary oscillations are numerically simulated from (8.41) and (8.42). Table 8.4 is an example of characteristic parameters of broad-area semiconductor lasers.

To explain the dynamics not only for the externally emitting light field but also within the laser cavity, a different model for broad-area semiconductor lasers is sometimes employed. In this model, the field amplitude and carrier density in the active region of a broad-area semiconductor laser fluctuate in time and space both for the transverse and longitudinal directions, i.e., x and z directions (z is the direction of light propagation). To analyze the internal local field and carrier density, we must take into account the internal field for the propagating and counter propagating waves and the polarization of the matter. Then, the electromagnetic field equation is numerically solved by using a finite difference time domain (FDTD) method (Acachihara et al. 1993; Hess and Kuhn 1996a,b; Simmendinger et al. 1999). Therefore, such a model

is sometimes used. In the model, the field equation for the forward and backward propagations $E^+(x,\ z,\ t)$ and $E^-(x,\ z,\ t)$ along the $z$direction in the internal active region is given as

$$\pm\frac{\partial E^{\pm}(x,\ z,\ t)}{\partial z}+\frac{\eta}{c}\frac{\partial E^{\pm}(x,\ z,\ t)}{\partial t}$$
$$=\frac{i}{2k}\frac{\partial^2 E^{\pm}(x,\ z,\ t)}{\partial x^2}-(\frac{\alpha_s}{2}+i\gamma_w)E^{\pm}(x,\ z,\ t)+\frac{i}{2}\frac{\Gamma(x)}{\eta^2\varepsilon_0 l}P_N^{\pm}(x,\ z,\ t) \quad (8.43)$$

and the carrier density $n(x,\ z,\ t)$ reads as

$$\frac{\partial n(x,\ z,\ t)}{\partial t}=D_n\left\{\frac{\partial^2 n(x,\ z,\ t)}{\partial x^2}+\frac{\partial^2 n(x,\ z,\ t)}{\partial z^2}\right\}+\frac{J(x,\ z)}{ed}$$
$$-\frac{n(x,\ z,\ t)}{\tau_s}-G_{E,P}(x,\ z,\ t) \quad (8.44)$$

where l is the internal cavity length of the laser, α_s is the linear absorption term, γ_w is the parameter related to transverse and vertical variations of the refractive index due to the waveguide structure, and $\Gamma(x)$ is the confinement factor. $P_N^{\pm}(x,\ z,\ t)$ is the nonlinear polarization of the matter accompanying the laser oscillation and is written as

$$P_N^{\pm}=\frac{2}{V}\sum_k d_{cv}(k)p_r^{\pm}(k) \quad (8.45)$$

where $d_{cv}(k)$ is the optical dipole matrix element and $p_r^{\pm}(k)$ is the microscopic polarization function. The macroscopic generation rate $G_{E,P}$ in (8.44) is given as

$$G_{E,P}(x,\ z,\ t)=-\chi''\frac{\varepsilon_0}{2\hbar}(|E^+(x,\ z,\ t)|^2+|E^-(x,\ z,\ t)|^2)$$
$$+[\frac{-i}{2\hbar}\{E^+(x,\ z,\ t)P^{+^*}(x,\ z,\ t)$$
$$-E^-(x,\ z,\ t)P^{-^*}(x,\ z,\ t)\}+c.c.] \quad (8.46)$$

where χ'' is the imaginary part of the susceptibility. When the variables for the z direction in (8.43) and (8.44) change slowly in time, the equations reduce to the rate equations at the exit face of the laser given by (8.41) and (8.42).

8.4.2 Dynamics of Broad-Area Semiconductor Lasers at Solitary Oscillations

In this subsection, the dynamics of broad-area semiconductor lasers at solitary oscillations are described. The L-I characteristic is the same as that for narrow-stripe

edge-emitting semiconductor lasers, but the threshold current is much higher because of the broad stripe width and the need of the high carrier injection rate. The laser threshold current is usually larger than 100 mA. In the previous theoretical model, we assume a single mode oscillation for a broad-area semiconductor laser, however, most of the actual broad-area semiconductor laser oscillates with multi-longitudinal mode. Therefore, we must use multimode equations for the real laser model to compare with experiments. However, the single mode model can reproduce well the fundamental characteristics of broad-area semiconductor lasers. The following examples of the numerical simulations are the results for a single longitudinal mode assumption.

As discussed, the rate equations depend on the x coordinate and the spatial modes play a crucial role for the dynamics. Then, we cannot ignore the spatial dependence and must take into account the higher transverse modes. Further, the laser undergoes spatial and temporal complex dynamics due to the self-focusing effects induced by the hole-burning of carriers and the diffraction of light. We will describe the fast dynamics later and, instead, we here discuss the time-averaged far-field profile of a laser oscillation. The output profile of broad-area semiconductor lasers has a significant wavefront distortion and the effect is remarkable for the laser of the gain-guided structure which is easy to fabricate. The far-field pattern of a broad-area semiconductor laser typically has a twin-peak profile. For multi-transverse-mode lasers, the beam quality factor is introduced to evaluate the beam quality. The beam quality factor M^2 of a far-field pattern for a laser is defined as (Hodgson and Weber 1997)

$$M^2 = \frac{D_m \theta_m}{d_0 \theta_0} \approx \left(\frac{D_m}{d_0} \right)^2 \tag{8.47}$$

where d_0 and D_m are the diameters of the ideal Gaussian beam and the observed beam, and θ_0 and θ_m are the divergence angles for the ideal and observed beams, respectively. The value of the beam quality factor M^2 is unity for the ideal beam, but the value for broad-area semiconductor lasers usually ranges from $10-50$ depending on the bias injection current and the stripe width.

Figure 8.28 shows a plot of experimental far-field patterns of a broad-area semiconductor laser for a change of the bias injection current. The profile is spatially averaged. At a lower bias injection current, the laser profile has a single lobe, while the laser shows a typical twin-peak pattern for a higher injection current. The extent of the divergence of the beam in the far field is roughly determined by the average particle size of the filamentation. From this relation, the spatial size of the filamentation at the exit facet of the laser is given as (Hülsewede et al. 2001)

$$\sigma = \frac{4\lambda}{\pi \theta} \tag{8.48}$$

where θ is the diffraction angle at the far-field plane. In Fig. 8.28, the divergence angle is $\theta = 0.17$ radians and the corresponding spatial size of the filamentation at $I = 230$ mA is estimated as 6 μm.

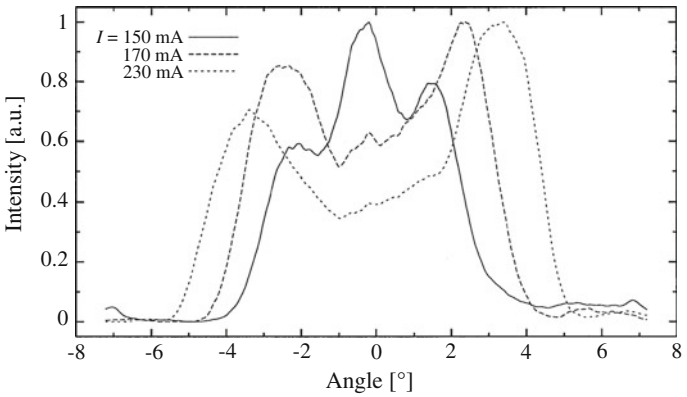

Fig. 8.28 Experimental far-field beam profile of a broad-area semiconductor laser. The laser oscillates at 780 nm and has a stripe width of 50 μm. The threshold current is 140 mA

A laser with a non-negligible spatial structure shows instabilities without any external perturbations. Another example is VCSELs, as we have already discussed. Next, we show a typical example of spatio-temporal dynamics in broad-area semiconductor lasers. Figure 8.29 is numerically calculated near-field and far-field patterns of a broad-area semiconductor laser for a stripe width of 50 μm at a bias injection current of $J = 1.5J_{\text{th}}$. Figure 8.29a, b are the time-resolved near-field and far-field patterns with a time window of 1 ns. The horizontal axis is the position of the exit face of the broad-area semiconductor laser and the vertical axis is the time development of the output power. In the near-field pattern (NFP), we can see that bright spot particles moves back and forth in a zigzag manner along the stripe width. This coil-like pattern is called a filament and it is a typical structure of the light output in broad-area semiconductor lasers. Figure 8.29b shows the corresponding time-resolved far-field pattern (FFP). Figure 8.29c, d are the time-averaged NFP and FFP. In the time-averaged NFP, the light outputs of the both edges in the active region are enhanced. The corresponding time-averaged FFP shows a twin-peaked pattern, which is typically observed in experiments. The calculated M^2 factor in the FFP is about M^2=10. The filament structures are indeed observed in experiments. Figure 8.30 is a filamentation oscillation experimentally observed by a streak camera in a near-field output of a broad-area semiconductor laser (Fischer et al. 1996; Burkhard et al. 1999). The width of migrating filaments is typically around 10 μm and it takes them about several picoseconds to migrate from one edge of the active region to the other. Figure 8.30a is the numerical simulation for the experiment for Fig. 8.30b. Though the model is a single mode, the calculated filamentation is quite similar to the experimental one. Filamentation is universally observed not only for wide stripe lasers but also for semiconductor laser arrays.

The origin of dynamic filamentation in broad-area semiconductor lasers is not fully understood yet. However, the phenomena can be related to the effects of self-focusing, diffraction, and spatial hole-burning, which depends on spatial carrier

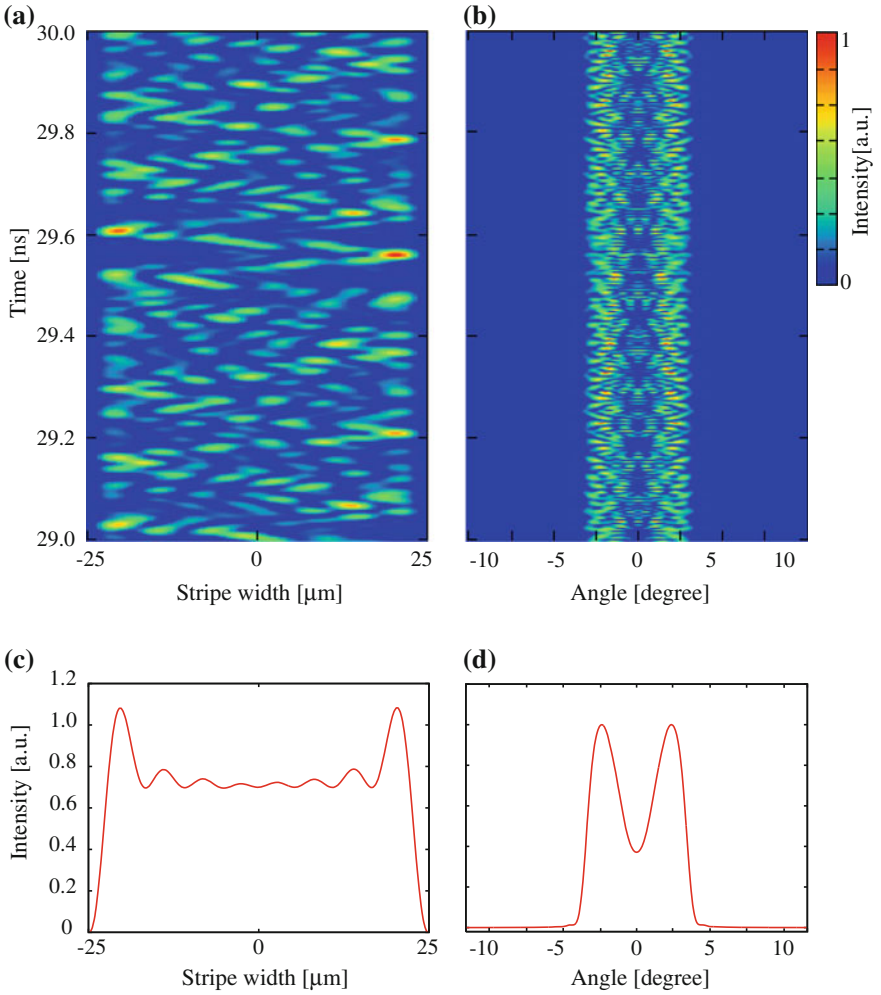

Fig. 8.29 Time-resolved **a** near-field pattern (NFP) and **b** far-field pattern (FFP) of index-guided structure broad-area semiconductor laser at bias injection current of $J = 1.5J_{\text{th}}$. The stripe width is 50 μm. Time-averaged **c** NFP and **d** FFP

diffusion as the relevant physical mechanisms (Hess et al. 1995; Hess and Kuhn 1996b). The self-focusing tends to guide high intensity regions resulting in a decrease of the optical gain. Thus, in the neighboring regions, the gain is higher. In addition, diffraction couples light into this neighboring region so that the spot of high intensity starts to migrate. At the edges of the active area, coupling via diffraction occurs only to one side, leading to a change of direction of migration. Figure 8.31 shows the intensity distribution of the internal cavity calculated from Maxwell-Bloch equations discussed in the previous subsection that include both the space dependence and the

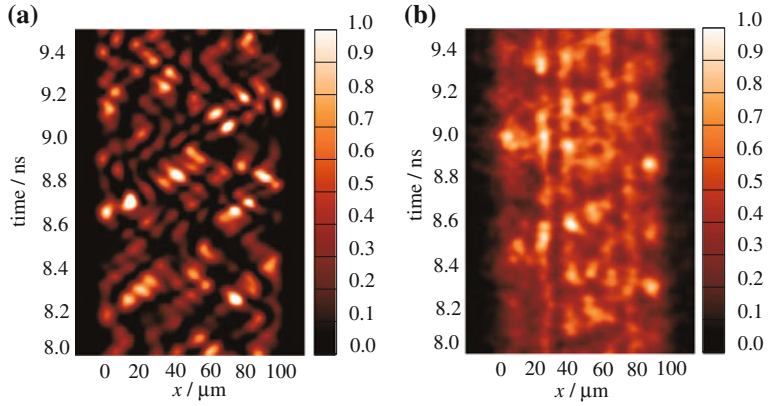

Fig. 8.30 Near-field pattern of filamentation in a broad-area laser. **a** Numerical simulation of filamentation. **b** Experimentally observed filamentation by streak camera. The bias injection current is $J = 2.0 J_{\mathrm{th}}$. The laser has a stripe width of 100 µm and the oscillation wavelength is 814 nm. The parameters of the theoretical result are compatible with those of the experiment. The *horizontal axis* corresponds to the exit face of the active region and the *vertical axis* is the time evolution [after Fischer et al. (1996); © 1996 EDP Sciences]

momentum dependence of the charge carriers and the polarization of matter (Hess and Kuhn 1996b). The bottom of each plot is the front facet with a lower internal intensity reflectivity of 0.33 and the top is the back facet with a higher reflectivity of 0.99. Bright spots of filamentation move with the time evolutions. Other than broad-area semiconductor lasers with constant stripe width, various types of broad-area lasers have been proposed (Levy and Hardy 1997; Fukushima 2000). To control and reduce the effect of filamentation, a flared laser having a tapered cavity has been used. In such lasers, the filamentation has been reduced but different complex spatio-temporal dynamics have been encountered.

We discussed the dependences of the laser dynamics on index- and gain-guide structures in ordinary narrow-stripe edge-emitting semiconductor lasers and the differences between them in Sect. 3.7.1. In the case of narrow-stripe edge-emitting semiconductor lasers, the dynamics strongly depend on the structures not only for solitary oscillations but also for oscillations under external perturbations. However, the differences are reflected only to the parameter values in the rate equations and particular time-dependent dynamics only change for the ranges of the parameter values, whether the laser is an index- or gain-guide structure. Nevertheless, lasers with gain-guide structure show unstable oscillations from the dynamics point of view. On the other hand, a broad-area semiconductor laser has a spatial structure along the stripe width (index- and gain-guided structures) and the differences between the structures give rise to large differences to the spatio-temporal dynamics. The dynamics of filamentations, which are the typical fast dynamics in broad-area semiconductor lasers, are strongly affected by the waveguiding structures.

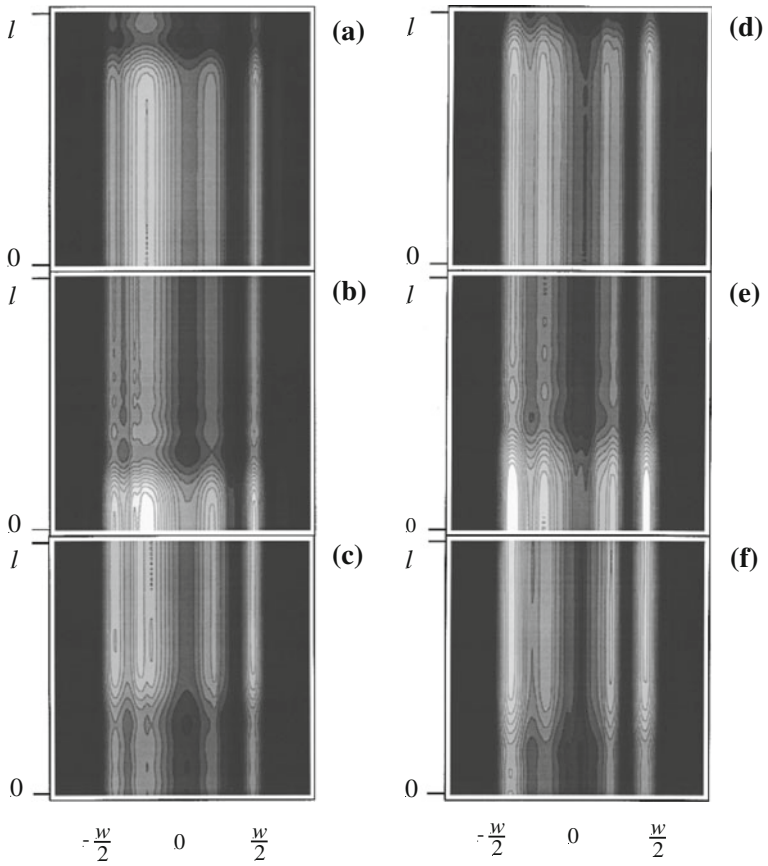

Fig. 8.31 Propagation of filamentary structures in a broad-area semiconductor laser. The individual plots display snapshots showing the equi-intensity regions of the intracavity intensity. **a** At time $t = t_0$, **b** $t_0 + 1$, **c** $t_0 + 2$, **d** $t_0 + 2.8$, **e** $t_0 + 3.5$, and **f** $t_0 + 4.5$ ps. *Dark shading* corresponds to low intensity and *bright colors* to areas of high intensity. The out-coupling facet (mirror reflectivity of 0.33) is located at the *lower* edge of each square. The highly reflecting back-coupling mirror (mirror reflectivity of 0.99) is at the *upper* edge. The longitudinal extension corresponds to 250 μm; the total transverse width ($w = 50$ μm) is 70 μm [after Hess and Kuhn (1996b); © 1996 APS]

Figure 8.32 shows the results of numerical simulations for filamentations in index- and gain-guide structures in broad-area semiconductor lasers, which have the same stripe width of 100 μm and the same bias injection current of $1.5J_{\text{th}}$. In the numerical simulations, the same form of the rate Eqs. (8.41) and (8.42) is assumed, but, in the gain-guide laser, it is assumed that the gain, the refractive index, and the injection current distribution have appropriate parabolic spatial distributions along the stripe width. Figure 8.32a, b show the near-field patterns at the exit faces of the lasers and their space–time correlation functions. The time and spatial sizes of the filaments in the index-guide laser calculated from the correlation function are 4.1 μm and 27 ps,

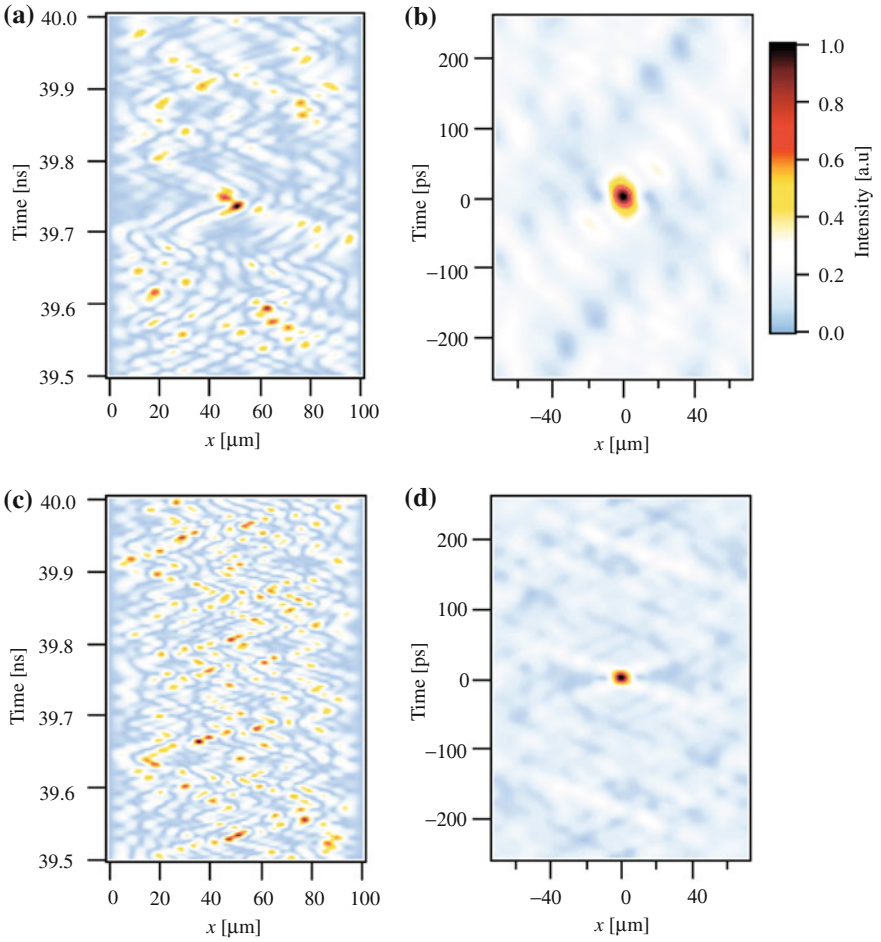

Fig. 8.32 Numerical simulations for near-field patterns in broad-area semiconductor lasers (*left* column) and their spatio-temporal correlations (*right* column) at $J = 1.5J_{\mathrm{th}}$. **a** and **b** Index-guide semiconductor laser, and **c** and **d** gain-guide semiconductor laser. Both lasers have the same stripe widths of 100 μm. Parabolic profiles for the gain, the refractive index, the injection current distribution along the stripe width are assumed in the gain-guide semiconductor laser

respectively, while those for the gain-guide laser are 2.9 μm and 12 ps, respectively. Namely, the gain-guide laser is less stable laser than the index-guide laser and the filaments strongly migrate back and forth along the active layer in the gain-guide laser as far as the values of the device parameters for both the structures are the same. For the increase in the bias injection current, the spatio-temporal size of filaments shrinks and filaments shows strong zig-zag motions along the active layer, as a result, both the lasers similarly become less stable.

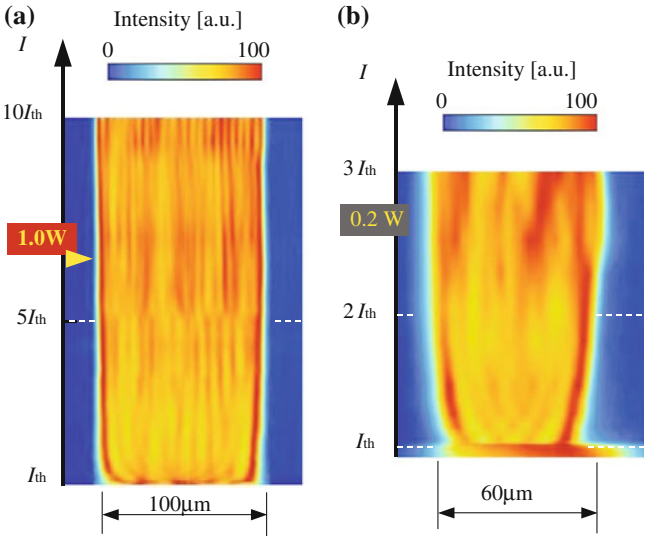

Fig. 8.33 Averaged near-field patterns for index- and gain-guide semiconductor lasers for the increase of the bias injection current. **a** Near-field pattern for an AlGaAs index-guide laser having a stripe width of 100 μm and oscillating at the wavelength of 808 nm. The threshold current is I_{th}=160 mA. **b** Near-field pattern for an AlGaInP gain-guide laser having a stripe width of 60 μm and oscillating at the wavelength of 642 nm. The threshold current is I_{th}=191 mA. Courtesy of SONY Cooperation

This fluctuation of microscopic filaments reflects the performances of macroscopic laser oscillations. Figure 8.33 shows experimental results of the time-averaged intensity distributions at the exit faces of index- and gain-guide broad-area semiconductor lasers for the bias injection current. The horizontal axis points to the exit face of the laser and the intensity distribution at each bias injection current is normalized. Each streak along the bias injection current corresponds to averaged filamentations. We can see different dynamics for several levels of the bias injection current. As already seen in Fig. 8.29, the enhancement of the powers at both edges of the active layer is observable irrespective of the guided structures. Although the two lasers have different stripe widths, values of device parameters, and oscillation frequencies, we can recognize that the gain-guide laser is less stable laser (Asatuma et al. 2006).

8.4.3 Optical Feedback Effects in Broad-Area Semiconductor Lasers

Instabilities in broad-area semiconductor lasers are enhanced by external perturbations. In this subsection, we present some instabilities and chaotic dynamics in broad-area semiconductor lasers subjected to optical feedback. The field equation in

the presence of optical feedback is given as

$$\frac{\partial E(x,\,t)}{\partial t} = iD_e\frac{\partial^2 E(x,\,t)}{\partial x^2} + \frac{1}{2}(1-i\alpha)G_n\{n(x,\,t)-n_{\rm th}\}E(x,\,t) + \frac{\kappa}{\tau_{\rm in}}E(x,\,t-\tau)\exp(i\omega_0\tau) \tag{8.49}$$

In the above equation, the feedback light is always returned to the original position in the active area, however, the assumption may not always be true in experimental situations. The light is intentionally fed back to a different position to control the oscillation and beam profile. In that case, we must introduce the term for the space-dependent optical feedback. The spatial coupling plays an important role in the laser dynamics and a locking of the laser oscillations can be expected. The beam quality inevitably deteriorates due to the broad stripe width, however, fabrication of high power laser is at present the primary interest for the development for broad-area lasers and few studies have been reported for the enhancement of beam qualities. However, now the beam quality becomes the important issue for the applications of broad-area semiconductor lasers, for example, a light source for the second harmonic generation of solid-state lasers, laser welding and cutting, optical data storage, and display. Thus, a beam with good quality is expected. One of the beam controls is optical feedback. Figure 8.34 shows a numerical example of the effects of short optical feedback in a broad-area semiconductor laser at the bias injection current of $J = 1.5J_{\rm th}$, the external amplitude reflectivity of $r = 0.06$, and the external mirror length of $L = 0.75$ cm. In the optical feedback, a partial reflection mirror of the width of 15 μm corresponding to the near field is used, so that the lower spatial modes are enhanced in the resulting oscillation. Figure 8.34a is the time-resolved NFP. Except for optical feedback, the condition is the same as that in Fig. 8.29. The filaments shows a rather regular pattern compared with the irregular oscillation of spatio-temporal pattern in Fig. 8.29a. At the same time, the side-peak intensities in Fig. 8.29c in the time-averaged NFP are suppressed and the twin-peak pattern of FFP in Fig. 8.29d becomes a single lobe pattern.

Dynamics similar to those of narrow-stripe edge-emitting semiconductor laser have been experimentally observed by optical feedback to broad-area semiconductor lasers. We show here one of the chaotic evolutions; the evolution of intermittent oscillations to regular chaotic states for the increase of the injection current. Figure 8.35 is an example of chaotic evolutions for the bias injection current at the external cavity length of $L = 30$ cm. The threshold of the used laser is about 140 mA. Figure 8.35a is the laser output power at the free running state just above the threshold. With the optical feedback, the reduction of the threshold is also observed in the broad-area semiconductor laser and the reduction rate is 13.9 % for the external feedback rate of 6 % (in intensity). When the laser is biased at a low injection current, LFFs are observed. In the power recovery process after the power dropout, the timescale of each step is also the same as the time calculated from the external cavity length. With the increase of the bias injection current, the frequency of LFFs changes and the inverse LFFs in which power jump-ups instead of power dropouts appear are

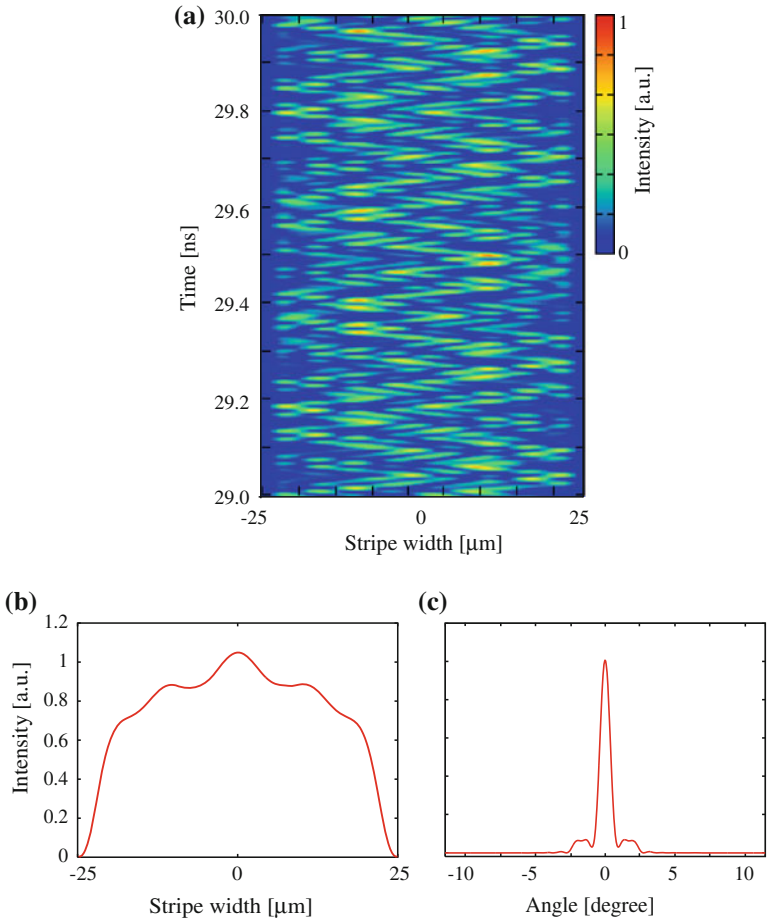

Fig. 8.34 Effect of short optical feedback with a partial reflection mirror of the width of 15 μm corresponding to the near field. **a** Time-resolved NFP at the bias injection current of $J = 1.5\,J_{\mathrm{th}}$, the external amplitude reflectivity of $r = 0.06$, and the external mirror length of $L = 0.75$ cm. Time-averaged **b** NFP and **c** FFP

observed at the bias injection current of 170 mA. Around this bias injection current, there is a kink of the L-I characteristic and the phase of the laser oscillation changes to a different state. At a further increase of the bias injection current, the laser behaves with normal chaotic oscillations, although the waveform still shows LFF-like oscillation (not fully chaotic oscillation in ordinary sense).

In a short optical feedback regime, one can observe similar dynamics of pulse packages as those in narrow-stripe semiconductor lasers. However, there are two schemes of pulse packages; one is a periodic envelope of an LFF frequency with a modulation of the fast oscillation corresponding to the external optical feedback loop, which is a familiar pulse package observed in a narrow-stripe edge-emitting

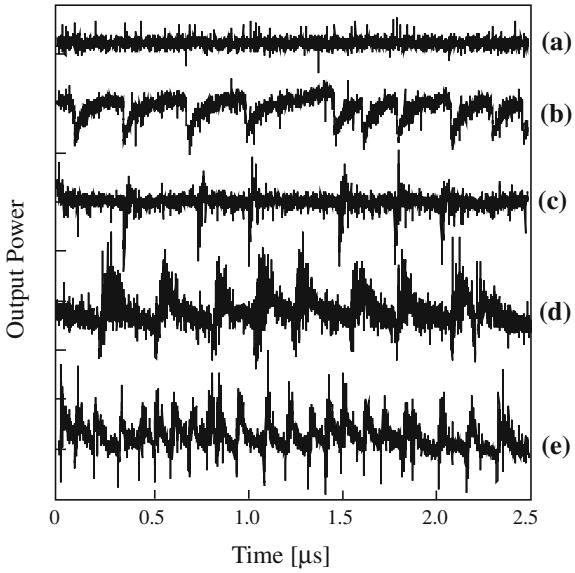

Fig. 8.35 Experimentally observed chaotic evolution for bias injection current in broad-area semiconductor laser. **a** Solitary oscillation at 140 mA. Optical feedback at bias injection currents **b** 150, **c** 162, **d** 170, and **e** 190 mA. The external cavity length is $L = 30$ cm and the external feedback strength is 6 % in intensity. The laser used is the same as in Fig. 8.28

semiconductor laser. The other one is a pulse package of an envelope of the external optical feedback loop with the fast regular oscillation of filament pulses, which is a unique feature in broad-area semiconductor lasers (Tachikawa et al. 2010). Edge-emitting semiconductor lasers are also very sensitive to the phase. Phase sensitivity also exists in broad-area semiconductor lasers subjected to optical feedback and the dynamics are much affected by the absolute phase of the external cavity (Martín-Regalado et al. 1996a,b). The other effects of frequency-filtered optical feedback, spatial-filtered optical feedback, and grating feedback have been studied (Gaciu et al. 2007). We return the subject of optical feedback in broad-area semiconductor lasers from the viewpoint of laser control in Chap. 10.

One of the important issues for the practical applications of broad-area semiconductor lasers, such as laser cutting, is catastrophic optical damage (COD) induced by optical feedback from a target. In ordinary narrow-stripe edge-emitting semiconductor lasers, catastrophic optical damage is also a serious problem when the laser is biased at a high injection current. The performance of the laser oscillations is significantly degraded by catastrophic optical damage and, worst case, the laser oscillation stops by the damage. The catastrophic optical damage is a critical problem in laser cutting using high power broad-area semiconductor lasers. Takiguchi (2006) investigated the conditions for the occurrence of catastrophic optical damage in broad-area semiconductor lasers from the viewpoint of laser dynamics. Figure 8.36 shows an example of catastrophic optical damage observed in an AlGaAs index-guide broad-area semiconductor laser having a stripe width of 50 μm. Under filamentation oscillations in broad-area semiconductor laser, a large power is concentrated to a filament within a short time, and this effect together with a large optical feedback

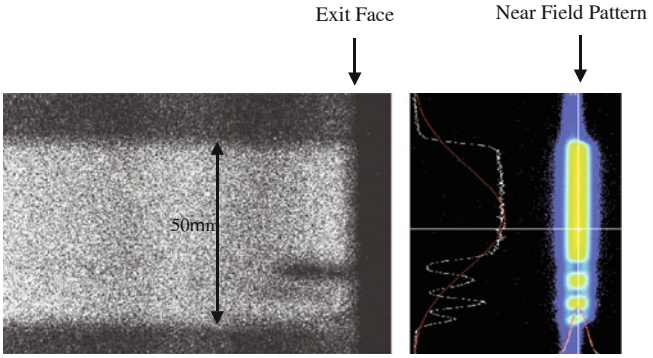

Fig. 8.36 Catastrophic optical damage (COD) induced by optical feedback in an index-guided broad-area semiconductor laser with a 50 μm stripe width and an oscillation wavelength of 808 nm. *Left* top view of the front facet. COD can be seen in the lower part of the laser. *Right* intensity profile of the cathode luminescence image at the front facet. Dips of light emissions corresponding to the front facet can be seen. Courtesy of SONY Cooperation

intensity may damage the laser. Thus, microscopic filamentations greatly affect the catastrophic optical damage, but the detailed study for catastrophic optical damage with the relation of laser dynamics has not been fully understood yet. The study is very important to prevent fatal catastrophic optical damage in broad-area semiconductor lasers as a practical issue.

8.4.4 *Effects of Optical Injection in Broad-Area Semiconductor Lasers*

Similar to the optical feedback effects in broad-area semiconductor lasers, the injection of an external coherent resonant light can lead to the excitation and selection of specific transverse modes depending on the power and spatial profile of the injected light field (Gaciu et al. 2007; Takimoto et al. 2009). Except for the spatial dependence of the injected field, the field in the presence of optical injection can be described by the same equation as (6.1) and is given as

$$\frac{\partial E(x,\,t)}{\partial t} = iD_e\frac{\partial^2 E(x,\,t)}{\partial x^2} + \frac{1}{2}(1-i\alpha)G_n\{n(x,\,t)-n_{\mathrm{th}}\}E(x,\,t) + \frac{\kappa_{\mathrm{inj}}}{\tau_{\mathrm{in}}}E_m(x,t)\exp(-i\Delta\omega t) \tag{8.50}$$

Again, E_m is the field of the injection laser, k_{inj} is the injection fraction, and $\Delta\omega$ is the frequency detuning between the injection laser and the broad-area laser.

Figure 8.37 shows numerical results of optical injection to a broad-area semiconductor laser (Takimoto et al. 2009). The stripe width of the active layer is 50 μm and the continuous-wave injection beam has a rectangular shape with a width of 40 μm. The beam is symmetrically injected related to the center of the active layer. The frequency detuning is assumed to be $\Delta\omega = 0\,\mathrm{GHz}$ at the bias injection current of $1.5J_{\mathrm{th}}$. The upper plots are the time-resolved filament patterns and the lower traces are the time-averaged intensity profiles of the near-field patterns. The external injection ratio r_{inj} defined by (6.2) is used as a measure of optical injection. At $r_{\mathrm{inj}} = 0.4$ in Fig. 8.37a, the laser still exhibits irregular oscillations, but the filament behavior differs from that of a solitary oscillation (compare with the solitary oscillation in Fig. 8.29) and the temporal duration of the filament is reduced. In the presence of optical injection, the side peak intensities, which exist at solitary oscillation, are suppressed and the laser beam has a flat top-hat profile, as shown in the time-averaged profile. Such a flat top-hat beam shape is very important for practical applications. At $r_{\mathrm{inj}} = 1.2$ in Fig. 8.37b, the laser still undergoes irregular oscillations, but some regular structure can be seen in the pattern and the filament durations are shorter. However, the flat-topped beam profile collapses and spatial periodicity is enhanced with a further increase in the optical injection, thus resulting in the excitation of higher spatial modes as shown in the time-averaged near-field pattern. At $r_{\mathrm{inj}} = 1.6$ in Fig. 8.37c, the near-field pattern shows a remarkable periodic structure and higher spatial modes are strongly excited. Spatio-temproal and spatio-spectral dynamics induced by optical injection are also studied by Gaciu et al. (2007).

8.5 Laser Arrays

Semiconductor laser arrays are also important devices for light sources with high power radiation. The laser may be composed of arrays of broad-area lasers to make an extremely high power laser device. However, here we assume that the arrays consist of ordinary narrow-stripe edge-emitting lasers and consider the interaction among the laser elements. When the separation between the laser arrays is very small, each laser interferes and instability sometimes occurs in the total laser output. In a strict sense, we must consider all the effects of the diffraction and the carrier diffusion as already discussed in Sect. 8.4 (Münkel et al. 1996). However, we consider the situation that the coupling of lights among arrays is a dominant effect and that it is more important than those of the diffraction and the carrier diffusion. We also assume that the coupling only between the neighborhood lasers is strong, as is often the case. Thus, the rate equations for the field amplitude and the carrier density of the jth element are given as (Winful and Rahman 1990; Winful 1992)

$$\frac{\mathrm{d}E_j(t)}{\mathrm{d}t} = \frac{1}{2}(1 - i\alpha)G_n\{n_j(t) - n_{\mathrm{th}}\}E_j(t) - i\frac{\kappa_a}{\tau_{\mathrm{in}}}\{E_{j+1}(t) + E_{j-1}(t)\} \quad (8.51)$$

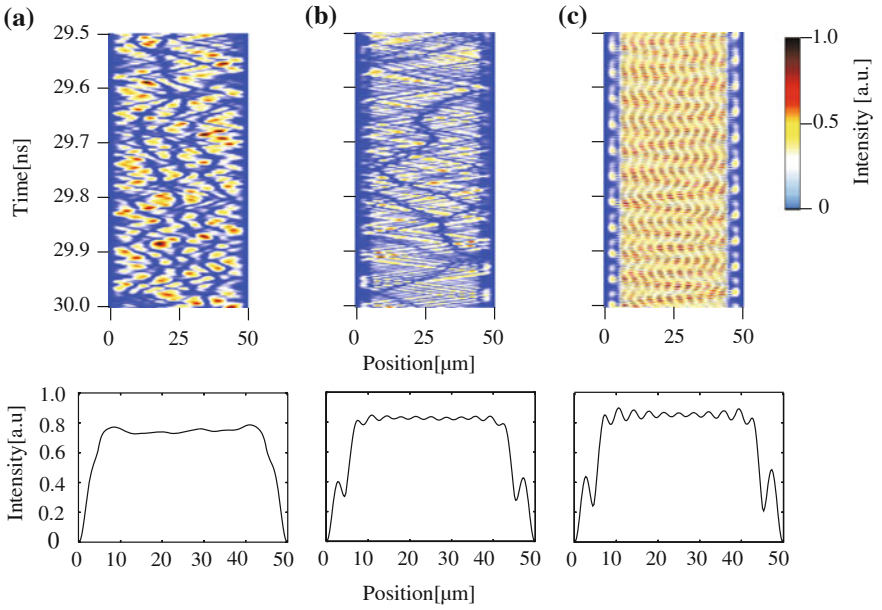

Fig. 8.37 Numerical results of optical injection at the external injection ratios of **a** $r_{inj} = 0.4$, **b** 1.2, and **c** 1.6 at the frequency detuning of $\Delta\omega = 0\,\mathrm{GHz}$ and the bias injection current of $1.5J_{\mathrm{th}}$. The internal reflectivity of the active layer and the refractive index of the laser medium are assumed as $r_0 = 0.1$, and $\eta = 3.59$, respectively. *Upper plots* time-resolved filament patterns and *lower graphs* time-averaged near-field patterns

$$\frac{\mathrm{d}n_j(t)}{\mathrm{d}t} = \frac{J}{ed} - \frac{n_j(t)}{\tau_s} - G_n\{n_j(t) - n_0\}|E_j(t)|^2 \tag{8.52}$$

where κ_a is the coupling ratio between the neighborhood laser elements. The spontaneous emission term is neglected in the above equations. For the numerical calculation of the rate equations, the number of laser arrays is $N + 1$ and the boundary condition is $E_0 = E_N = 0$. The rate equation for the field amplitude has the same form as the well-known equation of the coupled map lattice (CML). The CML shows typical spatio-temporal instabilities and chaos. Therefore, semiconductor laser arrays are essentially chaotic systems. Winful (1992) investigated chaotic dynamics and synchronization of laser arrays based on this model.

As a different approach for the analysis of semiconductor laser arrays, the model of periodic carrier confinement and injection is proposed by extending the theory of broad-area semiconductor lasers (Merbach et al. 1995; Martín-Regalado et al. 1996a,b). In multi-stripe laser arrays, the rate equations remain the same as (8.41) and (8.42). However, the laser is assumed to have a discrete multi-stripe structure along the x-direction as shown in Fig. 8.38. The confinement of the gain arises periodically in the active region. Then, we introduce a periodic confinement factor $\Gamma(x)$ in the wave-guide. Also, the bias injection current $J(x)$ is assumed as a periodic

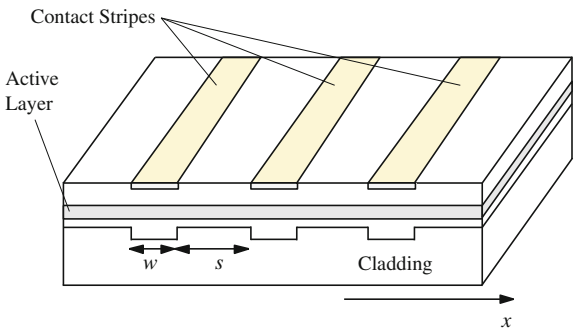

Fig. 8.38 Model of a multi-stripe semiconductor laser array. Only three stripes are displayed

function with the same period. Using these assumptions, the dynamics of the multi-stripe laser are numerically investigated. For the laser arrays, filamentations are also observed. Figure 8.39 shows an example of numerically calculated filamentations (Merbach et al. 1995). The laser has a ten-stripe. We can see filamentations among laser arrays and the dynamics strongly depends on the bias injection current. In Chap. 10, we also return to the control of unstable operation of laser arrays subjected to optical feedback from the viewpoint of laser control.

8.6 Quantum-Dot Semiconductor Lasers

8.6.1 Quantum-Dot Semiconductor Lasers

Quantum-dot semiconductor laser is an important light source for high-speed data communication applications, since it is insensitive to temperature variations and optical feedback, and provides features of high modulation bandwidth and low chirp. The device structure of a quantum-dot laser is almost the same as common narrow-stripe edge-emitting semiconductor lasers. However, in the active layer, small quantum dots as small as nanometer size are fabricated, usually by a self-assembled method of the crystal. A common quantum-dot semiconductor laser is not a single layer device, but several thin quantum-well layers with quantum dots are piled up in the active region. An electron and a hole are captured in a single dot and behave like zero-dimensionally confined particles with a fixed energy state. Thus the light emitted from a quantum-dot semiconductor laser shows a high coherence state. The crystal growth, the device characteristics, and their theoretical treatments have been given in a book of Sugawara (1999). Figure 8.40 is an example of a self-formed quantum-dot structure of InAs in an active region of GaAs (Shoji et al. 1997). Figure 8.40a show a plan view of quantum dots. It is desirable that quantum dots stand in a line on the wetting quantum-well layer and the size of each quantum dot should be the same. However, the control of the crystal growth is very difficult. In spite of irregularities of

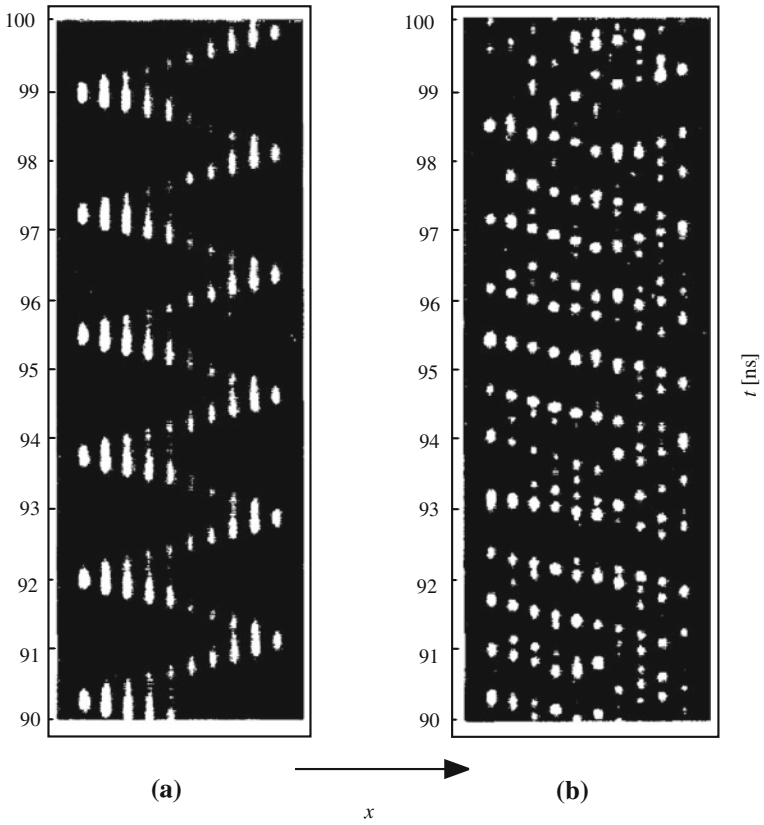

Fig. 8.39 Numerical plots of spatio-temporal output power of a ten-stripe laser array for two different injection currents. **a** $I = 34\,\text{mA}$: periodic state and **b** $I = 44\,\text{mA}$: chaotic state. The threshold current for each stripe is $I_{\text{th}} = 36\,\text{mA}$. The stripe width is $w = 5.0\,\mu\text{m}$ and the stripe separation is $s = 5.8\,\mu\text{m}$ [after Merbach et al. (1995); © 1995 APS]

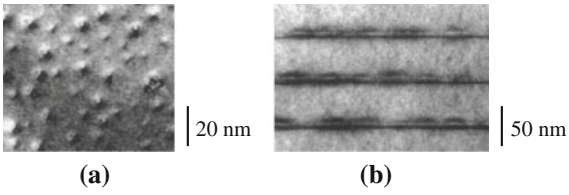

Fig. 8.40 Example of self-assembled quantum-dot structure. **a** plan view and **b** cross-section view [after Shoji et al. (1997)© 1997 IEEE]

the size and the position, the laser can emit a high quality beam. The grown quantum dots in Fig. 8.40b are 20 nm in diameter and 5 nm in height. The areal coverage is about 10 %.

The behaviors of quantum-dot semiconductor lasers are interesting from the viewpoint of nonlinear dynamics. We must consider electron and hole scattering rates to and from dots in the active layer. Therefore, we must introduce the extra differential equations to describe the dynamics. In usual, an addition of extra degree of freedom induces less stable operations for the system. Nevertheless, quantum-dot semiconductor laser is a stable light source even compared with common narrow-stripe edge-emitting semiconductor lasers. Physically, this stability is explained by the limitation of the light emitting region to a confined dot structure. To describe the dynamics, we need to introduce a microscopic model of the quantum-dot structure (Erneux et al. 2007; Lüdge et al. 2008, 2010; Lüdge and Schöll 2009; Grillot et al. 2009; Lüdge 2011). Figure 8.41 is the model of the energy band-structure of a quantum-dot semiconductor laser. Beside the two-level energy states (conduction and valence bands) in common semiconductor lasers, the energy band for a quantum dot is introduced. In this model, we here only consider the ground state (GS) of the energy level for a quantum dot. As far as the bias injection current is not large, the model can well describe the dynamics. For higher bias injection current, the exited states of the energy level should be taken into account (Grillot et al. 2009). In the microscopic model, the dynamics of electron and hole should be treated separately, since the effective masses for electron and hole are different and the carrier scattering rates form the wetting layer to a dot S^{in} and from a dot to the wetting layer S^{out} are also different. In the figure, the subscripts of e and h stand for electron and hole. In the microscopic model, the carrier scatterings into and from quantum dots (Auger process and carrier-phonon interaction) play important roles in the dynamics.

Using the band model in Fig. 8.41, the rate equation for the optical field is given by (Lüdge and Schöll 2009)

$$\frac{\mathrm{d}E(t)}{\mathrm{d}t} = \frac{1}{2}(1 - i\alpha)\left[\Gamma W A\{n_e(t) + n_h(t) - N^{\text{QD}}\} - \frac{1}{\tau_{\text{ph}}}\right] E(t) \tag{8.53}$$

where Γ is the optical confinement factor, W is the Einstein coefficient, and A is the area of the active region. N^{QD} denotes twice the density of the active quantum dots, taking into account spin degeneracy. n_e and n_h are the two-dimensional electron and hole densities in the dots, i.e., the densities are defined as a unit of a single layer. The rate equations for the densities of electrons w_e and holes w_h in the quantum-well wetting layer (WL) is given as

$$\frac{\mathrm{d}w_e(t)}{\mathrm{d}t} = \frac{J}{e} - S_e^{\text{in}}\frac{N^{\text{sum}}}{N^{\text{QD}}}\{N^{\text{QD}} - n_e(t)\} + S_e^{\text{out}}\frac{N^{\text{sum}}}{N^{\text{QD}}}n_e(t) \tag{8.54}$$

$$\frac{\mathrm{d}w_h(t)}{\mathrm{d}t} = \frac{J}{e} - S_h^{\text{in}}\frac{N^{\text{sum}}}{N^{\text{QD}}}\{N^{\text{QD}} - n_h(t)\} + S_h^{\text{out}}\frac{N^{\text{sum}}}{N^{\text{QD}}}n_h(t) \tag{8.55}$$

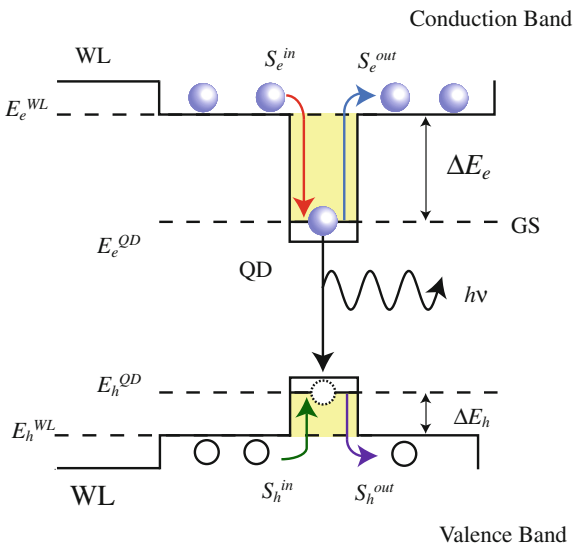

Fig. 8.41 Energy band structure of quantum-dot semiconductor lasers. *WL* quantum-well wetting layer, *QD* quantum dot, *GS* ground state level of a quantum dot, *E* energy level for corresponding state, ΔE energy difference, S^{in} capture rate, S^{out} escape rate

where J is the injection current density. N^{sum} is twice the total quantum-dot density as given by experimental surface imaging, which accounts for reduced gain because due to the size distribution of the quantum dots, namely the active quantum dots N^{QD}, match the mode energy for lasing. A crucial contribution to the dynamics of quantum-dot semiconductor lasers is given by non-radiative carrier–carrier scattering rates. S_e^{in} and S_h^{in} are the electron and hole capture rates into the quantum-dot levels in this process, while S_e^{out} and S_h^{out} are the electron and hole escape rates from the quantum-dot levels. The scattering times for electrons and holes are given by $\tau_e = 1/(S_e^{\text{in}} + S_e^{\text{out}})$ and $\tau_h = 1/(S_h^{\text{out}} + S_h^{\text{out}})$, respectively. As specific equations for quantum-dot semiconductor lasers, we need the following carrier density equations of quantum dots:

$$\frac{\mathrm{d}n_e(t)}{\mathrm{d}t} = S_e^{\text{in}}\{N^{\text{QD}} - n_e(t)\} - S_e^{\text{out}} n_e(t) - WA\{n_e(t) + n_h(t) - N^{\text{QD}}\}|E(t)|^2 \quad (8.56)$$

$$\frac{\mathrm{d}n_h(t)}{\mathrm{d}t} = S_h^{\text{in}}\{N^{\text{QD}} - n_h(t)\} - S_h^{\text{out}} n_h(t) - WA\{n_e(t) + n_h(t) - N^{\text{QD}}\}|E(t)|^2 \quad (8.57)$$

As an example, the values of device parameters for quantum-dot semiconductor lasers are listed in Table 8.5.

Strictly speaking, we must use the above five-variable model to explain the dynamics of quantum-dot semiconductor lasers, however, for the easiness of analytical calculations, such as an analysis for steady-state characteristics, a reduced model is sometimes used (O'Brien et al. 2004; Erneux et al. 2007). In this model, the carrier densities of electrons and holes in the wetting layer are assumed to be the same and

Table 8.5 Characteristic device parameters for quantum-dot semiconductor lasers with five-variable model at an oscillation wavelength of 1.30 μm

Symbol	Parameter	Value
W	Einstein coefficient	$0.7\,\mathrm{ns}^{-1}$
Γ	confinement factor	2.25×10^{-3}
A	WL normalization area	$4\times10^{-9}\,\mathrm{m}^2$
N^{QD}	twice total QD density of lasing group	$0.6\times10^{14}\,\mathrm{m}^{-2}$
N^{sum}	twice total QD density	$20\times10^{14}\,\mathrm{m}^{-2}$
α	linewidth enhancement factor	0.9
τ_{ph}	lifetime of photon	10 ps
τ_{in}	round-trip time in laser cavity	24 ps
ΔE_e	ground state energy difference for electron	190 meV
ΔE_h	ground state energy difference for hole	69 meV
m_e	effective mass of electron	$0.043\,\mathrm{m}_0$
m_h	effective mass of hole	$0.45\,\mathrm{m}_0$
m_0	mass of electron	$9.11\times10^{-31}\,\mathrm{kg}$
r_0	facet reflectivity	0.565

the carrier densities in quantum dots also obey the same dynamics. Therefore, the carrier density equations in the wetting layer reduce to a single carrier density equation. Also the carrier density equations in a quantum dot are replaced as a probability density equation of a single carrier occupation. Then, this model contains three variables of the field E, the occupation probability density ρ of electron and hole pair in a quantum dot, and the carrier density n in the wetting layer as follows:

$$\frac{\mathrm{d}E(t)}{\mathrm{d}t} = \frac{1}{2}(1-i\alpha)[g_0\vartheta\{2\rho(t)-1\} - \frac{1}{\tau_{\mathrm{ph}}}]E(t) \tag{8.58}$$

$$\frac{\mathrm{d}\rho(t)}{\mathrm{d}t} = -\frac{\rho(t)}{\tau_d} - g_0\{2\rho(t)-1\}|E(t)|^2 + [\{1-\rho(t)\}R_{\mathrm{cap}} - \rho(t)R_{\mathrm{esc}}] \tag{8.59}$$

$$\frac{\mathrm{d}n(t)}{\mathrm{d}t} = \frac{J}{e} - \frac{n(t)}{\tau_s} - 2N_d[\{1-\rho(t)\}R_{\mathrm{cap}} - \rho(t)R_{\mathrm{esc}}] \tag{8.60}$$

where g_0 is the gain coefficient, ϑ is the conversion coefficient from the total gain to the two-dimensional surface given by $\vartheta = 2N_d\Gamma/d_d$, N_d is the total carrier density, and d_d is the thickness of quantum dots. R_{cap} and R_{esc} are the carrier capture and escape rates in and from a dot, respectively. The carrier capture rate is given by $R_{\mathrm{cap}} = Cn^2 + Bn$, where C is the carrier–carrier scattering coefficient (Auger capture coefficient) and B is the carrier–phonon scattering coefficient. These rates correspond to the carrier–carrier scattering rates defined in (8.53)–(8.57), however the rates for electrons and holes are assumed to be the same in (8.59). In the five-variable model, these parameters are the functions of the carrier densities in the wetting layer. In spite of a rough picture of the model, the fundamental dynamics and the trends of the laser oscillations can be explained to some extent. The model is

Table 8.6 Characteristic device parameters for quantum-dot semiconductor lasers with three-variable model at an oscillation wavelength of 1.30 μm

Symbol	Parameter	Value
g_0	gain coefficient	$1.8 \times 10^{-11}\ \mathrm{m^3 s^{-1}}$
ϑ	conversion coefficient	$2.4 \times 10^{22}\ \mathrm{m^{-3}}$
N_d	total carrier density	$2 \times 10^{15}\ \mathrm{m^{-2}}$
d_d	thickness of dot	10 nm
α	linewidth enhancement factor	1.2
r_0	facet reflectivity	0.565
τ_{ph}	photon lifetime	3 ps
τ_d	carrier lifetime in dot	1 ns
τ_s	carrier lifetime in well	1 ns
τ_{in}	round-trip time in laser cavity	8 ps
Γ	confinement factor	0.06
R_{cap}	carrier capture rate	$10^{11}\ \mathrm{s^{-1}}$
R_{esc}	carrier escape rate	$1.25 \times 10^{10}\ \mathrm{s^{-1}}$

particularly useful for the primary study of the steady-state behaviors in quantum-dot semiconductor lasers. The values of the parameters used in this model are listed in Table 8.6.

8.6.2 Quantum-Dot Semiconductor Lasers in Solitary Oscillations

We here discuss some characteristics of quantum-dot semiconductor lasers at solitary oscillation based on the five-variable model. The scattering rates are not constant but they depend on the carrier densities in the quantum-well wetting layer. They are calculated from microscopic Auger in- and out-scatterings. The calculation is not straightforward and they are not given by analytical forms. Therefore, we here only show examples of numerical results for the scattering rates. Figure 8.42 shows the scattering rates of electrons and holes for the carrier densities in the wetting layer at the ground state energy difference for electron of $\Delta E_e = 190$ meV and the ground state energy difference for hole $\Delta E_h = 69$ meV. We can see the strong dependence of the scattering rates on the carrier densities in the wetting layer. Figure 8.43a shows the steady-state occupation probabilities of carriers in a dot as a function of the bias injection current under the same condition of Fig. 8.42. For a low bias injection current in Fig. 8.43a, the difference of occupations of electron and hole is large, but it becomes small for the increase of the bias injection current and stays constant values. On the other hand, the difference of the carrier densities in the wetting layer is rather small for the all range of the bias injection current as shown in Fig. 8.43b. Thus, the

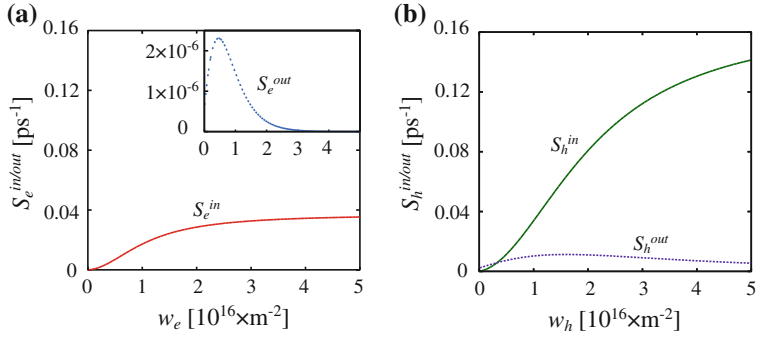

Fig. 8.42 Carrier–carrier scattering rates of **a** electrons (S_e^{in} and S_e^{out}) and **b** holes (S_h^{in} and S_h^{out}) for the carrier densities in the wetting layer at $\Delta E_e = 190\,\text{meV}$ and $\Delta E_h = 69\,\text{meV}$. *Solid lines* capture rates. *Dotted lines* escape rates

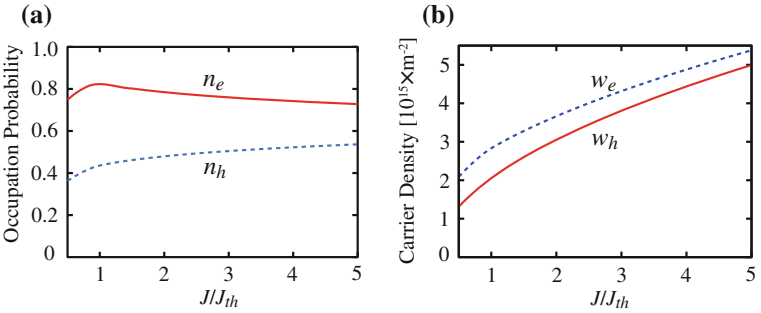

Fig. 8.43 **a** Steady-state occupation probabilities of carriers in a dot for the bias injection current. **b** Steady-state carrier densities in the quantum-well wetting layer for the bias injection current. *Solid lines* electrons. *Dotted lines* holes

difference of the occupation probabilities between electrons and holes in quantum dots plays a crucial role in the dynamics of quantum-dot semiconductor lasers.

The damping rate for a step response of the laser output for the bias injection current in quantum-dot semiconductor lasers is very high compared with that of quantum-well lasers. The fact is confirmed experimentally and theoretically. Figure 8.44 shows a comparison of experimental and simulation results for some fundamental characteristics in a quantum-dot semiconductor laser (Lüdge and Schöll 2009). Figure 8.44a is a turn-on transients at the bias injection currents of $2.2J_{\text{th}}$ and $2.7J_{\text{th}}$. The symbol of stars corresponds to the experimental and the simulation results are obtained from the five-variable model in (8.53)–(8.57). We can see fast decays of the relaxation oscillations. Figure 8.44b–d are the frequency of the relaxation oscillation ν_R, the width of the first relaxation oscillation peak Δt_{FWHM}, and the turn-on delay τ_{delay} for the variation of the bias injection current.

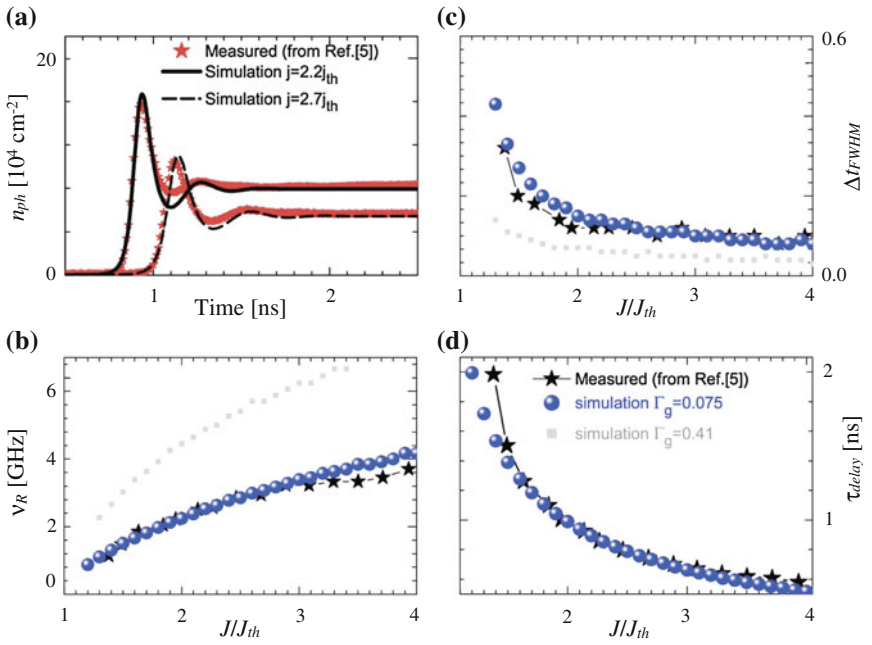

Fig. 8.44 Characteristics of a quantum-dot semiconductor laser. **a** Step response of the bias injection currents at $2.2J_{\text{th}}$ and $2.7J_{\text{th}}$. Stars are the experimental results. **b** Frequency of the relaxation oscillation for the bias injection current. Stars are the experimental results and dots are the simulated results. **c** Width of the first relaxation oscillation peak. **d** Turn-on delay time. Γ_g is the geometric confinement factor, which is related to the confinement factor as $\Gamma = \Gamma_g N^{\text{QD}}/N^{\text{sum}}$ [after Lüdge and Schöll (2009); © 2009 IEEE]

The microscopic five-variable model well reproduces the experimental results. Except for the fast damping rate in Fig. 8.44a, the other characteristics are compatible with those for quantum-well semiconductor lasers.

8.6.3 Optical Feedback Effects in Quantum-Dot Semiconductor Lasers

Since quantum-dot semiconductor laser has a fast damping rate as discussed in the previous subsection, it is robust for external perturbations such as optical feedback and optical injection. The optical feedback effects in quantum-dot semiconductor lasers have been studied theoretically and experimentally (O'Brien et al. 2004; Huyet et al. 2004; Viktorov et al. 2006; Otto et al. 2010). For example, the field equation with optical feedback in the microscopic model is written as

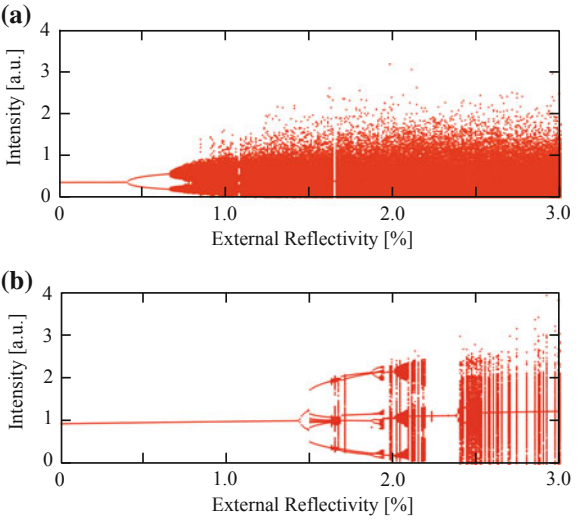

Fig. 8.45 Chaotic bifurcation diagrams induced by optical feedback. Bifurcation diagrams for **a** quantum-well and **b** quantum-dot semiconductor lasers. The length of the external reflector is $L = 30\,\mathrm{cm}$ and the bias injection current is set to $J = 1.5 J_{\mathrm{th}}$

$$\frac{\mathrm{d}E(t)}{\mathrm{d}t} = \frac{1}{2}(1 - i\alpha)\left[\Gamma W A\{n_e(t) + n_h(t) - N^{\mathrm{QD}}\} - \frac{1}{\tau_{\mathrm{ph}}}\right]E(t) + \frac{\kappa}{\tau_{\mathrm{in}}}E(t-\tau)\exp(i\omega_0\tau) \tag{8.61}$$

and the other four equations of the carrier densities in quantum-well and quantum-dot layers remain the same as (8.53)–(8.57). Similar to the dynamics of quantum-well semiconductor lasers, LFFs and fast chaotic oscillations are observed depending on the length of an external reflector, the external reflectivity, and the bias injection current. However, we need a larger external feedback power to destabilize the laser compared with quantum-well semiconductor lasers. Figure 8.45 shows examples of chaotic bifurcation diagrams induced by optical feedback for quantum-well and quantum-dot semiconductor lasers. Since the device structure and the parameters are different for the two lasers, it is difficult to perform completely direct comparisons of the dynamics. However, the device parameters are carefully chosen to compare the characteristics. The bifurcation diagram for the quantum-dot semiconductor laser is calculated from the microscopic five-variable model. From the figures, we can conclude that the quantum-dot semiconductor laser is less sensitive to optical feedback and we need much higher feedback power to destabilize the laser.

8.6.4 Optical Injection Effects in Quantum-Dot Semiconductor Lasers

Quantum-dot semiconductor laser has a high damping rate and a small α parameter. This high damping and small α parameter have been cited as the principal reason for the increased stability of such devices when subject to optical feedback, optical injection, and mutual coupling configurations. Therefore, it behaves like a class A laser rather than a class B laser for an optical injection (Goulding et al. 2007; Erneux et al. 2010). A typical feature of optical injection to a class B laser with nonzero α parameter is an asymmetric shape of the stable injection-locking region in the phase-space map of the optical injection and the frequency detuning as shown in Fig. 6.6. While, a class A laser such as He-Ne laser with visible oscillation shows a symmetric shape of the stable injection-locking region. Quantum-dot semiconductor laser with optical injection shows similar dynamics to a class A laser as for optical injection, however, various dynamics can be found at the boundaries of the stable optical injection-locking region. One of typical characteristics of quantum-dot semiconductor lasers is a pulsation oscillation like the axon of the giant Atlantic squid when perturbed above certain threshold level. The pulses are evidence of a large excursion in the phase space of the system. Indeed, for optical injection, quantum-dot semiconductor laser shows single pulses and double excitable pulses at one boundary of the stable injection-locking region at high injection strength with finite frequency detuning. Theoretical considerations show that these pulses are related to a saddle-node bifurcation on a limit cycle as in the Adler equation.

Figure 8.46 shows the boundaries of the stable optical injection-locking region in quantum-dot semiconductor laser (Erneux et al. 2010). Figure 8.46a is an experimental result of the phase diagram for a DFB quantum dot semiconductor laser of an oscillation wavelength of 1.30 μm. The bias injection current is set to $1.5J_{\text{th}}$. The solid lines in Fig. 8.46 are the boundary of saddle-node (SN) bifurcations, and the dashed lines are that of Hopf (H) bifurcations. The inside of the lines are the stable injection-locking region. Various dynamics are observed, but the one of different features of injection locking from those of conventional quantum-well semiconductor lasers is rather a symmetrical shape of the injection-locking region and the domain of bistable operation, in which coexistence of two stable locking states exists. The Hopf bifurcation line differs from that which occurs for an injected quantum-well semiconductor lasers and, in particular, it does not cross the zero detuning line as shown in the inset in Fig. 8.46a. The phase diagram is not similar to that of ordinary class B laser, but similar to that of class A laser. More precisely, quantum-dot semiconductor lasers exhibit both Class A and Class B dynamics, depending on the carrier capture parameters by analyzing a following three-variable rate-equation model.

To investigate optical-injection dynamics, the following field equation of the three-variable model is employed:

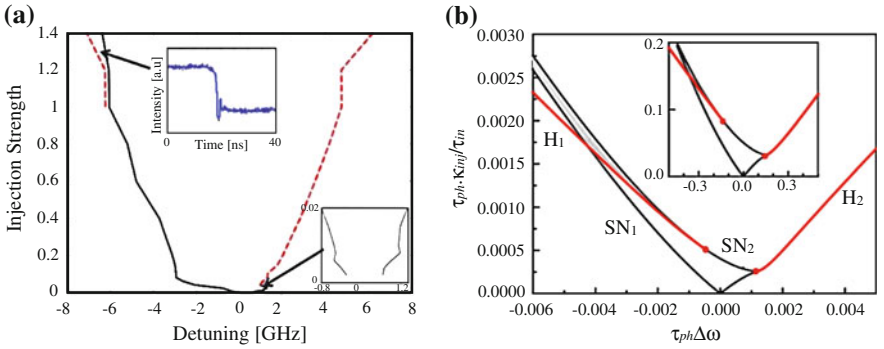

Fig. 8.46 **a** Experimental stability diagram in the phase space of frequency detuning and injection strength (intensity). The lines are the stability boundary for optical injection. *Solid line* saddle-node bifurcation boundary, and *dashed line* Hopf bifurcation boundary. *Upper inset* switching between two locked states with different intensities, and *lower inset* zoom of the region of low injection strength where the locking is via a saddle-node bifurcation for both signs of the detuning. **b** Analytic stability diagram calculated from three-variable model at $J = 1.2J_{\text{th}}$, a=1.2, and τ_{ph} =2 ps. *SN* saddle-node bifurcation point, *H* Hopf bifurcation point. The shaded region denotes the domain of steady-state bistability. The dots are fold-Hopf points where Hopf and SN bifurcation lines merge. The inset shows the stability diagram for an injected class A laser [after Erneux et al. (2010); © 2010 OSA]

$$\frac{\mathrm{d}E(t)}{\mathrm{d}t} = \frac{1}{2}(1 - i\alpha)\left[g_0\vartheta\{2\rho(t) - 1\} - \frac{1}{\tau_{\text{ph}}}\right]E(t) + \frac{\kappa_{\text{inj}}}{\tau_{\text{in}}}E_m(t)\exp(-i\,\Delta\omega t) \tag{8.62}$$

The other two equations are the same as (8.59) and (8.60). Figure 8.46b shows the phase diagram theoretically calculated from the three-variable model. The dots are fold-Hopf points where Hopf and SN bifurcation lines merge. The shaded region denotes the domain of steady-state bistability, which is compatible with the experiment. At higher injection levels and for positive detuning, the locking is via a Hopf bifurcation (H_2), and there is no SN bifurcation. For negative detunings, there is a domain of bistability between two locked states, because of a Hopf bifurcation that stabilizes the lower intensity branch (H_1). The dynamics is fairly similar to those of an injected class A laser, which is shown in the inset in Fig. 8.46b. The general trends of optical-injection dynamics in Fig. 8.46b are well coincident with those of the experiment in Fig. 8.46a.

8.7 Quantum-Cascade Semiconductor Lasers

8.7.1 Quantum-Cascade Semiconductor Lasers

Different from conventional quantum-well semiconductor laser, which uses optical transitions between conduction and valence bands (inter-band), semiconductor laser that is based on inter-subbanad optical transitions within conduction band has been developed (Faist et al. 1994; Gmachl et al. 2001; Wójcik et al. 2011a,b; Scalari et al. 2009). The laser has several stages of cascades consisting of superlattice structures and is called quantum-cascade semiconductor laser (QCL). The light emission of this laser is based on inter-subband optical transitions, therefore the carrier related to laser radiation is only electron. Quantum-cascade lasers emit THz light from mid-infrared (wavelength of several μm) to far-infrared (several hundreds μm) oscillations either at pulse or CW operations. However, it is difficult to obtain a laser from an oscillation wavelength between $30 \sim 60\,\mu$m, since the energy in this region corresponds to that of longitudinal optical phonon (LO phonon). In a long optical wavelength, cooling for the device is essential, however, a laser (GaInAs/AlInAs/InP quantum-cascade laser) operating at room temperature is reported. Quantum-cascade semiconductor laser can emit high power as much as 1 W and has a narrow oscillation linewidth as small as 150 kHz, while conventional quantum-well semiconductor laser has a linewidth around 10 MHz. Quantum-cascade lasers are of great interest, since they can be used for detection of toxic chemicals and gases by mid-infrared spectroscopy. Their narrow linewidths make them attractive in coherent applications, such as free-space short-range communications due to the Wi-Fi capabilities of terahertz waves and large supposed bandwidth modulation. Also their large direct intensity modulation bandwidth is attractive for optical communication systems. Some of different characteristics of quantum-cascade semiconductor lasers from conventional quantum-well semiconductor lasers are listed in Table 8.7. The main difference concerning the laser dynamics is a short relaxation time of carriers due to the use of inter-subband optical transitions.

Figure 8.47 shows a schematic model of the band structure in a quantum-cascade semiconductor laser. The laser consists of a multi-stage quantum cascade. In the figure, a single period is drawn. A single photon is emitted by the transition in the subbands when an electron passes through each quantum cascade. Each stage consists of the active region and the injection region. The electron that is once emitted photon is reused in the next stage, therefore, the external quantum efficiency is very high and the laser power is proportional to the number of the stages. In actual, each region consists of several layers of quantum-well structures. For optical transitions, the laser is described by a two-level model, however four energy levels are related to the light emission as shown in the figure. A carrier is injected from the injection region and goes through a tunnel barrier 4. The injected carrier at the level 3 emits a photon and transitions to the level 2. The carrier is pulled out form the level 2 to the ground state 1 by the fast sub picosecond time relaxation process. This carrier is again injected to the next stage. Several stages, usually several to more that ten stages, are piled up along

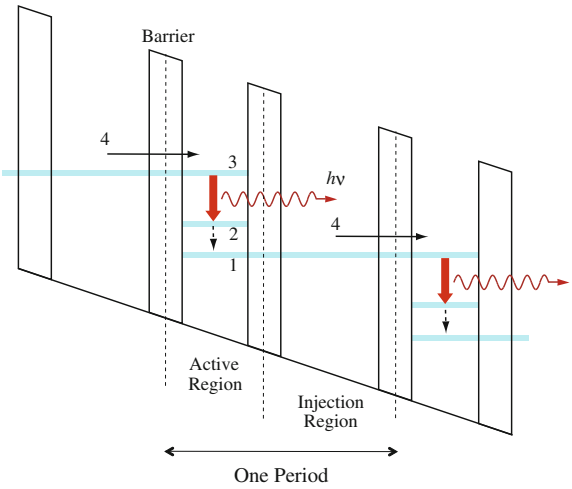

Fig. 8.47 Schematic model of a quantum-cascade laser using an inter-subband four-level active medium. Each stage consists of active and injection regions. *4* Injector, *3* upper level of laser emission, *2* lower level of laser emission, and *1* ground state

Table 8.7 Difference of characteristics between conventional quantum-well semiconductor lasers (QWLs) and quantum-cascade semiconductor lasers (QCLs)

	QWLs	QCLs
Optical transitions	interband	inter-subband
Carriers	electrons and holes	electrons
α parameter	large	small
Oscillation linewidth	broad (∼10 MHz)	narrow (∼100 kHz)
Polarization mode	TE	TM
Output power	proportional to injection current	proportional to injection current and number of cascades
Stripe width*	few μm	larger than 10 μm
Thickness of active region*	less than 1 μm	larger than 10 μm
Relaxation time of carrier	∼1 ns	∼1 ps

* Note that the size of QCL is strongly dependent on the emission wavelength

the direction perpendicular to the substrate and, thus, forming quantum cascades. The emission wavelength is easily controlled by designing the thicknesses of the active and injection regions and also the inside quantum-well layers, even for the same material, which is quite different from conventional quantum-well semiconductor lasers. Indeed, the design of the subband ranging from several tens to 100 meV is possible for the same materials and we can obtain a quantum-cascade semiconductor laser with a desired optical wavelength.

8.7.2 Linewidth Enhancement Factor of Quantum-Cascade Semiconductor Lasers

In conventional diode lasers, the linewidth enhancement factor (α factor) is typically $3 \sim 7$, and arises because the conduction and valence bands involved in the laser transition have opposite curvature in k-space, resulting in a spectrally asymmetric differential gain. In contrast, both laser subbands of a quantum-cascade semiconductor laser are within the conduction band, and exhibit the same reciprocal space curvature. It has thus been predicted that the lasers should display a symmetric differential gain and a zero α factor. However, it is not true for real quantum-cascade semiconductor lasers for several reasons and the lasers usually have small but nonzero value of the linewidth enhancement factor. Therefore, the lasers behave like not class B lasers as dynamic characteristics but rather class A lasers. There are several methods to measure a linewidth enhancement factor in a semiconductor laser and the same techniques can be also applied to measure the parameter in a quantum-cascade semiconductor laser. Among them, the measurement using self-mixing effect in semiconductor laser is a promising one due to the lack of compact and sensitive detectors in the THz band (Staden et al. 2006; Green et al. 2008; Lim et al. 2011). The method of self-mixing in semiconductor lasers is well studied in quantum-well semiconductor lasers and applications including the measurement of linewidth enhancement factor are discussed in Chap. 11.

Figure 8.48 shows an example of the measurements of linewidth enhancement factor using self-mixing effects in quantum-cascade semiconductor lasers (Staden et al. 2006). The laser is a DFB quantum-cascade laser of an internal cavity length of L= 1 mm, a width of the active region of $w = 10\,\mu$m, and an oscillation wavelength of $\lambda = 5.45\,\mu$m. The laser is cooled and its threshold current is 115 mA at 82 K. The linewidth enhancement factor has a value close to zero near the threshold, however, it varies largely depending on the bias injection current and has a large value at higher injection current. This is a remarkable difference with respect to near-infrared interband semiconductor lasers, for which α is expected to be approximately constant. One of possible reasons for this increase could be the detuning effect of the resonator mode with respect to the gain curve. It is known that for interband semiconductor lasers a relative red-shift of the resonator mode with respect to the gain peak results in an increase of the linweidth enhancement factor (α factor). For quantum-cascade semiconductor lasers, an increase of temperature as well as an increase of injection current results in a red-shift of the gain spectrum. Further, a steady-state analysis based on the rate equations discussed in the next subsection, the carrier densities of the upper and lower laser levels both increase above threshold with increasing injection current, even though the difference of both densities above threshold remains constant, accounting for gain clamping. This behavior follows from the rate equations for quantum-cascade semiconductor lasers and is depicted in the inset of the figure. It is in contrast to inter-band semiconductor lasers, where the carrier density is pinned above threshold. The monotonic increase of the carrier density certainly influences the material susceptibility, and thus it alters the

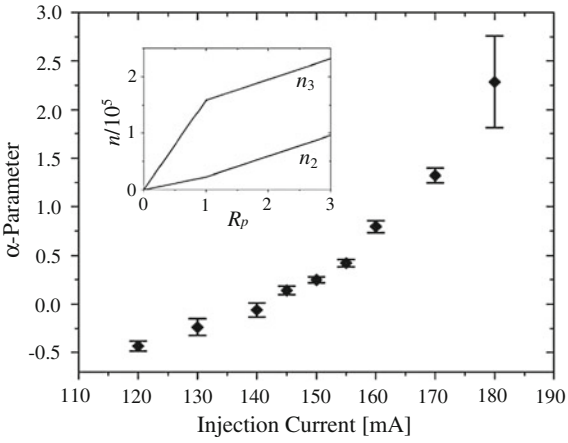

Fig. 8.48 α parameter as a function of the injection current. The inset shows the dependence of the carrier population of the upper and lower levels on the pump parameter $R_p = J/J_{\text{th}}$ [after Staden et al. (2006); © 2006 OSA]

linewidth enhancement factor. As another example, (Green et al. 2008) measured the linewidth enhancement factor for a quantum-cascade semiconductor laser of an optical wavelength of $\lambda = 116\,\mu\text{m}$. They obtained the linewidth enhancement factor from 0.2 to 0.5 depending on the bias current ranging form J to $2J_{\text{th}}$. The variation is small but it still depends on the bias injection current.

8.7.3 Rate Equations of Quantum Cascade Semiconductor Lasers

A quantum-cascade laser consists of a large number of layers constituting active and injector regions. An accurate design requires a large number of rate equations (Donovan et al. 2001). However, it is not convenient to treat them for the visualization of interplay between various parameters. Therefore, to obtain a reduced set of equations, we here consider a two-level lasing quantum well together with a lifetime describing carrier removal. As a result, the model of a quantum-cascade laser of N_p periods, are written by the following simple rate equations (Haldar 2005; Petitjean et al. 2011; Meng and Wang 2012):

$$\frac{\mathrm{d}S(t)}{\mathrm{d}t} = N_p G\{n_3(t) - n_2(t)\}S(t) - \frac{S(t)}{\tau_{\text{ph}}} + \beta\frac{n_3(t)}{\tau_{\text{sp}}} \tag{8.63}$$

$$\frac{\mathrm{d}n_3(t)}{\mathrm{d}t} = \frac{J}{ed} - \frac{n_3(t)}{\tau_3} - G\{n_3(t) - n_2(t)\}S(t) \tag{8.64}$$

$$\frac{\mathrm{d}n_2(t)}{\mathrm{d}t} = \frac{n_3(t)}{\tau_{32}} - \frac{n_2(t)}{\tau_2} + G\{n_3(t) - n_2(t)\}S(t) \tag{8.65}$$

S is the photon number, n_3 is the carrier density at energy level 3, and n_2 is the carrier density at energy level 2. Here, G is the gain coefficient, τ_{ph} is the photon lifetime, τ_{sp} is the spontaneous relaxation time, τ_3 is the electron lifetime at level 3, τ_{32} the phonon scattering time from level 3 to 2, τ_2 is the electron lifetime at level 2, β is the spontaneous emission factor. It is easily derived from the steady-state analysis that the laser oscillation is attained when the condition of $\tau_{32} > \tau_2$ is satisfied. Table 8.8 lists some parameter values used for numerical calculations in the above equations (Petitjean et al. 2011).

One of the characteristics related to the dynamics in quantum-cascade semiconductor laser is a very short carrier lifetime, by which the laser shows significant differences in comparison with conventional semiconductor lasers based on interband optical transitions. Due to fast carrier decay rate, the laser has a small damping characteristic for a step response and behaves like class A lasers. Figure 8.49 shows a small signal response of a quantum-cascade laser calculated from the above three equations (Meng and Wang 2012). In an interband semiconductor laser, the modulation bandwidth is simply determined by the relaxation oscillation time and the oscillation frequency is increased as the square root of the optical power. Thus, in common semiconductor lasers, the relaxation oscillation frequency is usually several to ten GHz within the operation injection current range. However, a high modulation characteristic is obtained in a quantum-cascade semiconductor laser as shown in Fig. 8.49. For the bias injection current of $J = 4J_{th}$, the 3-dB cutoff frequency of 21 GHz is obtained. Further, resonance peak, which is usually observed close to the cutoff frequency in conventional semiconductor lasers, is not visible in the responses. The 3-dB optical bandwidth increases with optical power, but unlike that for interband lasers, it initially increases approximately linearly with optical power, not as the square root of the optical power. To explain the detailed dynamics of quantum-cascade semiconductor lasers, the extraction time of the electrons to pass through the different periods should be taken into account (Rana and Ram 2002; Gensty and Elsäßer 2005; Petitjean et al. 2011). To account the extraction time of the electrons to pass from the fundamental level of a certain period to the excited one of the next period, one more equation has to be reintegrated. The rate equations are consequently based on a three-level scheme with four equations (one for each of the three levels of the electrons and one for the photons).

8.7.4 Nonlinear Interactions in Quantum-Cascade Semiconductor Lasers

Nonlinear phase coupling of laser modes in quantum-cascade semiconductor lasers leads to a variety of ultrafast and coherent phenomena; synchronization of transverse modes, beam steering, multimode instability, and generation of mode-locked ultrashort pulses. The inhomogeneous saturation leads to spectral and spatial hole burning, which, in turn, gives rise to multimode operation and nonlinear coupling between

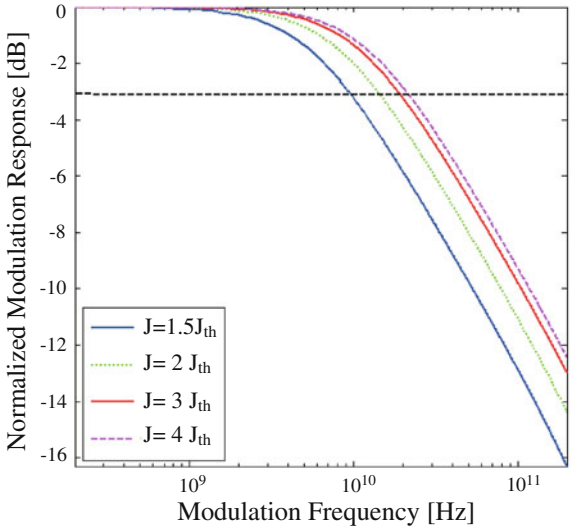

Fig. 8.49 Numerical example of small signal response in a quantum-cascade laser at $\lambda = 9\mu\text{m}$, $N_p = 40$, $\tau_{\text{ph}} = 9.91$ ps and $\tau_3 = 0.66$ ps [after Meng and Wang (2012); © 2012 OSA]

laser modes. This nonlinear coupling is phase sensitive and under certain conditions may lead to frequency and phase locking of laser modes. To discuss coherent interplays in quantum-cascade semiconductor lasers, the equation for the field is necessary instead of the photon number equation in the preceding subsection. For the purpose of explaining nonlinear phase coupling in multimode quantum-cascade semiconductor lasers, the coherent rate-equation model based on the two-level Maxwell-Bloch equations are derived (Wójcik et al. 2010, 2011a,b). The derivation is almost equal to that derived in Chap. 2.

The electron flow through the typical active region of a quantum-cascade semiconductor laser can be roughly approximated by a four-level laser scheme. The four-level scheme can be further reduced to the effective two-level scheme if we take into account that the scattering time from lower laser level 3 to level 2 in Fig. 8.47 is very short (∼0.2 ps) due to resonant LO-phonon emission. Therefore, level 3 stays almost empty and we can neglect its population. Then one can write the equation for the population inversion $W = n_3 - n_2$ between laser levels 3 and 2. The total field is expanded by the eigenfunction of the x and y coordinates $\psi(\mathbf{r}_\perp)(\mathbf{r}_\perp = (x, y))$ as

$$E_{\text{total}}(\mathbf{r}, t) = \sum_i E_i(z, t)\psi_i(\mathbf{r}_\perp) \tag{8.66}$$

where ψ_i is the eigenfunction for the ith mode. Then, the rate equations for the field component E_i, the polarization P and the population inversion W are given by

Table 8.8 Characteristic device parameters for quantum-cascade semiconductor lasers at an oscillation wavelength of 103 μm

Symbol	Parameter	Value
ν	frequency	2.9 THz
N_p	number of period	30
Γ	confinement factor	0.27
w	cavity width	80 μm
L	cavity length	3.0 mm
r^2	facet reflectivity	0.29
η_g	mode-group index	3.3
α_i	cavity loss	$2.4 \times 10^{-3}\,\mathrm{m}^{-1}$
G	gain coefficient	$6.75 \times 10^{-9}\,\mathrm{m}^3\mathrm{s}^{-1}$
I_{th}	threshold current	200 mA
β	spontaneous emission factor	1×10^{-5}
τ_2	electron lifetime at level 2	0.3 ps
τ_3	electron lifetime at level 3	1.1 ps
τ_{31}	phonon scattering time 3→1	2.4 ps
τ_{32}	phonon scattering time 3→2	2.0 ps
τ_{ph}	photon lifetime	3.7 ps
τ_{sp}	spontaneous relaxation time	7.0 ns

$$\frac{\partial E_i(z,\,t)}{\partial t} + \frac{c}{\eta_i}\frac{\partial E_i(z,\,t)}{\partial z} + (\alpha_i + i\delta_i)E_i(z,\,t) = i\frac{4\pi\omega_0}{\eta_i\sigma}\int_{\mathrm{ar}} P(z,\,t)\psi_i(\mathbf{r}_\perp)\mathrm{d}V \tag{8.67}$$

$$\frac{\partial P(z,\,t)}{\partial t} + \gamma_\perp P(z,\,t) = \frac{iN_A\mu^2}{2\hbar}W(z,\,t)\sum_i E_i(z,\,t)\psi_i(\mathbf{r}_\perp) \tag{8.68}$$

$$\frac{\partial W(z,\,t)}{\partial t} + \gamma_{||}\{W(z,\,t) - W_p\} = \frac{i}{\hbar N_A}\sum_i \{E_i^*(z,\,t)P(z,\,t) - E_i(z,\,t)P^*(z,\,t)\} \tag{8.69}$$

where $\gamma_\perp$ is the longitudinal relaxation coefficient, $\gamma_{||}$ is the transverse relaxation coefficient, N_A is the density of atoms in the unit volume, μ is the dipole moment of the laser transition, W_p is the pump, η_i is the modal refractive index, α_i is the modal loss, $\delta_i = \omega_i - \omega_0$ is the detuning of the ith mode (ω_i) from the central frequency (ω_0), and σ is the cross section of the waveguide. The integration in (8.67) is taken over the active region.

The fast relaxation times for population inversion, $\gamma_{||}^{-1} \sim 1$ ps, and polarization, $\gamma_\perp^{-1} \sim 0.1$ ps, characteristic of quantum-cascade semiconductor lasers allow us to adiabatically eliminate both variables. This remarkable stability of the transverse mode locking is the consequence of another peculiar feature of the lasers;

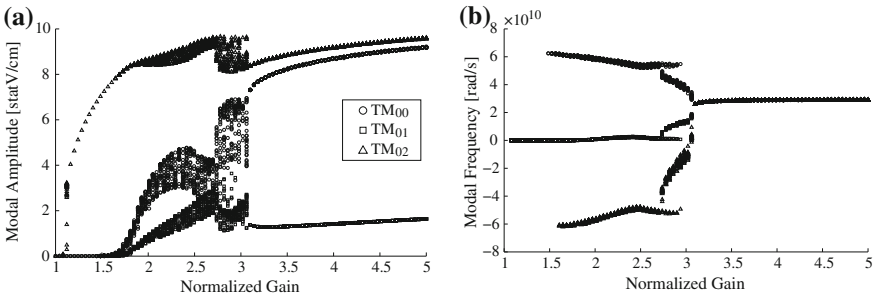

Fig. 8.50 Stable steady-state solutions for three TM modes (TM_{00}, TM_{01}, and TM_{02}) as the function of the linear gain normalized to the threshold gain for the TM_{02} mode. **a** Modal amplitudes and **b** modal frequencies [after Wójcik et al. (2010); © 2010 SPIE]

ultrafast gain recovery time of the order of 1 ps. This timescale is much shorter than the cavity roundtrip time and the photon lifetime, which makes the laser a class A laser. Ultrafast gain recovery time leads to overdamped relaxation oscillations as discussed in the previous subsection, which stabilizes phase locking, as compared to class B lasers where phase locking of transverse modes is more difficult to achieve because of prominent relaxation oscillation resonance. In common semiconductor lasers, phase locking is primarily due to density modulation of free carriers, which is proportional to the linewidth enhancement factor α. In quantum-cascade lasers, the total electron density is not affected by the laser field and the linweidth enhancement factor is much smaller. In this case, the mode coupling is due to gain saturation across an inter-subband atomic-like laser transition and the concomitant strong spatial hole-burning, which favors multimode operation. Figure 8.50 shows an example of nonlinear phase couplings in quantum-cascade semiconductor lasers. The laser is operated with three TM modes (TM_{00}, TM_{01}, and TM_{02}), which are assumed in coincident with a real experiment. Figure 8.50a, b are the amplitude and frequencies of all stable steady-state solutions, respectively (only the field equation is taken into account). The frequency of each mode in Fig. 8.50 is defined as a derivative of the total phase; it is constant when the steady state is reached. The simulations reveal the existence of a certain critical current above which there is only one stable steady-state solution. A remarkable feature of this solution is that frequencies of all modes are locked to the same frequency. Below this critical current, there are multiple steady-state solutions with different uncorrelated frequencies and phases. The model can well explain coherent interplays in real quantum-cascade semiconductor lasers with multimode oscillations.

8.7.5 *Effects of Optical Feedback in Quantum-Cascade Semiconductor Lasers*

For coherent effects of optical feedback and optical injection in quantum-cascade semiconductor lasers, a similar equation for the complex field E as those discussed in the pervious sections can be employed instead of the photon number equation in (8.63).

$$\frac{\mathrm{d}E(t)}{\mathrm{d}t} = \frac{1}{2}(1 - i\alpha)\left[N_p G\{n_3(t) - n_2(t)\} - \frac{1}{\tau_{\mathrm{ph}}}\right]E(t) \tag{8.70}$$

Quantum-cascade semiconductor lasers still have non-zero value of the α parameter. Optical feedback or optical injection term is added to the right hind side of the equation in (8.70) when necessary. The carrier density equations remain the same as (8.64) and (8.65). Room temperature quantum-cascade semiconductor lasers are an attractive solution for trace gas sensing applications that require fast, portable, high sensitivity measurements such as environmental monitoring and medical diagnostics. Therefore, the study of optical feedback effects in quantum-cascade semiconductor lasers is important, since the coherence of the lasers is high (the oscillation linewidth is as small as ∼100 kHz) and an isolator in this wavelength region is not available. Nevertheless, a little study for the dynamics of quantum-cascade semiconductor lasers with optical feedback has been conducted (Hugi et al. 2010). One of the reasons for lacking the study is that the lasers behave like class A lasers and we need much larger optical feedback to induce instabilities such as chaos in comparison with conventional semiconductor lasers. Therefore, we here only remark some aspects of the current study of the optical feedback effects. As the study for the optical feedback from plain mirror and grating mirror, the effects for the linewidth narrowing, spectroscopic characteristics of laser oscillations, and RIN enhancement and reduction have been reported (Luo et al. 2001; Totschnig et al. 2002; Petitjean et al. 2011). The dynamic phenomena correspond to those of small optical feedback effects in interband quantum-well semiconductor lasers. Also, the effect of optical injection in quantum-cascade semiconductor lasers is an interesting issue left for the future study.

References

Acachihara H, Hess O, Abraham E (1993) Spatiotemporal chaos in broad-area semiconductor lasers. J Opt Soc Am B 10:658–665

Agrawal GP, Dutta NK (1993) Semiconductor lasers. Van Nostrand Reinhold, New York

Ahamed M, Yamada M (2002) Influence of instantaneous mode competition on the dynamics of semiconductor lasers. IEEE J Quantum Electron 38:682–693

Altés JB, Gatare I, Panajotov K, Thienpont H, Sciamanna M (2006) Mapping of the dynamics induced by orthogonal optical injection in vertical-cavity surface-emitting lasers. IEEE J Quantum Electron 42:198–207

Aoyama H, Tomida S, Shogenji R, Ohtsubo J (2011) Chaos dynamics in vertical-cavity surface-emitting semiconductor lasers with polarization-selected optical feedback. Opt Commun 284:1405–1411

Arteaga MA, Unold HJ, Ostermann JM, Michalzik R, Thienpont H, Panajotov K (2006) Investigation of polarization properties of VCSELs subject to optical feedback from an extremely short external cavity—part II: experiments. IEEE J Quantum Electron 42:102–107

Asatuma T, Takiguchi Y, Frederico S, Furukawa A, Hirata S (2006) Successive phase change and stability of near-field patterns for broad-area laser diodes. SPIE Proc 6104:61040C

Barchanski A, Gensty T, Degen C, Fischer I, Elsäßer W (2003) Picosecond emission dynamics of vertical-cavity surface-emitting lasers: spatial, spectral, and polarization-resolved characterization. IEEE J Quantum Electron 39:850–858

Besnard P, Robert F, Charès ML, Stéphan GM (1997) Theoretical modeling of vertical-cavity surface-emitting lasers with polarized optical feedback. Phys Rev A 56:3191–3205

Besnard P, Charès ML, Stéphan G, Robert F (1999) Switching between polarized modes of a vertical-cavity surface-emitting laser by isotropic optical feedback. J Opt Soc Am B 16:1059–1064

Burkhard T, Ziegler MO, Fischer I, Elsäßer W (1999) Spatio-temporal dynamics of broad area semiconductor lasers and its characterization. Chaos, Solitons and Fractals 10:845–850

Carr TW, Erneux T (2001) Dimensionless rate equations and simple conditions for self-pulsing in laser diodes. IEEE J Quantum Electron 37:1171–1177

Danckaerta J, Naglera B, Alberta J, Panajotova K, Veretennicoff I, Erneux T (2002) Minimal rate equations describing polarization switching in vertical-cavity surface-emitting lasers. Opt Commun 201:129–137

Degen C, Fischer I, Elsäßer W (1999) Transverse modes in oxide confined VCSELs: influence of pump profile, spatial hole burning, and thermal effects. Opt Express 5:38–47

Diehl R (2000) High-power diode laser, fundamentals, technology, applications. Springer-Verlarg, Berlin

Donovan K, Harrison P, Kelsall RW (2001) Self-consistent solutions to the intersubband rate equations in quantum cascade lasers: analysis of a GaAs/$Al_xGa_{1-x}As$ device. J Appl Phys 89:3084–3090

Erneux T, Viktorov EA, Mandel P (2007) Time scales and relaxation dynamics in quantum-dot lasers. Phys Rev A 76:023819-1–7

Erneux T, Viktorov EA, Kelleher B, Goulding D, Hegarty SP, Huyet G (2010) Optically injected quantum-dot lasers. Opt Lett 35:937–939

Faist J, Capasso F, Sivco DL, Sirtori C, Hutchinson AL, Cho AY (1994) Quantum cascade laser. Science 264:553–556

Fischer I, Hess O, Elsäßer W, Göbel E (1996) Complex spatio-temporal dynamics in the near-field of broad-area semiconductor laser. EuroPhys Lett 35:579–584

Fujiwara N, Ohtsubo J (2004) Synchronization in chaotic vertical-cavity surface-emitting semiconductor lasers. SPIE Proc 5349:282–289

Fujiwara N, Takiguchi Y, Ohtsubo J (2003) Observation of low-frequency fluctuations in vertical-cavity surface-emitting lasers. Opt Lett 28:896–898

Fukushima T (2000) Analysis of resonator eigenmodes in symmetric quasistadium laser laser diodes. J Lightwave Technol 18:2208–2216

Fukushima T, Miyazaki H, Ando T, Tanaka T, Sakamoto T (2002) Nonlinear dynamics in directly modulated self-pulsating laser diodes with a highly doped saturable absorption layer. Jpn J Appl Phys 41 Part 1:117–124

Gaciu N, Gehrig E, Hess O (2007) Control of broad-area laser dynamics with delayed optical feedback. In: Schöll E, Schuster G (eds) Handbook of chaos control, Chap. 22. Wiley-VCH, Weinheim

Gatare I, Sciamanna M, Buesa J, Thienpont H, Panajotov K (2006) Nonlinear dynamics accompanying polarization switching in vertical-cavity surface-emitting lasers with orthogonal optical injection. Appl Phys Lett 88:101106-1–3

Gehrig E, Hess O (2003) Spatio-temporal dynamics and quantum fluctuations in semiconductor lasers. Springer-Verlag, Heidelberg

Gensty T, Elsäßer W (2005) Semiclassical model for the relative intensity noise of intersubband quantum cascade lasers. Opt Commun 256:171–183

Giudici M, Balle S, Ackemann T, Barland S, Tredicce JR (1999) Polarization dynamics in vertical-cavity surface-emitting lasers with optical feedback: experiment and model. J Opt Soc Am B 16:2114–2123

Gmachl C, Capasso F, Sivco DL, Cho AY (2001) Recent progress in quantum cascade lasers and applications. Rep Prog Phys 64:1533–1601

Goulding D, Hegarty SP, Rasskazov O, Melnik S, Hartnett M, Greene G, McInerney JG, Rachinskii D, Huyet1 G (2007) Excitability in a quantum dot semiconductor laser with optical injection. Phys Rev Lett 98:153903-1–4

Green RP, Xu JH, Mahler L, Tredicucci A, Beltram F, Giuliani G, Beere HE, Ritchie DA (2008) Linewidth enhancement factor of terahertz quantum cascade lasers. Appl Phys Lett 92:071106-1–3

Grillot F, Veselinov K, Gioannini M, Montrosset I, Even J, Piron R, Homeyer E, Loualiche S (2009) Spectral analysis of 1.55-μm InAs-InP(113)B quantum-dot lasers based on a multipopulation rate equations model. IEEE J Quantum Electron 45:872–878

Haldar MK (2005) A simplified analysis of direct intensity modulation of quantum cascade lasers. IEEE J Quantum Electron 41:1349–1355

Hess O, Kuhn T (1996a) Maxwell-Bloch equations for spatially inhomogeneous semiconductor lasers I theoretical formulation. Phys Rev A 54:3347–3359

Hess O, Kuhn T (1996b) Maxwell-Bloch equations for spatially inhomogeneous semiconductor lasers II spatiotemporal dynamics. Phys Rev A 54:3360–3368

Hess O, Koch SW, Moloney JV (1995) Filamentation and beam propagation in broad-area semiconductor lasers. IEEE J Quantum Electron 31:35–43

Hodgson N, Weber H (1997) Optical resonators. Springer, London

Hong Y, Spencer PS, Shore KA (2004) Suppression of polarization switching in vertical-cavity surface-emitting lasers by use of optical feedback. Opt Lett 29:2151–2153

Hong Y, Ju R, Spencer PS, Shore KA (2005) Investigation of polarization bistability in vertical-cavity surface-emitting laser subjected to optical feedback. IEEE J Quantum Electron 41:619–624

Hugi A, Maulini R, Faist J (2010) External cavity quantum cascade laser. Semicond Sci Technol 25:083001-1–14

Hülsewede R, Sebastian J, Wenzel H, Beister G, Kanauer A, Erbert G (2001) Beam quality of high power 800 nm broad-area laser diodes with 1 and 2 mm large optical cavity structure. Opt Commun 192:69–75

Hurtado A, Quirce A, Valle A, Pesquera L, Adams MJ (2010) Nonlinear dynamics induced by parallel and orthogonal optical injection in 1550 nm vertical-cavity surface-emitting lasers (VCSELs). Opt Express 18:9423–9428

Huyet G, O'Brien D, Hegarty SP, McInerney JG, Uskov AV, Bimberg D, Ribbat C, Ustinov VM, Zhukov AE, Mikhrin SS, Kovsh AR, White JK, Hinzer K, SpringThorpe AJ (2004) Quantum dot semiconductor lasers with optical feedback. Phys Stat Sol (a) 201:345–352

Ikuma Y, Ohtsubo J (1998) Dynamics in a compound cavity semiconductor laser induced by small external-cavity-length change. IEEE J Quantum Electron 34:1240–1246

Jiang S, Pan Z, Dagenais M, Morgan RA, Kojima K (1993) High-frequency polarization self-modulation in vertical-cavity surface-emitting lasers. Appl Phys Lett 63:3545–3547

Jones RJ, Rees P, Spencer PS, Shore KA (2001) Chaos and synchronization of self-pulsating laser diodes. J Opt Soc Am B 18:166–172

Juang C, Chen MR, Juang J (1999) Nonlinear dynamics of self-pulsating laser diodes under external drive. Opt Lett 24:1346–1348

Juang C, Hwang TM, Juang J, Lin WW (2000) A synchronization scheme using self-pulsating laser diodes in optical chaotic communication. IEEE J Quantum Electron 36:300–304

Kuznetsov M, Tsang DZ, Walpole JN, Liau ZL, Ippen EP (1986) Chaotic pulsation of semiconductor lasers with proton-bombarded segment. In: Boyd RW, Raymer MG, Narducci LM (eds) Optical instabilities, Vol. 4. Cambridge University Press, Cambridge

Law JY, Agrawal GP (1997a) Effects of spatial hole burning on gain switching in vertical-cavity surface-emitting lasers. IEEE J Quantum Electron 33:462–468

Law JY, Agrawal GP (1997b) Mode-partition noise in vertical-cavity surface-emitting lasers. IEEE Photon Technol Lett 9:437–439

Law JY, Agrawal GP (1998) Feedback-induced chaos and intensity-noise enhancement in vertical-cavity surface-emitting lasers. J Opt Soc Am B 15:562–569

Levy G, Hardy AA (1997) Chaotic effects in flared lasers: a numerical analysis. IEEE J Quantum Electron 33:26–32

Li H, Iga K (2002) Vertical-cavity surface-emitting laser devices. Springer, Berlin

Li H, Lucas TL, McInerney JG, Wright MW, Morgan RA (1996) Injection locking dynamics of vertical cavity semiconductor lasers using conventional and phase conjugate injection. IEEE J Quantum Electron 32:22–235

Lim YL, Dean P, Nikolić M, Kliese R, Khanna SP, Lachab M, Valavanis A, Indjin D, Ikonić Z, Harrison P, Linfield EH, Davies AG, Wilson SJ, Rakić AD (2011) Demonstration of a self-mixing displacement sensor based on terahertz quantum cascade lasers. Appl Phys Lett 99:081108-1–3

Lüdge K (2011) Modeling quantum dot based laser devices. In: Lüdge K (ed) Nonlinear laser dynamics, Chap. 1. Wiley-VCH, Weinheim

Lüdge K, Schöll E (2009) Quantum-dot lasers-desynchronized nonlinear dynamics of electrons and holes. IEEE J Quantum Electron 45:1396–1401

Lüdge K, Bormann MJP, Malić E, Hövel P, Kuntz M, Bimberg D, Knorr A, Schöll E (2008) Turn-on dynamics and modulation response in semiconductor quantum dot lasers. Phys Rev B 78:035316-1–11

Lüdge K, Aust R, Fiol G, Stubenrauch M, Arsenijević D, Bimberg D, Schöll E (2010) Large-signal response of semiconductor quantum-dot lasers. IEEE J Quantum Electron 46:1755–1762

Luo GP, Peng C, Le HQ, Pei SS, Hwang WY, Ishaug B, Um J, Baillargeon JN, Lin CH (2001) Grating-tuned external-cavity quantum-cascade semiconductor lasers. Appl Phys Lett 78:2834–2836

Marciante JR, Agrawal GP (1998) Spatio-temporal characteristics of filamentation in broad-area semiconductor lasers: experimental results. IEEE Photon Technol Lett 10:54–56

Martín-Regalado J, van Tartwijk GHM, Balle S (1996a) Mode control and pattern stabilization in broad-area lasers by optical feedback. Phys Rev A 54:5386–5393

Martín-Regaldo J, Balle S, Abraham NB (1996b) Modeling spatio-temporal dynamics of gain-guided multistripe and broad-area lasers. IEE Proc Optoelectron 143:17–23

Martín-Regalado J, Prati JF, Abraham NB (1997) Polarization properties of vertical-cavity surface-emitting lasers. IEEE J Quantum Electron 33:765–783

Masoller C, Abraham NB (1999a) Low-frequency fluctuations in vertical-cavity surface-emitting semiconductor lasers with optical feedback. Phys Rev A 59:3021–3031

Masoller C, Abraham NB (1999b) Polarization dynamics in vertical-cavity surface-emitting lasers with optical feedback through a quarter-wave plate. Appl Phys Lett 74:1078–1080

Masoller C, Torre MS, Mandel P (2006) Influence of the injection current sweep rate on the polarization switching of vertical-cavity surface-emitting lasers. J Appl Phys 99:026108-1–3

Meng B, Wang QJ (2012) Theoretical investigation of injection-locked high modulation bandwidth quantum cascade lasers. Opt Express 20:1450–1464

Merbach D, Hess O, Herzel H, Schöll E (1995) Injection induced bifurcations of transverse spatiotemporal patterns in semiconductor arrays. Phys Rev E 52:1571–1578

Mirasso CR, van Tartwijk GHM, Hernández-García E, Lenstra D, Lynch S, Landais P, Phelan P, O'Gorman J, Elsäßer W (1999) Self-pulsating semiconductor lasers: theory and experiment. IEEE J Quantum Electron 35:764–770

Mulet J, Balle S (2002) Spatio-temporal modeling of the optical properties of VCSELs in the presence of polarization effects. IEEE J Quantum Electron 38:291–305

Münkel M, Kaiser F, Hess O (1996) Spatio-temporal dynamics of multi-stripe semiconductor lasers with delayed optical feedback. Phys Lett A 222:67–75
Naumenko AV, Loiko NA, Sondermann M, Ackemann T (2003) Description and analysis of low-frequency fluctuations in vertical-cavity surface-emitting lasers with isotropic optical feedback by a distant reflector. Phys Rev A 68:033805-1–16
O'Brien D, Hegarty SP, Huyet G (2004) Sensitivity of quantum-dot semiconductor lasers to optical feedback. Opt Lett 29:1072–1074
Otto C, Lüdge K, Schöll E (2010) Modeling quantum dot lasers with optical feedback: sensitivity of bifurcation scenarios. Phys Stat Sol (b) 247:829–845
Petermann K (1988) Laser diode modulation and noise. Kluwer Academic, Dordrecht
Petitjean Y, Destic F, Mollier JC, Sirtori C (2011) Dynamic modeling of terahertz quantum cascade lasers. IEEE J Select Topics Quantum Electron 17:22–29
Rahman L, Winful H (1994) Nonlinear dynamics of semiconductor arrays: a mean field model. IEEE J Quantum Electron 30:1405–1406
Rana F, Ram RJ (2002) Current noise and photon noise in quantum cascade lasers. Phys Rev B 65:125313-1–26
Ryan A, Agrawal GP, Gray GR, Gage EC (1994) Optical feedback-induced chaos and its control in multimode semiconductor lasers. IEEE J Quantum Electron 30:668–679
Ryvkinn BS, Panajotov K, Avrutin EA, Veretennicoff I, Thienpont H (2004) Optical-injection-induced polarization switching in polarization-bistable vertical-cavity surface-emitting lasers. J Appl Phys 96:6002–6007
San Miguel M, Feng Q, Moloney JV (1995) Light polarization dynamics in surface-emitting semiconductor lasers. Phys Rev A 52:1729–1740
Scalari G, Walther C, Fischer M, Terazzi R, Beere H, Ritchie D, Faist J (2009) THz and sub-THz quantum cascade lasers. Laser and Photon Rev 3:45–66
Scholz D, Braun H, Schwarz UT, Brüninghoff S, Queren D, Lell A, Strauss U (2008) Measurement and simulation of filamentation in (Al, In)GaN laser diodes. Opt Express 16:6846–6859
Sciamanna M, Panajotov K (2005) Two-mode injection locking in vertical-cavity surface-emitting lasers. Opt Lett 30:2903–2905
Sciamanna M, Panajotov K (2006) Route to polarization switching induced by optical injection in vertical-cavity surface-emitting lasers. Phys Rev A 73:023811-1–17
Sciamanna M, Erneux T, Rogister F, Deparis O, Mégret P, Blondel M (2002a) Bifurcation bridges between external-cavity modes lead to polarization self-modulation in vertical-cavity surface-emitting lasers. Phys Rev A 65:041801-1–4
Sciamanna M, Rogister F, Deparis O, Mégret P, Blondel M, Erneux T (2002b) Bifurcation to polarization self-modulation in vertical-cavity surface-emitting lasers. Opt Lett 27:261–263
Sciamanna M, Masoller C, Abraham NB, Rogister F, Mégret P, Blondel M (2003a) Different regimes of low-frequency fluctuations in vertical-cavity surface-emitting lasers. J Opt Soc Am B 20:37–39
Sciamanna M, Masoller C, Rogister F, Mégret P, Abraham NB, Blondel M (2003b) Fast pulsing dynamics of a vertical-cavity surface-emitting laser operating in the low-frequency fluctuation regime. Phys Rev A68:015805-1–4
Sciamanna M, Valle A, Mégret P, Blondel M, Panajotov K (2003c) Nonlinear polarization dynamics in directly modulated vertical-cavity surface-emitting lasers. Phys Rev E 68:016207-1–4
Shoji H, Nakata Y, Mukai K, Sugiyama Y, Sugawara M, Yokoyama N, Ishikawa H (1997) Lasing characteristics of self-formed quantum-dot lasers with multistacked dot layer. IEEE J Selct Topics Quantum Electron 3:188–195
Simmendinger C, Preißer D, Hess O (1999) Stabilization of chaotic spatiotemporal filamentation in large broad area lasers by spatially structured optical feedback. Opt Express 5:48–54
Sondermann M, Bohnet H, Ackemann T (2003) Low-frequency fluctuations and polarization dynamics in vertical-cavity surface-emitting lasers with isotropic feedback. Phys Rev A 67:021802-1–4
Sugawara M (1999) Self-assembled InGaAs/GaAs quantum dots. Academic Press, San Diego

Tabaka A, Peil M, Sciamanna M, Fischer I, Elsäßer W, Thienpont H, Veretennicoff I, Panajotov K (2006) Dynamics of vertical-cavity surface-emitting lasers in the short external cavity regime: pulse packages and polarization mode competition. Phys Rev A 73:013810-1–14

Tachikawa T, Takimoto S, Shogenji R, Ohtsubo J (2010) Dynamics of broad-area semiconductor lasers with short optical feedback. IEEE J Quantum Electron 46:140–149

Takiguchi Y, Asatsuma T, Hirata S (2006) Effect of the threshold reduction on a catastrophic optical mirror damage in broad-area semiconductor lasers with optical feedback. SPIE Proc 6104:61040X

Takimoto S, Tachikawa T, Shogenji R, Ohtsubo J (2009) Control of spatio-temporal dynamics of broad-area semiconductor lasers by strong optical injection. IEEE Photon Technol Lett 21:1051–1053

Tang X, van der Ziel JP, Chang B, Johnson R, Tatum JA (1997) Observation of bistability in GaAs quantum-well vertical-cavity surface-emitting lasers. IEEE J Quantum Electron 33:927–932

Totschnig G, Winter F, Pustogov V, Faist J, Müller A (2002) Mid-infrared external-cavity quantum-cascade laser. Opt Lett 27:1788–1800

Tronciu VZ, Yamada M, Ohno T, Ito S, Kawakami T, Taneya M (2003) Self-pulsation in an InGaN laser—theory and experiment. IEEE J Quantum Electron 39:1509–1514

Valle A, Sarma J, Shore KA (1995a) Spatial holeburning effects on the dynamics of vertical-cavity surface-emitting laser diodes. IEEE J Quantum Electron 31:1423–1431

Valle A, Sarma J, Shore KA (1995b) Dynamics of transverse competition in vertical cavity surface emitting laser diodes. Opt Commun 115:297–302

Valle A, Gatare I, Panajotov K, Sciamanna M (2007) Transverse mode switching and locking in vertical-cavity surface-emitting lasers subject to orthogonal optical injection. IEEE J Quantum Electron 43:322–333

van Tartwijk GHM, San Miguel M (1996) Optical feedback on self-pulsating semiconductor lasers. IEEE J Quantum Electron 32:1191–1202

Viktorov EA, Mandel P, O'Driscoll I, Carroll O, Huyet G, Houlihan J, Tanguy Y (2006) Low-frequency fluctuations in two-state quantum dot lasers. Opt Lett 31:2302–2304

Von Lehmen AC, Florez LT, Stoffel NG (1991) Dynamics, polarization, and transverse mode characteristics of vertical cavity surface emitting lasers. IEEE J Quantum Electron 27:1402–1409

von Staden J, Gensty T, Elsäßer W, Giuliani G, Mann C (2006) Measurements of the α factor of a distributed-feedback quantum cascade laser by an optical feedback self-mixing technique. Opt Lett 31:2574–2576

Wójcik AK, Belyanin A, Yu N, Diehl L, Capasso F (2010) Nonlinear coupling of transverse modes in quantum cascade lasers. Opt Eng 49:111114-1–10

Wójcik AK, Yu N, Capasso F, Belyanin A (2011a) Nonlinear optical interactions of laser modes in quantum cascade lasers. J Modern Opt 58:727–742

Wójcik AK, Yu N, Diehl L, Capasso F, Belyanin A (2011b) Self-synchronization of laser modes and multistability in quantum cascade lasers. Phys Rev Lett 106:133902-1–4

Winful HG (1992) Instability threshold for an array of coupled semiconductor lasers. Phys Rev A 46:6093–6094

Winful HG, Rahman L (1990) Synchronized chaos and spatiotemporal chaos in arrays of coupled lasers. Phys Rev Lett 65:1575–1578

Winful HG, Chen YC, Liu JM (1986) Frequency locking, quasiperiodicity, and chaos in modulated self-pulsating semiconductor lasers. Appl Phys Lett 48:616–618

Yamada M (1993) A theoretical analysis of self-sustained pulsation phenomena in narrow-stripe semiconductor lasers. IEEE J Quantum Electron 29:1330–1336

Yamada M (1996) Theoretical analysis of noise-reduction effects in semiconductor lasers with help of self-sustained pulsation phenomena. J Appl Phys 79:61–71

Yamada M (1998a) Computer simulation of feedback induced noise in semiconductor lasers operating with self-sustained pulsation. IEICE Trans Electron E81-C:768–780

Yamada M (1998b) A theoretical analysis of quantum noise in semiconductor leasers operating with self-sustained pulsation. IEICE Trans Electron E81-C:290–298